Design of Fluidized-Bed Reactors for Catalytic Fast Pyrolysis

By

Robert J. Coolman

A dissertation submitted in partial fulfillment of

the requirements for the degree of

Doctor of Philosophy

(Chemical Engineering)

at the

UNIVERSITY OF WISCONSIN-MADISON

2016

Date of final oral examination: November 9th, 2016

The dissertation is approved by the following members of the Final Oral Committee:

George W. Huber, Professor, Chemical and Biological Engineering
Thatcher W. Root, Professor, Chemical and Biological Engineering
Christos T. Maravelias, Professor, Chemical and Biological Engineering
Ive Hermans, Associate Professor, Chemistry
William F. Banholzer, Research Professor, Chemical and Biological Engineering

ABSTRACT

The net accumulation of atmospheric carbon resulting from the increase in global demand for fuels and chemicals from fossil sources warrants the search for alternatives that fit into existing infrastructure ("drop-in" chemicals and fuels) that come from renewable sources. The research presented in this thesis progresses this search for alternatives through the study of Catalytic Fast Pyrolysis (CFP) of renewable lignocellulosic biomass.

We studied CFP of cellulose at 500°C using a ZSM-5 catalyst in a bubbling fluidized bed reactor constructed from a 4.92-cm ID pipe. Inert gas was fed from below through a distributor plate and from above through a vertical feed tube along with cellulose. Aromatic yield reached a maximum of 31.6% carbon with increasing gas residence time by changing the catalyst bed height. Increasing the hole-spacing in the distributor plate was shown to have negligible effect on average bubble diameter and hence did not change the product distribution. Aromatic yields of up to 39.5% carbon were obtained when all studied parameters were optimized.

In a larger 9.67-cm ID process development unit (PDU) with on-stream particle input and output, we studied CFP of pine sawdust over ZSM-5 catalyst. The PDU maintained constant product yield of aromatics over an extended reaction period (6 hrs) with continuous catalyst addition and removal. The yields and selectivity for aromatics and olefins were dependent on temperature, biomass weight hourly space velocity (WHSV), catalyst to biomass ratio, fluidization gas velocity, and catalyst bed weight. The overall aromatic yield increased up to 15.5% carbon when decreasing gas velocities due to the increased vapor residence time and the improved mass transfer from smaller bubble sizes. A simulated recycle stream of CFP product gases consisting of CO, CO_2 and olefins was used to test the viability of subsequent olefin aromatization in the presence of CO and CO_2. Olefins were converted into additional aromatics while CO and CO_2

remained inert during CFP. The spray-dried ZSM-5 catalyst was stable over a series of 30 reaction/regeneration cycles.

In a third 4.92-cm ID reactor, the effect of steam for the CFP of cellulose with ZSM-5 was studied. Irreversible and reversible changes due to steaming were identified. Steam caused dealumination, a loss of total acidity, an increase in the zeolite-crystal size, and agglomeration of particles. For runs both with and without steam co-feeding, these irreversible changes caused lower yields for aromatics and char/coke, and higher yields for methane and unidentified products. In addition to irreversible catalyst changes, steam co-feeding was also found to reversibly lower yields of aromatics, char/coke, and identifiable oxygenate species, increase yields of CO and methane, and not change the overall yields of CO_2 and olefins.

Also in the third reactor, we studied the effects of catalyst contact time ($WHSV^{-1}$) and coking on CFP of cellulose. Because coke interferes with catalyst activity, the effect of catalyst contact time was studied at coke loadings known not to deactivate the catalyst. CO and CH_4 are favored at low catalyst contact times (<1,000 s), oxygenated and unidentified species at medium catalyst contact times (1,000 s – 10,000 s), and aromatics and CO_2 at high catalyst contact times (>10,000 s). At increased time on stream, the catalyst lost activity due to coking. The majority aromatic-producing activity was lost after site turnovers of 95 (cellulose monomers to Brønsted sites) corresponding to a weight turnover of 2.0 (feed weight to catalyst weight). Accumulated coke deactivates the catalyst by both filling the micropores and blocking the acid sites.

ACKNOWLEDGEMENTS

I owe a great many thanks to people who have helped me along my journey. First and foremost is my lovely wife, Epiphany. I would not have been able to do this without her love and support. Whatever the future brings, it means everything to have her promise to share it with me.

I would also like to thank my father Richard, my mother Ida, my sister Julia, and my brother William. All of them have always been within a phone call's reach. I am so lucky to have them for a family.

I am forever indebted to my advisor, Professor George W. Huber, for his guidance and patience throughout my years of study. I'm thankful for the support he showed me as I experimented in careers apart from research, and even after I had stopped believing I could finish this body of work. I am also thankful for the support of Professor T.J. "Lakis" Mountziaris, who served as my co-advisor at UMass Amherst, and whose knack for storytelling inspired me to tell stories of my own.

I would like to thank past and present members of the Huber research group for sharing the lab and office with me. I deeply appreciate all your support, knowledge, drive, and senses of humor. In particular, I would like to thank each of my lab partners. I owe so much to Dr. Haiping Yang, who did much of the lab work while she was pregnant with her second child. I could not have completed this project without her tenacity and encouragement. I offer thanks to Dr. Jungho Jae for his quick thinking and enthusiasm for research. I offer thanks to Jian Shi for her attention to detail and ability to drive a project forward. I offer thanks to Dr. Pranav Karanjkar who always knew what questions to ask and was always committed to learning how to do things in new and creative ways. Lastly I offer thanks to Dr. Torren Carlson, whom from I inherited this project, and whose mentorship has stayed with me all throughout my graduate experience.

I would like to express my gratitude towards the entire faculty and staff in the Chemical Engineering Departments at UMass Amherst and UW Madison for adding value to these years of graduate research. I offer thanks to Gary Czupkiewicz and Joseph Smith at UMass, and Joe Lord and Dr. Eric Codner at UW Madison for their technical expertise and patience in honing my skills as designer and prototyper of chemical-engineering equipment. Thanks also to Kathleen Heinzen and Christi Levenson for their resourcefulness and words of encouragement.

I am thankful for all the friendships I've made through these years; first after my trans-continental move from Oregon to Massachusetts, and second after my unexpected move to Madison, Wisconsin. Thank you, Amherst friends Sara, Alex, Paul, and Paige for being there to play games and to listen. Thank you, Madison friends Rhea, Liz, Nick, Dan, Iris, and Marissa for opening your hearts to me and my wife. Thank you also to Madison Circus Space for helping me rediscover what it means to have a community. I never expected to find myself so at home in the Mid-West.

Finally, I'd like to thank all the professors who expressed interest in sitting on my committee: James Dumesic, Thatcher Root, Christos Maravelias, Ive Hermans, William Banholzer, Lakis Mountziaris, and Curt Conner.

The research projects presented in this dissertation were supported by grants from NSF-EFRI-HyBi (Grant # 0937895). A part of this research was also supported by Anellotech, Inc., a startup company based on the technology presented in part in the content of this dissertation. I gratefully acknowledge their financial support.

TABLE OF CONTENTS

LIST OF TABLES

LIST OF FIGURES

CHAPTER 1

Introduction

The reasons for using lignocellulosic biomass as a feedstock for fuels and chemicals – as an alternative to petroleum and other fossil fuels – are twofold. Firstly, as fossil fuels become depleted, we are forced to turn to increasingly harmful methods of extraction such as off-shore drilling and hydraulic fracking which, just in the last decade, have resulted in environmental catastrophes such as the Deepwater Horizon Oil Spill and contamination of groundwater. Secondly, the continued use of fossil fuels is responsible for the rise in atmospheric carbon dioxide (CO_2) from 280 ppm to 400 ppm (and counting) in less than 300 years. Because CO_2 is a greenhouse gas, this rate of increase puts us on a trajectory of a long-term global average temperature increase of 3.6°C by 2040.[7]

To put us on an emissions track consistent with the worldwide-accepted goal of 2°C by 2040 (COP21), it is necessary to use fuels that do not cause a net accumulation of atmospheric carbon. Because lignocellulosic biomass recovers carbon from the atmosphere, the use of this biomass as fuel will not result in a net accumulation of CO_2 in the atmosphere. Lignocellulosic biomass will have an availability of over 1 billion dry tons annually at ~$40-$80/dry ton[8] by mid-21st-century.[9]

In spite of the advantages of using lignocellulosic biomass as a fuel and/or chemical precursor, it is not currently used in great quantities to produce either because the current technologies for converting biomass into fuels and chemicals are unable to economically compete with petroleum-based methods.[10, 11] For this reason, it is necessary to continue researching methods of biomass conversion.

Catalytic Fast Pyrolysis (CFP) is a method of converting lignocellulosic biomass into gasoline-range fuel and/or valuable aromatic chemicals using one thermochemical step[12-27], and it uses the inexpensive zeolite catalyst ZSM-5.[19, 26-27, 32-38] During CFP, biomass is quickly heated to moderately-high temperatures (450-650°C) where it forms pyrolysis vapors.[28-30] These vapors subsequently diffuse into the pores of the zeolite where they are converted to aromatics, olefins, CO, CO_2, and water. Coke is the major undesired byproduct that both competes with aromatics production and deactivates the catalyst.[31]

The utility of CFP becomes apparent in the context of older thermochemical technologies that achieve conversion of lignocellulosic biomass to gasoline-range fuels and chemicals. Effectively, CFP can be viewed as the consolidation of steps for two separate routes:

A. Consolidating the steps of (1) fast pyrolysis of biomass to produce bio oil and (2) catalytic upgrading of bio oil to produce drop-in fuels and chemicals
B. Consolidating the steps of (1) biomass gasification to produce syngas, (2) methanol synthesis from syngas, and (3) Mobil's Methanol-to-Gasoline (MTG) process to produce drop-in fuels and chemicals

Extensive catalyst testing has shown ZSM-5 to be a low-cost, high-yield choice zeolite catalyst for CFP, meaning it uses the same catalyst as Mobil's MTG process.[32-39] While MTG was commercially implemented in fixed-bed reactors, fluidized-bed reactors (FBRs) are even more advantageous for improved heat and mass transfer and that they allow for steady-state operation through continuous addition of fresh catalyst and removal of coked catalyst.[39]. FBRs also offer solid-feeding capabilities not available to fixed beds.

CFP of solid biomass has been studied in a variety of fluidized bed reactors, including bubbling-fluidized-bed[12, 19, 38, 40-43], spouted-bed[44, 45], and circulating-fluidized-bed[5] reactors. The

absence of moving parts also makes fluidized bed reactors ideal for CFP of biomass.[46-48] We have previously reported that the production of aromatics by CFP of biomass is highest in a fluidized reactor that has a biomass weight hourly space velocity (WHSV) between 0.1 and 0.35 hr^{-1}.[39, 49, 50] These low space velocities can realistically only be achieved at an industrial scale by using reactor configurations with low void fraction (ε) such as bubbling beds ($\varepsilon \approx 0.50$) or turbulent beds ($\varepsilon \approx 0.70$). Fast-fluidized beds ($\varepsilon \approx 0.90$) and pneumatic transport beds ($\varepsilon > 0.99$) are not feasible at the desirable range of space velocities. For example, a 2000 metric ton of biomass feed per day reactor, at a WHSV of 0.3 hr^{-1} requires 278 metric tons of catalyst, which at a density of 1250 $kg \cdot m^{-3}$, requires a solid volume of 222 m^3. A 2-m diameter reactor with a void fraction typical of fast fluidization ($\varepsilon = 0.96$), would require an implausible height of 1800 m. For these reasons, this thesis explores the bubbling regime of fluidization.

The goal of this thesis is to present design recommendations for bubbling FBR reactors optimized to produce aromatics. Chapter 2 discusses the hydrodynamic effects of bubbling FBRs on CFP, particularly how various changes to reactor configuration affect aromatic yield. Chapter 3 explores the scaling of CFP to the process-development scale (larger than lab scale, but still smaller than pilot scale), particularly the operation of an FBR at steady state with continuous addition and removal of catalyst. Chapter 4 examines the effects of steam on CFP chemistry. Chapter 5 looks at effects of catalyst contact time (at constant catalyst activity) and coking on product distribution. In Chapters 2, 4, and 5, cellulose is used as a model compound for woody biomass, which typically contains around 40% cellulose. Finally, Chapter 6 summarizes and makes recommendations for future exploration of this technology.

1.1. Process outline for CFP

Throughout this thesis, CFP experiments were performed by feeding room-temperature solid biomass (either crystalline cellulose or sawdust) into a bed of ZSM-5 fluidized by inert gas at 500-650°C and atmospheric pressure. Catalyst beds were supported by a distributor, made of either stainless-steel cloth (Chapters 4 and 5), mesh (Chapter 2), or plate with holes drilled in it (Chapter 3). Feeding was accomplished through either a drop tube from the top (Chapter 2) or an auger into the side (Chapters 3, 4, and 5). The reactors consisted of sealed 316 stainless-steel tubes either 2 inches in diameter (Chapters 2, 4, and 5) or 4 inches in diameter (Chapter 3). Each reactor was spray-coated with a protective layer of abrasion-resistant ceramic to protect its surface from corrosion. The gas flow rates were controlled by mass flow controllers (Brooks Instruments).

A reactor and plenum (the empty space below the distributor) were heated to reaction temperature using four cylindrical ceramic-fiber heaters (WATLOW), each controlled separately to create a uniform temperature profile. Heating of the plenum allows for pre-heating of the distributor-carrier gas, enabling it reach to reaction temperature before reaching the catalyst. Heating-zone temperatures were controlled by thermocouples located between the reactor body and heaters. The flanges joining the main reactor body and the plenum are heated using a band heater.

Once in the reactor, the biomass turns into pyrolysis fumes and char. The fumes adsorb to the surface of the catalyst where they turn into gasoline-range compounds, CO, CO_2, coke, and water. The product species desorb from the catalyst, and leave the top of the reactor where they enter a cyclone to separate any entrained catalyst particles. These cyclonics (always <2% of the bed mass) were either sent back to the reactor (Chapter 2) or collected and disposed (Chapters 3, 4, and 5). The product vapors continue to a condenser train which begins with a bubbler full of

solvent maintained at 0°C using an ice bath. The solvent is a known amount of ethanol (Chapters 2 and 3), isopropanol (Chapters 4 and 5), or water (also used in Chapter 3) to condense organic species. The last step of the condenser train is a series of cold-finger condensers maintained at -78°C using a dry-ice/acetone bath to condense any remaining organics. The non-condensable gases were then either vented into a fume hood, plumbed through a soap-film flow meter, or sampled in tedlar gas-sampling bags (Restek) and analyzed using gas chromatography.

After the reaction was completed, the reactor was flushed with helium for another 30 min to ensure complete purging of all volatile organic products. All the liquids of the bubbler and the condensers (on phase in Chapters 2, 3, and 5, two phases in Chapter 4) were then mixed together and analyzed using gas chromatography.

After purging and removing the condenser train, the catalyst was regenerated for approximately two hours, and always at a temperature ≥50°C higher than reaction temperature for CFP. This was to ensure complete combustion of any organic species remaining on the catalyst. The combustion effluent containing CO, CO_2, and water was then passed through a copper catalyst (13% CuO on alumina, Sigma Aldrich) held at 250°C to convert CO to CO_2. This gas stream was then passed through a Dryrite trap to remove the water, followed by a pre-weighed Ascarite trap to capture CO_2 in order to determine the quantity of char and coke generated from the reaction through gravimetric analysis.[50, 51] Because this analysis does not distinguish between char (produced from homogeneous slow pyrolysis and/or homogeneous deposition of pyrolysis vapors) and coke (produced from heterogeneous catalysis)[39, 52], yields calculated using this method are indicated using the name “char+coke.”

1.2. Materials

Plant biomass is composed of three main components: cellulose, hemicellulose, and lignin. Previous experiments have shown that cellulose is the primary contributes toward aromatic production in CFP.[53, 54] Cellulose is a good model compound for raw woody biomasses because woods contain ~40% wt. of cellulose. This thesis explores the use of two feedstocks: pure cellulose, and sawdust from eastern white pine. Chapters 2, 4, and 5 use industrial-grade cellulose with an average particle size of 200 μm (Lattice® NT Microcrystalline Cellulose, FMC biopolymer, 99%). Throughout this thesis, $C_6H_{10}O_5$ was used as the empirical formula for cellulose. Chapter 3 uses pine sawdust obtained from Cowls Building Supply (Cowls Building Supply, Amherst, MA). Prior to experiments, the wood was ground with a rotary cutter mill to pass a 1-mm screen. The ground wood was air-dried to reduce its moisture content to less than 5 wt%. The elemental composition of the dry wood feed is shown in Table 1.1.

Table 1.1. Elemental composition of dry sawdust (Eastern White Pine)[1]

Wood component	**%wt**	**Formula**	**Weight Fraction**			**Atomic Fraction**		
			C	**H**	**O**	**C**	**H**	**O**
Lignin	27.2%	$C_{9.94}H_{12.82}O_{2.94}$	67%	7%	26%	39%	50%	11%
Cellulose	37.4%	$C_6H_{10}O_5$	44%	6%	49%	29%	48%	24%
Glucomannan	20.4%	$C_{24}H_{40}O_{20}$	44%	6%	49%	29%	48%	24%
Glucuronoxylan	8.5%	$C_{21}H_{32}O_{18}$	44%	6%	50%	30%	45%	25%
Other Polysaccharides	4.3%	$C_6H_{10}O_5$	44%	6%	49%	29%	48%	24%
Pinus strobus (Eastern White Pine)	**97.8%**	$\mathbf{C_{1.00}H_{1.52}O_{0.64}}$	**51%**	**6%**	**43%**	**32%**	**48%**	**20%**

The catalyst used in CFP is commercial spray-dried 40% ZSM-5 (Intercat Inc.). Zeolite crystals are typically ~1 μm in diameter, so it is necessary to bind them together to make particles suitable for fluidization. The remaining 60% refers to the binder used to spray dry the catalyst to an average particle size of 99 μm and a standard deviation of 23 μm.

Before each CFP experiment, the catalyst was calcined in air at a temperature ~100°C than the reaction temperature (at a flowrate exceeding minimum fluidization). In Chapters 2, 4, and 5, calcining was done in situ. In Chapter 3, calcining was performed overnight via a lab furnace with large crucibles.

1.3. Definitions

The weight hourly space velocity (WHSV) of a reaction is calculated by dividing the cellulose flow rate by the amount of catalyst present inside the fluidized bed reactor as represented by Equation 1.1.

$$\text{WHSV } (h^{-1}) = \frac{\text{biomass flow rate } (g \cdot h^{-1})}{\text{weight of catalyst (g)}} \tag{1.1}$$

Weight turnover is defined as the ratio of biomass fed into a catalyst bed divided by the mass of the bed (Equation 1.2). Similarly, the site turnover is defined as the ratio of cellulose monomers fed to the catalyst bed divided by the initial number of Brønsted sites present in that bed (Equation 1.3). Weight turnovers may be converted to site turnovers by multiplying by an experimentally-determined factor of 47.5.

$$\text{Weight turnover} = \frac{\text{mass of biomass fed (g)}}{\text{mass of catalyst bed (g)}} \tag{1.2}$$

$$\text{Site turnover} = \frac{\text{quantity of cellulose monomers fed (mmol)}}{\text{initial quantity of Brønsted sites (mmol)}} \tag{1.3}$$

Yield of a product species is defined by Equation 1.4. Selectivity of a species towards an aromatics or olefins are defined by Equation 1.5 and Equation 1.6, respectively.

$$\text{Yield} = \frac{\text{carbon in product (mol)}}{\text{carbon in feed (mol)}} \times 100\% \tag{1.4}$$

$$\text{Aromatic Selectivity} = \frac{\text{carbon in an aromatic product (mol)}}{\text{carbon in all aromatic products (mol)}} \times 100\% \tag{1.5}$$

$$\text{Olefin Selectivity} = \frac{\text{carbon in an olefin product (mol)}}{\text{carbon in all olefin products (mol)}} \times 100\% \quad (1.6)$$

A variety of heterogeneous and homogeneous reactions simultaneously take place in the reactor and therefore it is necessary to account for the different residence times that occur in the reactor (see Figure 1.1).

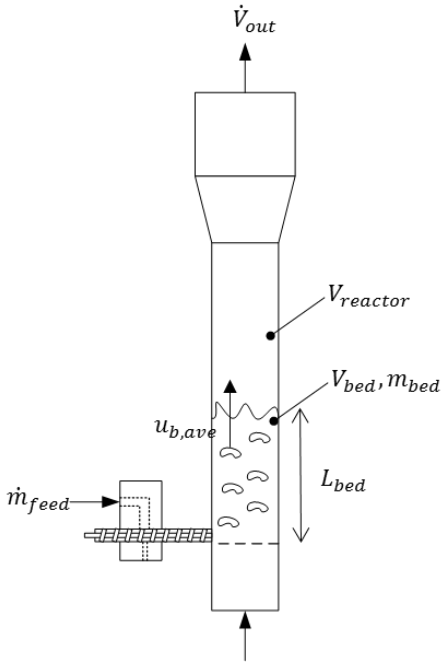

Catalyst Contact Time (1/WHSV)

$$\tau_{cat} = \frac{m_{bed}}{\dot{m}_{feed}}$$

Bubble Residence Time

$$\tau_b = \frac{L_{bed}}{u_{b,ave}}$$

Bed Residence Time

$$\tau_f = \frac{V_{bed}}{\dot{V}_{out}}$$

Reactor Residence Time

$$\tau_r = \frac{V_{reactor}}{\dot{V}_{out}}$$

Figure 1.1. Definitions of various residence times

The catalyst contact time (τ_{cat}) is defined as the weight of the catalyst bed divided by the feed rate of cellulose (Equation 1.7). The catalyst contact time is also equal to the inverse of WHSV. The duration of τ_{cat} is also the time it takes for the weight turnover to reach a value of 1 (or increase by 1). Bubble residence time (τ_b) is defined as the height of the fluidized bed divided by the average rate at which the bubbles ascend through the fluidized bed (bubble-rise velocity) (Equation 1.8). The fluidized bed residence time (τ_f) is defined as the volume of the fluidized bed divided by the output volumetric flowrate (Equation 1.9). Both of τ_b and τ_f are estimated by the Assemblage Model described later in this chapter. Because the bed does not occupy the total

volume of the reactor, it is also important to consider reactor residence time (τ_r), which is defined as the volume of the reactor (which includes both the fluidized bed and the headspace above it) divided by the output volumetric flow rate (Equation 1.10). Output volumetric flow rate was determined using a soap-film flow meter.

$$\text{Catalyst contact time, } \tau_{cat}\text{ (s)} = \frac{m_{bed}}{\dot{m}_{feed}} = \frac{\text{mass of catalyst (g)}}{\text{biomass feed rate } (\text{g}\cdot\text{s}^{-1})} = \frac{3600\ (\text{s}\cdot\text{h}^{-1})}{\text{WHSV } (\text{h}^{-1})} \quad (1.7)$$

$$\text{Bubble residence time, } \tau_b\text{(s)} = \frac{L_{bed}}{u_{b,ave}} = \frac{\text{height of fluidized bed (cm)}}{\text{average bubble-rise velocity } (\text{cm}\cdot\text{s}^{-1})} \quad (1.8)$$

$$\text{Bed residence time, } \tau_f\text{ (s)} = \frac{V_{bed}}{\dot{V}_{out}} = \frac{\text{volume of fluidized bed } (\text{cm}^3)}{\text{output volumetric flow rate } (\text{cm}^3\cdot\text{s}^{-1})} \quad (1.9)$$

$$\text{Reactor residence time, } \tau_r\text{ (s)} = \frac{V_{reactor}}{\dot{V}_{out}} = \frac{\text{volume of reactor } (\text{cm}^3)}{\text{output volumetric flow rate } (\text{cm}^3\cdot\text{s}^{-1})} \quad (1.10)$$

d_{b0}	Initial bubble diameter (cm)
d_{bm}	Maximum bubble diameter (cm)
d_b	Bubble diameter (cm)
$d_{b,ave}$	Average bubble diameter (cm)
d_p	Catalyst particle diameter (μm)
D_t	Diameter of the fluidized bed reactor (cm)
L_f	Fluidized bed height (cm)
L_m	Minimum/fixed bed height (cm)
l_{or}	Hole-spacing in a distributor plate (cm)
N_{or}	Hole-density of a distributor plate (cm^{-2})
Q_c	Total carrier gas flow rate (sccm)
Q_{ft}	Carrier gas flow rate through feed tube (sccm)
Q_{mf}	Minimum fluidization flow rate (sccm)
Q_p	Products flow rate (sccm)
Q_t	Total gas flow rate (sccm) = Q_c + Q_p
u_0	Superficial velocity of the carrier gas ($\text{cm}\cdot\text{s}^{-1}$)
u_b	Bubble velocity ($\text{cm}\cdot\text{s}^{-1}$)
$u_{b,ave}$	Average bubble velocity ($\text{cm}\cdot\text{s}^{-1}$)
u_f	Velocity of gas through the bottom inlet ($\text{cm}\cdot\text{s}^{-1}$)
u_{mf}	Minimum fluidization velocity ($\text{cm}\cdot\text{s}^{-1}$)
V_i	Volume of phase *i* (cm^3)

$\dot{V}_i$	Volumetric flow of phase *i* ($cm^3 \cdot s^{-1}$)
z	Height above the distributor plate (cm)
δ	Fraction of bed occupied by bubble phase (dimensionless)
ε	Void fraction (dimensionless)
ρ_i	Density of component *i* ($g \cdot cm^{-3}$)
τ_b	Gas residence time in bubble phase (s)
τ_e	Gas residence time in emulsion phase (s)
τ_f	Overall vapor residence time in fluidized bed (s)

1.5. The Assemblage Model

It was desired to gain an understanding of the hydrodynamics based on phenomena intrinsic to bubbling fluidized beds and the associated empirical relations found in the literature. For this purpose, we combined several of these relations to create the "Assemblage Model" to enhance the understanding offered by the traditional Kunii-Levenspiel (K-L) model for bubbling fluidization.

The most important hydrodynamic quantity is bubble size.[55] While bubbles aid in turbulence and mixing, gas within bubbles must diffuse out into the surrounding emulsion phase in order to interact with the catalyst. To some extent, gas within a bubble bypasses the emulsion. While there is appreciable gas exchange between the bubble and the emulsion, the mass transfer rate is limited by the surface area of the bubble. Because the surface-area to volume ratio decreases as the bubbles coalesce, bubble-emulsion exchange rates decrease rapidly with increasing bubble size. Decrease in mass transfer becomes an issue if bubbles become too large, and even larger bubbles can even form slugs which are rough on the catalyst and reactor.

Many models of fluidized-bed hydrodynamics, including the K-L model, revolve around two phase theory.[46] In two-phase theory an "emulsion phase" is assumed to contain all particles and to be under the conditions of minimum fluidization (superficial velocity u_{mf} and void fraction ε_{mf}). All flow in excess of minimum fluidization is assumed to enter the "bubble phase", which is

assumed to be devoid of any particles. With these assumptions, it is possible to calculate several hydrodynamic quantities using only bubble rise velocity u_b and volume of solids V_S. These quantities include the fraction of the bed in the bubble phase δ, the height of the fluidized bed L_f, the overall void fraction of the fluidized bed ε, the average gas residence time τ_f, and the residence times of the bubble- and emulsion-phases, τ_b and τ_e respectively.

The K-L model uses the bubble size d_b as an input to calculate the bubble rise velocity u_b from an empirical model developed by Davidson.[56] The K-L model then uses two-phase theory to calculate δ, L_f, ε, τ_f, τ_b, and τ_e (see Figure 1.2). Because we were interested in predicting bubble size, we developed the Assemblage Model by combining a variety of empirical relations found in the literature using MATHCAD. The bubble size $d_b(z)$ and bubble rise velocity $u_b(z)$ were calculated as functions of the vertical distance above the distributor, z, using the inputs of bed mass, particle size, input fluidization gas velocity, and distributor configuration.[46] The model's feasibility was verified through qualitative comparison with bubble sizes observed in a cold-flow study. Other model results were validated by comparing predictions of the K-L model with the bubble size predicted by the Assemblage model. Figure 1.2 and Table 1.2 compare the Assemblage Model to the K-L model.

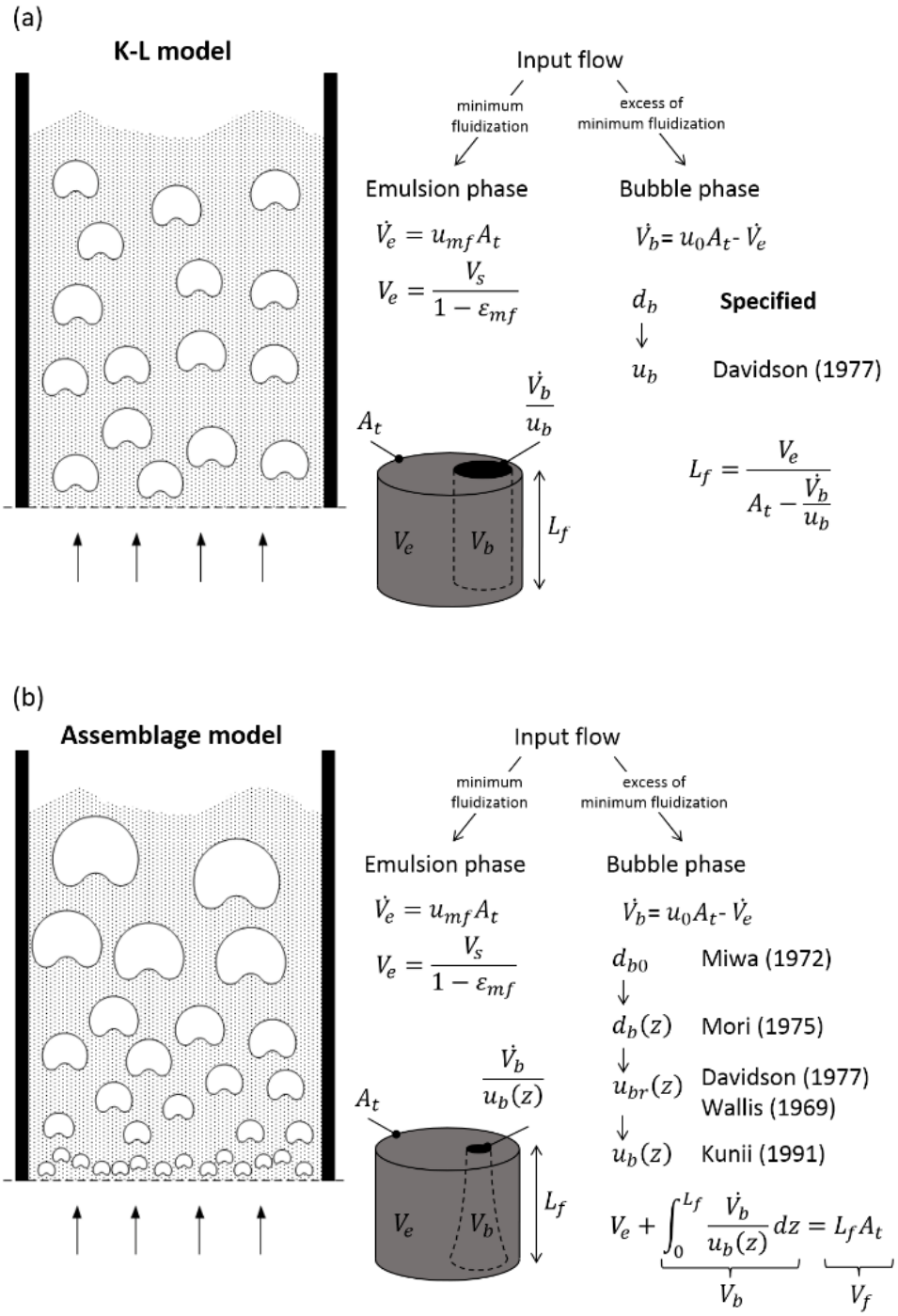

Figure 1.2. Illustrated demonstrations of correlations used to construct the (a) K-L model and (b) Assemblage Model.

Table 1.2. Comparison of Assemblage Model with K-L model

Symbol	Description	Assemblage Model	K-L model
$d_{b,ave}$	Average bubble diameter over the height of the bed (cm)	1.19 (input for K-L)	not predicted from this model
$u_{b,ave}$	Average bubble rise velocity over the height of the bed ($cm \cdot s^{-1}$)	34.21	28.88
δ	Fraction of the bed occupied by the bubble phase	0.07	0.09
L_f	Height of the fluidized bed (cm)	18.44	18.72
ε	Void fraction of the fluidized bed	0.47	0.47
τ_f	Average gas residence time in the fluidized bed (s)	2.91	2.95
τ_b	Gas residence time in the bubble phase (s)	0.54	0.65
τ_e	Gas residence time in the emulsion phase (s)	18.18	18.18

A standard theory of two-phase fluidization was assumed, meaning the emulsion phase was assumed to be at the point of minimum fluidization, and any gas flow in excess of minimum fluidization was assumed to enter the bubble phase. The minimum-fluidization velocity u_{mf} was determined from Equation 1.11 as outlined by Wen[57]:

$$u_{mf} = \frac{\mu}{d_p \rho_g}\left(\sqrt{33.7^2 + 0.0408\frac{d_p \rho_g \Delta\rho g}{\mu^2}} - 33.7\right) \tag{1.11}$$

From here, the void fraction at minimum fluidization ε_{mf} was determined using Ergun's relation shown in Equation 1.12[58]:

$$\frac{d_p \rho_g (\Delta\rho) g}{\mu^2} = \frac{1.75}{\varepsilon_{mf}^3 \phi_s} \cdot \left(\frac{u_{mf} d_p \rho_g}{\mu}\right)^2 + \frac{150(1-\varepsilon_{mf})}{\varepsilon_{mf}^3 \phi_s^2} \cdot \frac{u_{mf} d_p \rho_g}{\mu} \tag{1.12}$$

The volume of the emulsion phase was determined by dividing the volume of the solids V_s by the volume fraction of the emulsion phase shown in Equation 1.13.

$$V_e = \frac{V_s}{1-\varepsilon_{mf}} \tag{1.13}$$

Equation 1.14 shows the residence time of the emulsion phase was determined as the volume of the gas in this phase divided by its volumetric flow rate:

$$\tau_e = \frac{\varepsilon_{mf} \cdot V_e}{\left(u_0 - u_{mf}\right) \cdot A_t} \tag{1.14}$$

The initial size of bubbles forming at the distributor was determined based on the fluidizing gas velocity u_0 and the spacing of the holes in the distributor l_{or}. The analysis is described by Miwa[59] and was modified by Kunii and Levenspiel.[46] The hole-density for a staggered arrangement of holes is given by Equation 1.15.

$$N_{or} = \frac{2}{\sqrt{3}.l_{or}^2} \tag{1.15}$$

For initial bubble sizes smaller than hole-spacing l_{or}, the distributor was treated as a perforated plate and Equation 1.16 was used to predict the initial bubble size.

$$d_{b0,\,perforated} = \frac{1.3}{g^{0.2}}\left(\frac{u_0 - u_{mf}}{N_{or}}\right)^{0.4} \tag{1.16}$$

If the initial bubble size calculated from the perforated plate correlation $d_{b0,perforated}$ is larger than l_{or}, the distributor's behavior becomes indistinguishable from that of a porous plate. In such cases, Equation 1.17 is used in place of Equation 1.15. The Assemblage Model selects the larger of the values from Equation 1.15 and Equation 1.16 as the initial bubble diameter d_{b0}.

$$d_{b0,porous} = \frac{2.78}{g}\left(u_0 - u_{mf}\right)^2 \tag{1.17}$$

Bubble size increases as the bubbles coalesce. Bubble growth with respect to distance above the distributor is described by Mori[60] in Equation 1.18. The diameter and cross-sectional area of the bed are denoted as D_t and A_t respectively.

$$d_b(\mathrm{z}) = 0.65\ \mathrm{cm}\cdot\left(\frac{A_t}{\mathrm{cm}^2}\cdot\frac{u_0 - u_{mf}}{\mathrm{cm{\cdot}s^{-1}}}\right)^{0.4} - \left(0.65\ \mathrm{cm}\cdot\left(\frac{A_t}{\mathrm{cm}^2}\cdot\frac{u_0 - u_{mf}}{\mathrm{cm{\cdot}s^{-1}}}\right)^{0.4} - d_{b_0}\right)\cdot\exp\left(\frac{-0.3\cdot z}{D_t}\right) \tag{1.18}$$

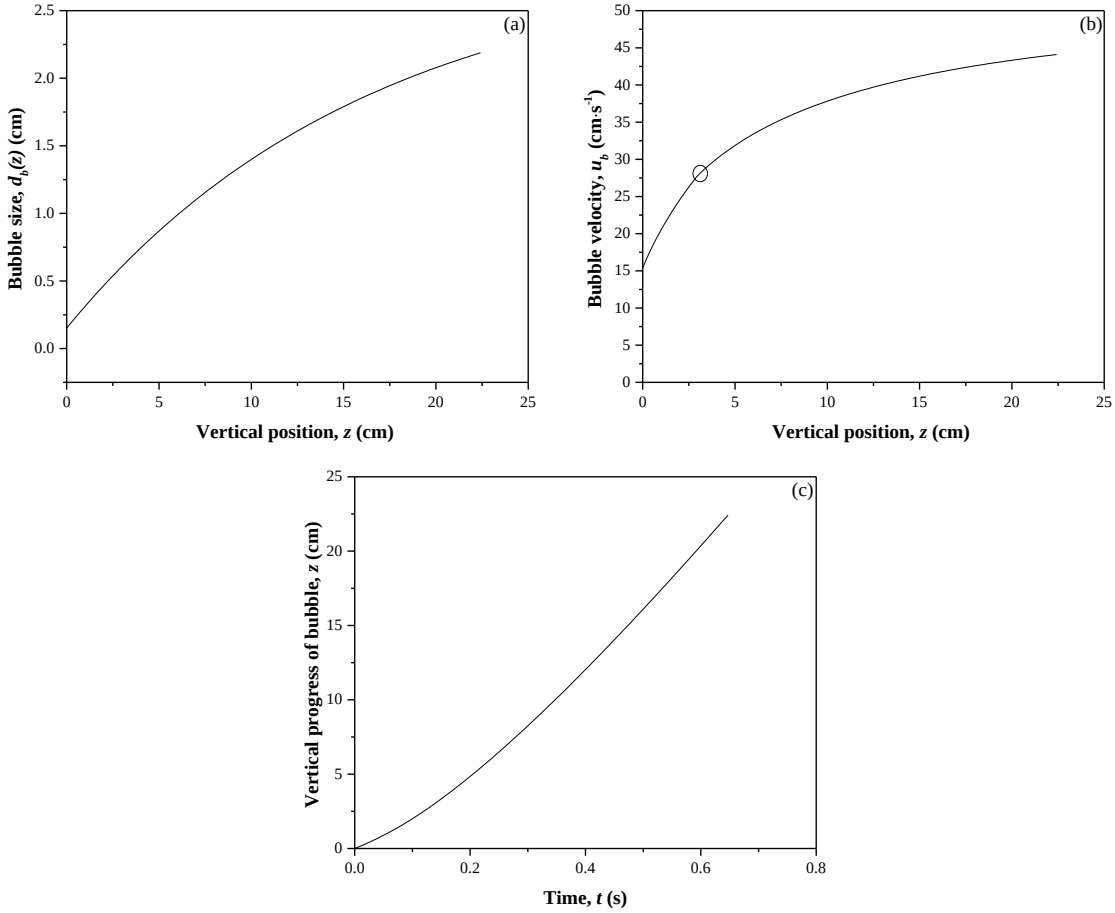

Figure 1.3. Results from the Assemblage Model. (a) Size of bubbles as a function of height above the distributor. Note the initial bubble size at $z = 0$. (b) The velocity of the bubbles as a function of height above the distributor. "○" indicates the transition from free bubbles to introduction of frictional wall effects. (c) The progress of a bubble's rise through the bed as a function of residence time.

The bubble size $d_b(z)$ was then used to determine the bubble-rise velocity with respect to the emulsion $u_{br}(z)$.[61] A graph showing the progress of bubble size $d_b(z)$ vs. a bubble's height above the distributor is shown in Figure 1.3a. For free bubbles, we used Equation 1.19.

$$u_{br,\,free}\left(z\right) = 0.711\sqrt{g \cdot d_b\left(z\right)} \tag{1.19}$$

For bubble diameters exceeding 12.5% of D_t, the frictional effects of the walls were considered. Equation 1.20 accounts for the drag on bubbles by the walls.[62]

$$u_{br,wall}(z) = 0.711\sqrt{g \cdot d_b(z)} \cdot 1.2 \cdot \exp\left(-1.49\frac{d_b(z)}{D_t}\right) \tag{1.20}$$

The Assemblage Model accounts for the emulsion's contribution to the movement of the bubbles from gulf-streaming. Kunii and Levenspiel[46] proposed Equation 1.21 from Werther's data.[63] A graph showing the progress of bubble velocity $u_b(z)$ vs. a bubble's height above the distributor is shown in Figure 1.3b.

$$u_b(z) = 1.55\ \mathrm{m{\cdot}s^{-1}}\left(\frac{u_0 - u_{mf}}{\mathrm{m{\cdot}s^{-1}}} + 14.1 \cdot \left(\frac{d_b(z)}{\mathrm{m}} + 0.005\right)\right) \cdot \left(\frac{D_t}{\mathrm{m}}\right)^{0.32} + u_{br}(z) \tag{1.21}$$

Understanding the volumetric flow of the bubble phase to be a constant $\dot{V}_b$, the bubble-rise velocity $u_b(z)$ the Assemblage Model integrates the "cross sectional area of the bubble phase" by integrating the quotient of $\dot{V}_b$ and $u_b(z)$. The height of the bed L_f was found as the numerical solution to Equation 1.22:

$$V_e + \int_0^{L_f} \frac{\dot{V}_b}{u_b(z)} dz = L_f A_t \tag{1.22}$$

The volume of the fluidized bed V_f was calculated as $L_f A_t$ and the volume of the bubble phase V_b was calculated as the difference $\left(V_f - V_e\right)$. The fraction of the bed in the bubble phase δ was calculated as V_b/V_f. The overall void fraction ε_f was calculated as $\left(V_f - V_s\right)/V_f$. The overall residence time τ_f was calculated as $\varepsilon_f L_f / u_0$.

The bubble residence time τ_b was calculated as the time it takes a bubble to travel from z = 0 to $z = L_f$, as shown in Equation 1.23.

$$\tau_b = \int_0^{L_f} \frac{1}{u_b(z)} dz \tag{1.23}$$

For time-averaged hydrodynamic parameters, we numerically solved for the inverse function *z(t)* from *t(z)*, shown by Equation 1.24.

$$t(z) = \int_0^{z} \frac{1}{u_b(h)} dh \tag{1.24}$$

Average bubble size $d_{b,\text{ave}}$ and average bubble velocity $u_{b,\text{ave}}$ were averaged over bubble residence time by Equation 1.24 and Equation 1.25.

$$d_{b,ave} = \frac{1}{\tau_b} \int_0^{\tau_b} d_b(z(t)) dt \tag{1.24}$$

$$u_{b,ave} = \frac{1}{\tau_b} \int_0^{\tau_b} u_b(z(t)) dt \tag{1.25}$$

Figure 1.3c shows the vertical progress of a bubble as a function of time.

CHAPTER 2

Effect of Fluidized-Bed Hydrodynamics on CFP Production of Aromatics

Karanjkar, P.U.; Coolman, R.J.; Huber, G.W.; Blatnik, M.T.; Almalkie, S.; de Bruyn Kops S.M.; Mountziaris, T.J.; Conner W.C., Production of aromatics by catalytic fast pyrolysis of cellulose in a bubbling fluidized bed reactor. *AlChE J.*, **2014** 60, 1320-1335.[64]

- My contribution to this work was construction and maintenance of the fluidized-bed reactor, creation of the Assemblage Model described in Chapter 1, and data analysis.
- Karanjkar, P.U. collected the data from the fluidized bed and wrote most of paper that this chapter is based upon.
- Blatnik, M.T. and Almalkie, S. built and interpreted a computational fluid dynamics model which is not included in this thesis.
- Huber, G.W.; de Bruyn Kops, S.M.; Mountziaris, T.J.; Conner W.C. were the primary investigators of this study.

2.1. Background

The objective of this chapter is to develop an understanding of how fluidized-bed hydrodynamics affect the product distribution of catalytic fast pyrolysis of cellulose in a lab-scale fluidized-bed reactor. The reactor is a 316L stainless steel 4.92-cm ID pipe with a freeboard height of 40.64 cm. Above the freeboard is a disengaging zone which includes an expansion to a 7.79-cm ID pipe. A diagram of the reactor is shown in Figure 2.1a.

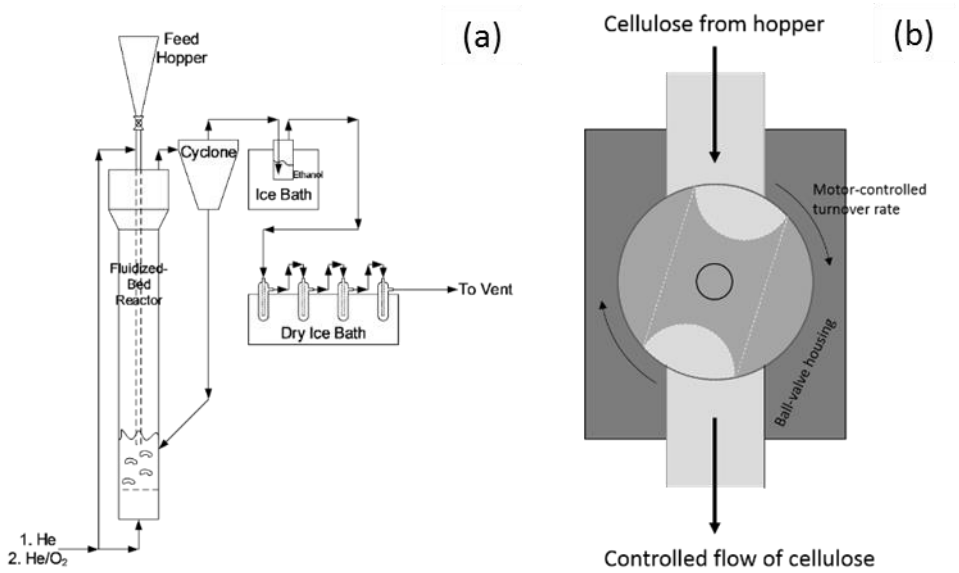

Figure 2.1. (a) Schematic of the experimental system. Ceramic heaters not shown. (b) diagram of feeder motor

Between 90 g to 250 g of catalyst were loaded into the reactor, corresponding to about 15% to 40% of the reactor volume. The catalyst bed is supported by a distributor plate made of 2 layers of stainless steel perforated plates sandwiched around a 400 mesh stainless steel cloth. Cellulose is fed into the reactor via a feed hopper connected to a 1.10-cm ID feed tube entering from the top of the reactor and extending into the fluidized bed, ending at a height 1.52 cm above the distributor plate. The free-fall time (0.35 s) of a cellulose particle is less than the feed-tube gas residence time (6.3 s) in the feed tube, meaning cellulose particles fall through the feed tube. From Whitaker's

correlation of convective heat transfer about a sphere[65], it takes an upper bound of 0.1 s to heat the bulk of a 200-μm cellulose particle to 400°C in a 500°C stream of helium flowing at average freefall velocity. Based on pyrolysis rates determined by Cho et al.[31], pyrolysis of cellulose is extremely fast at 400°C (on the order of 0.1 $g \cdot s^{-1}$). It can therefore be assumed the 6×10^{-6}-gram cellulose particles are completely pyrolyzed upon exiting the feed tube.

A feeder motor made from a partially-filled ball valve is placed below the hopper (Figure 2.1b) to control the cellulose feed rate thus controlling the WHSV to within ± 2% of the set value. During the reaction, catalyst particles were fluidized using a carrier stream of helium gas entering through the distributor (henceforth referred to as the distributor-carrier gas) and through the feed tube (henceforward referred to as the feed-tube carrier gas). This feed-tube carrier gas was necessary to ensure proper feeding of the cellulose into the fluidized bed.

The reaction temperature was 500°C. Each reaction was run for a span of 30 min. To test the reproducibility of results, we replicated experiments with varying catalyst bed height and varying distributor hole-spacing three times. We obtained standard deviation values of less than 3% for the carbon yields of different products which indicates that the data is reproducible and the trends discussed in the latter sections of this study are statistically significant.

The liquid products (dissolved in ethanol) were analyzed for aromatics using a Shimadzu GC2010 system with an Agilent HP INNOWax column (60 m, 0.32 mm, 0.5 μm) and a flame ionization detector (FID). The gaseous products collected at different times during the reaction were analyzed using a Shimadzu GC2014 system with (1) Restek Rtx®-VMS column (40 m, 0.25 mm, 1.5 μm) and an FID to analyze C3 and C4 olefins, and (2) a custom-made Supleco Hayesep D packed column with a thermal conductivity detector (TCD) to analyze CO, CO_2, methane, and ethylene. Yield of char+coke was measured using gravimetric analysis of Ascarite explained in

Chapter 1. From carbon balance, unidentified carbon was calculated by subtracting moles of carbon in product from the moles of carbon in the cellulose feed. To calculate total mass balance in some of the experiments, water content in the liquid product was analyzed using a Mettler Toledo V20 compact volumetric Karl-Fischer titrator.

2.2. Results and Discussion

2.2.1. Determination of minimum fluidization velocity

The minimum fluidization velocity was determined experimentally using pressure-drop measurements at the reaction temperature of 500°C since the molar flow rate of a carrier gas at the minimum fluidization is strongly dependent on temperature.[66, 67] By measuring the pressure drop across a span of decreasing helium flowrates, the minimum fluidization velocity was found to be 0.36 $cm \cdot s^{-1}$ (Figure 6.1) corresponding to a helium flow rate of 147 sccm (denoted throughout this chapter as Q_{mf}). This minimum fluidization velocity was found to be consistent with the predictions of Equation 1.10.[57, 68]

2.2.2. Effect of total carrier gas flow rate

CFP of cellulose was carried out at different values of the total flow rate of carrier gas (Q_c) while holding the WHSV and amount of catalyst in the bed constant. The total flow rate of carrier gas is the sum of distributor-carrier and feed-tube carrier gases. The fraction of the total amount of gas passed through the feed tube was kept constant (Q_{ft}/Q_c = 0.34). Figure 2.2 and Table 2.1 show product yields as a function of this total carrier gas flow rate while other parameters such as bed temperature, cellulose WHSV, and catalyst-bed mass were kept constant.

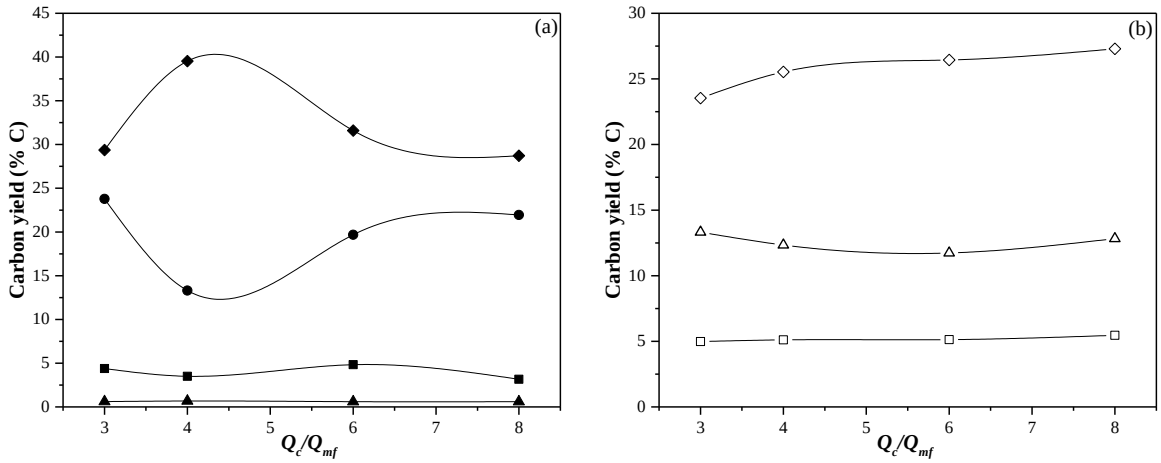

Figure 2.2. Product yields as a function of Q_c/Q_{mf} at 500°C, Q_{ft}/Q_c = 0.34 and WHSV = 0.25 ± 0.02 hr^{-1}. Key: (a) ◆:Aromatics ■:C_2-C_4 Olefins ▲:Methane ●:Unidentified (b) ◇:CO □:CO_2 Δ:Char+Coke

Table 2.1. Detailed product yields and selectivities for CFP of cellulose at various flow rates of carrier gas as a multiplier of the minimum fluidization flow rate (Reaction Conditions: Temperature of bed: 500°C, Q_{ft}/Q_c = 0.34, and WHSV: ~ 0.25 ± 0.02 hr^{-1} with 250 g catalyst)

	Q_c/Q_{mf}			
	3	4	6	8
Parameters				
d_b (cm)	0.68	0.80	1.01	1.18
u_b (cm·s^{-1})	20.64	22.85	26.24	28.97
δ	0.04	0.05	0.08	0.10
L_f (cm)	19.65	19.93	20.44	20.89
τ_b (s)	0.95	0.87	0.80	0.72
Bed expansion (%)	12	13	16	19
Q_t (sccm)	797	934	1191	1502
τ_f (s)	9.95	8.61	6.93	5.61
Overall yields (%C)				
Aromatics	29.4	39.5	31.6	28.7
C_2-C_4 Olefins	4.4	3.5	4.8	3.2
Methane	0.6	0.7	0.6	0.6
CO	23.5	25.5	26.4	27.3
CO_2	5.0	5.1	5.1	5.5
Char+Coke	13.3	12.3	11.7	12.8
Total carbon balance	**76.2**	**86.7**	**80.3**	**78.0**
Unidentified	23.8	13.3	19.7	22.0
Aromatic selectivity (%C)				
Benzene	17.0	20.4	17.8	17.6
Toluene	33.6	36.7	34.9	35.7
Ethyl-benzene	0.83	0.81	0.64	0.71
Xylenes	21.3	20.5	20.9	22.3
Styrene	0.0	0.2	0.2	0.0
Benzofuran	0.4	0.2	0.2	0.4
Indene	2.5	2.1	2.6	0.3
Phenol	2.3	1.5	1.8	2.4
Naphthalenes	22.0	17.6	20.8	20.7
Olefin selectivity (%C)				
Ethylene	36.9	51.4	42.0	67.8
Propylene	55.5	43.6	52.3	28.2
C_4 olefins	7.6	5.0	5.7	4.0

Table 2.2 also lists the bubble residence time and average gas residence times inside the catalyst bed. Gas residence times were calculated using Equation 2.4. The total gas flow rate (Q_c) includes the product gas flow rate (Q_p) as the latter was measured to be in the range of 300 sccm to 350 sccm for the cellulose WHSV of 0.24 hr^{-1} (with 250 g of catalyst). As Q_c/Q_{mf} increased, the average gas residence time decreased from 9.95 s to 5.61 s in a slightly indirect proportion. This deviation is because as the total carrier gas flow rate is increased, the catalyst bed expands and contributes slightly to an increase in gas residence time.

As shown in Figure 2.2a, the aromatic yield went through a maximum of 39.5% carbon which occurred at an intermediate value of gas and bubble residence time corresponding to four times the minimum fluidization flow rate. The unidentified hydrocarbons showed the exact opposite trend and gave a minimum carbon yield of 13.3% carbon at four times the minimum fluidization flow rate. We have shown previously that the unidentified carbon is consists of molecular weight oligomer species (including tars) that collect in the condensers or elsewhere in the system. Mass balances of up to 85 wt% were achieved by analyzing the water content of the liquid product. The remaining 15 wt% is most likely high molecular weight species. In previous experiments, we obtained mass balances of 100 wt% ± 10 wt%. Chapter 3 of this thesis shows that using water (instead of ethanol) in the condenser train, these unidentified species are found in the bubbler in the form of a floating black residue. The carbon yields of C_1-C_4 olefins did not exhibit any trend with respect to carrier gas flow rate. The maximum olefin yield was 4.8% carbon.

The aromatic yield for CFP of cellulose is about twice the aromatic yield for CFP of pine wood.[39, 49] The coke yields for CFP of pine wood are 30% to 35% carbon, which are 2 to 3 times higher than coke yields obtained in this work from CFP of cellulose.[49] The cellulose portion of the biomass thus contributes more to the aromatics than the other components of the biomass. These

results are consistent with the work of Jae et al.[53] where they observed that for maple wood, maple wood with hemicellulose extracted, and maple wood with cellulose and hemicellulose extracted, aromatic yield decreased with increasing lignin content. This work suggests that lignin and the ash content in the biomass are detrimental to the production of aromatics and different feedstocks will have a different aromatics yield depending on the cellulose/hemicellulose fraction of the biomass feedstock.

2.2.3. Effect of catalyst bed height

Figure 2.3 and Table 2.2 show the product yield as a function of the catalyst bed height for CFP of cellulose at a bed temperature of 500°C and cellulose WHSV of 0.24 hr^{-1}. Each of these experiments were replicated three times to confirm the reproducibility of the results and standard deviations were calculated which are also reported in Table 2.2. A typical standard deviation of 1% to 2% was calculated for the product yields and distribution. Table 2.2 reports calculated fluidized bed heights (L_f) for different amounts of catalysts. The cellulose flow rate was increased with increasing bed height to maintain a constant WHSV. This increase in WHSV led to an increase in the product gas flow rate. The total carrier gas inlet flow rate was held constant for all these experiments.

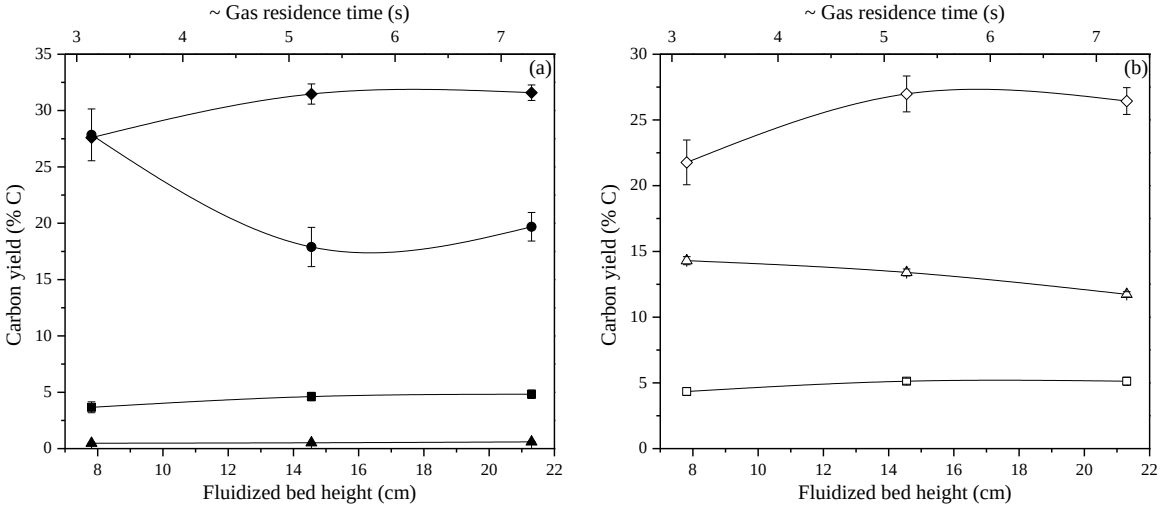

Figure 2.3. Product yields as a function of catalyst bed height / bubble residence time at 500°C, Q_c/Q_{mf} = 6, and WHSV = 0.24 ± 0.02 hr^{-1}. Key: (a) ◆:Aromatics ■:C_2-C_4 Olefins ▲:Methane ●:Unidentified (b) ◇:CO □:CO_2 Δ:Char+Coke

Table 2.2. Detailed product yields and selectivities for CFP of cellulose for different catalyst bed heights (Reaction Conditions: Temperature of bed: 500°C, WHSV: 0.24 ± 0.02 hr^{-1}, Q_c/Q_{mf} = 6)

	Bed height (cm)		
	7.81	14.55	21.30
Parameters			
Catalyst amount (g)	90	170	250
d_b (cm)	0.66	1.02	1.34
u_b ($cm \cdot s^{-1}$)	21.93	26.93	30.78
δ	0.11	0.10	0.09
τ_b (s)	0.36	0.54	0.69
Bed expansion (%)	0.23	0.22	0.21
Q_t (sccm)	1026	1100	1191
τ_f (s)	3.07	5.34	7.22
Overall yields (%C)			
Aromatics	27.6 ± 0.1	31.5 ± 0.9	31.6 ± 0.7
C_2-C_4 Olefins	3.7 ± 0.5	4.6 ± 0.4	4.8 ± 0.4
Methane	0.5 ± 0.0	0.5 ± 0.0	0.6 ± 0.0
CO	21.8 ± 1.7	27.0 ± 1.4	26.4 ± 1.0
CO_2	4.3 ± 0.3	5.1 ± 0.2	5.1 ± 0.3
Coke	14.3 ± 0.3	13.4 ± 0.3	11.7 ± 0.2
Total carbon balance	**72.2 ± 2.3**	**82.1 ± 2.3**	**80.3 ± 2.3**
Unidentified	27.9 ± 2.3	17.9 ± 1.7	19.7 ± 1.3
Aromatic selectivity (%C)			
Benzene	20.2 ± 0.8	18.4 ± 0.2	17.8 ± 0.2
Toluene	37.4 ± 1.0	35.5 ± 0.2	34.9 ± 0.4
Ethyl-benzene	0.8 ± 0.1	0.5 ± 0.0	0.6 ± 0.0
Xylenes	20.9 ± 0.0	20.9 ± 0.1	20.9 ± 0.1
Styrene	1.0 ± 0.2	0.3 ± 0.1	0.2 ± 0.1
Benzofuran	0.5 ± 0.1	0.3 ± 0.1	0.2 ± 0.0
Indene	3.2 ± 0.2	2.7 ± 0.1	2.6 ± 0.0
Phenol	2.2 ± 0.4	1.9 ± 0.1	1.8 ± 0.1
Naphthalenes	13.7 ± 1.1	19.5 ± 0.2	20.8 ± 0.6
Olefin selectivity (%C)			
Ethylene	46.5 ± 2.6	46.2 ± 3.4	42.0 ± 0.3
Propylene	49.3 ± 2.6	49.4 ± 3.1	52.3 ± 0.5
C_4 olefins	4.3 ± 0.1	4.3 ± 0.4	5.72 ± 0.4

The increase in the bed size leads to an increase in bubble residence time (τ_b) and gas residence time (τ_f). The bubble residence time and gas residence time increased from 0.36 s to 0.69 s and 3.07 s to 7.22 s respectively. Initially, as the bed height increased from 6.4 cm to 12 cm, the aromatic yield increased from 27.6% carbon to 31.5% carbon. Further increase in bed height to 17.6 cm only increased the aromatic yield by 0.1% carbon. The aromatic selectivity, however, did change with increased bed height. The benzene and toluene selectivities decreased from 20.2% and 37.4% to 17.8% and 34.9% respectively, as the bed height increased. The naphthalenes selectivity increased from 13.7% to 20.8% with increased bed height, suggesting that gas residence time is an important parameter for tuning selectivity towards mono-aromatics. The selectivity towards oxygenates such as benzofuran and phenol also showed a slight decrease with an increase in bed height. This could be because of the longer gas residence time in the catalyst bed allowing for more deoxygenation by decarbonylation and decarboxylation. This is consistent with the slight increase in CO and CO_2 yield. The yield of C_2-C_4 olefins increased from 3.7% to 4.8% with slightly higher selectivity towards C_3-C_4 olefins than ethylene. Among other non-condensable gases, CO and CO showed an overall increase in their yields. The coke yield decreased from 14.3% to 11.7% as the bed height increased. These results suggest that gas residence time plays an important role in tuning the product distribution. Higher gas residence times shift the aromatics distribution towards polyaromatic compounds.

In these experiments, since the cellulose WHSV is maintained at a constant value of 0.25 hr^{-1}, increasing the bed height also increases the rate at which cellulose is fed. This changes the concentration of pyrolysis vapors entering the catalyst bed from the feed-tube. It is not known whether this increase of local concentration of pyrolysis vapors at the outlet of the feed-tube significantly affects the product distribution independently of residence time.

2.4.4. Effect of distributor plate hole-spacing

Three distributor plates were prepared with different hole-spacings: 284 µm, 787 µm, and 2778 µm. Hole-spacing is the center-to-center distance between two holes on a distributor. As described in Section 2.4, hole-spacing of a distributor plate determines the initial diameter of the bubbles formed. The experiments were carried out at a constant temperature of 500°C, a constant WHSV of 0.24 hr^{-1}, and a fixed carrier gas flow rate of 880 sccm. Each experiment was repeated three times to test the reproducibility of the results. We expected a significant difference in the product yield as a function of the initial bubble diameter, which was varied over an order-of-magnitude. Table 2.5 shows the hydrodynamic parameters calculated using the Assemblage Model developed here. While initial bubble size was estimated to increase by an order-of-magnitude when similarly increasing the distributor hole spacing, other hydrodynamic parameters (most importantly, average bubble size) were estimated to remain almost constant. This was reflected in the product distribution.

Table 2.3 and Figure 2.4 show product yields with standard deviations as a function of hole-spacing in a perforated plate distributor plate. Standard deviations of less than 1% for the product yields are indication of reproducible results. The bubble residence time was estimated to change slightly from 0.73 s to 0.69 s with a change in the distributor plate. The gas residence time did not change in this case as the product flow rate was almost the same in all the experiments. The aromatic yield and C_2-C_4 olefins showed only a slight change as the hole-spacing was increased almost 10 times. As can be seen from Table 2.5, the yield and selectivity of different products did not change appreciably. Since the average bubble diameter didn't change appreciably, we were unable to test the effect of average bubble size on the product distribution.

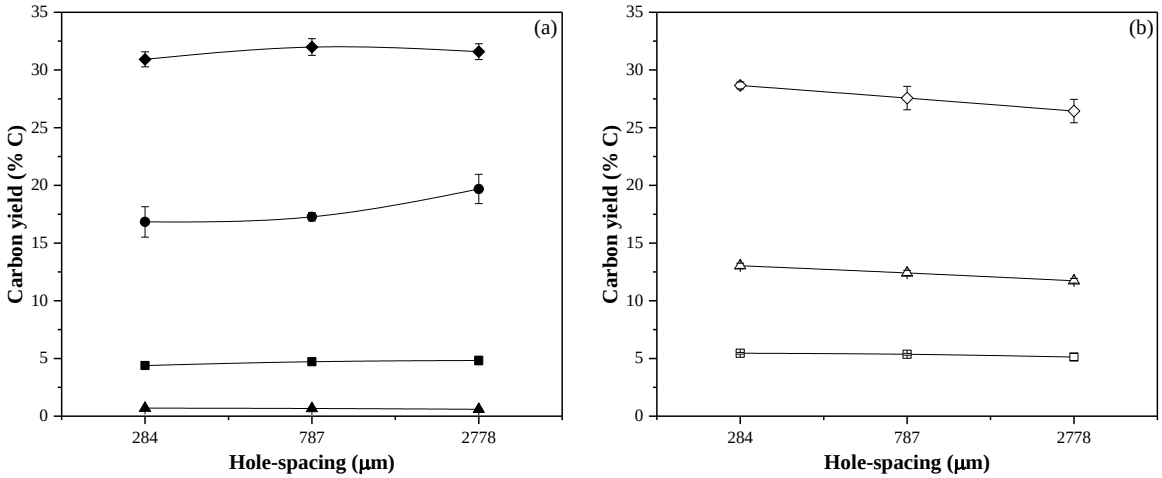

Figure 2.4. Product yields as a function of hole-spacing in the distributor plate at 500°C, Q_c/Q_{mf} = 6, and WHSV = 0.24 ± 0.01 hr^{-1}. Key: (a) ◆:Aromatics ■:C_2-C_4 Olefins ▲:Methane ●:Unidentified (b) ◇:CO □:CO_2 Δ:Char+Coke

Table 2.3. Detailed product yields and selectivities for CFP of cellulose for different hole-spacing in the distributor plates (Reaction Conditions: Temperature of bed: 500°C, WHSV: 0.24 ± 0.01 hr^{-1} with 250 g catalyst, $Q_c/Q_{mf} = 6$)

	Hole-spacing (μm)		
	284	787	2778
Parameters			
d_{b0} (cm)	0.02	0.06	0.15
d_b (cm)	1.21	1.24	1.34
u_b ($cm \cdot s^{-1}$)	29.34	29.74	30.78
δ	0.10	0.10	0.09
L_f (cm)	21.41	21.38	21.30
τ_b (s)	0.73	0.72	0.69
Bed Expansion (%)	22	22	21
Q_t (sccm)	1191	1191	1191
τ_f (s)	7.26	7.25	7.22
Overall yields (%C)			
Aromatics	30.9 ± 0.6	31.9 ± 0.7	31.6 ± 0.7
C_2-C_4 Olefins	4.4 ± 0.3	4.7 ± 0.2	4.8 ± 0.4
Methane	0.7 ± 0.0	0.7 ± 0.0	0.6 ± 0.0
CO	28.7 ± 0.3	27.6 ± 1.0	26.4 ± 1.0
CO_2	5.4 ± 0.7	5.4 ± 0.1	5.1 ± 0.3
Char+Coke	13.0 ± 0.2	12.4 ± 0.2	11.7 ± 0.2
Total carbon balance	**83.2 ± 1.3**	**82.8 ± 1.3**	**80.3 ± 1.3**
Unidentified	16.8 ± 1.3	17.3 ± 0.4	19.7 ± 1.3
Aromatic selectivity (%C)			
Benzene	17.8 ± 0.5	16.6 ± 0.4	17.8 ± 0.2
Toluene	34.0 ± 0.7	34.5 ± 0.5	34.9 ± 0.4
Ethyl-benzene	0.6 ± 0.1	0.6 ± 0.0	0.6 ± 0.0
Xylenes	20.2 ± 0.8	21.3 ± 0.4	20.9 ± 0.1
Styrene	0.3 ± 0.0	0.4 ± 0.2	0.2 ± 0.1
Benzofuran	0.2 ± 0.0	0.3 ± 0.0	0.2 ± 0.0
Indene	2.4 ± 0.2	2.5 ± 0.3	2.6 ± 0.1
Phenol	1.7 ± 0.2	1.9 ± 0.4	1.8 ± 0.1
Naphthalenes	22.6 ± 1.5	22.0 ± 1.1	20.8 ± 0.6
Olefin selectivity (%C)			
Ethylene	45.9 ± 5.8	42.1 ± 2.2	42.0 ± 0.3
Propylene	48.9 ± 6.0	52.7 ± 2.0	52.3 ± 0.5
C_4 olefins	5.2 ± 0.4	5.2 ± 0.3	5.7 ± 0.4

Because distributor hole spacing did not change the bubble size at this scale, it was hypothesized that, for average bubble size, the effect of bubble coalescence dominates over the effect of initial bubble size. To test this hypothesis, the Assemblage Model was tested at larger scales. The results are shown in Table 2.4. From these results, we see that distributor-hole spacing only affects the average bubble size in a small way, and that this effect becomes more pronounced at larger scales. This suggests that coalescence is a more important phenomenon to average bubble size than initial bubble size, and this effect of coalescence is more important at smaller scales.

Table 2.4. Results obtained from the Assemblage Model at different scales of reactor size. To maintain bed height (approximately 21 cm) the mass of bed particles was varied proportionally to the square of the column diameter D_t.

			% increase
Hole-spacing (μm)	**284**	**2778**	878%
d_{b0} (cm)	0.02	0.15	650%
Average bubble size for D_t = 5 cm	1.07	1.20	12%
Average bubble size for D_t = 50 cm	0.91	1.07	18%
Average bubble size for D_t = 500 cm	0.63	0.77	22%

2.4.5. Effect of reactor temperature

The effects of reactor temperature on pine CFP are shown in Figure 2.5. Aromatic production reaches a maximum yield of 32% at 500°C, though olefins reached a maximum yield of 7% at 550°C. All other compound groups showed an increase (methane, CO, and CO_2) or decrease (char+coke and unidentified balance carbon) across all the span of 450 to 600°C. Most striking is the rapid increase of CO production at high temperatures. This occurs coincidently with a decrease in aromatic yield, suggesting that at high temperatures, the aromatic precursors decompose into CO.

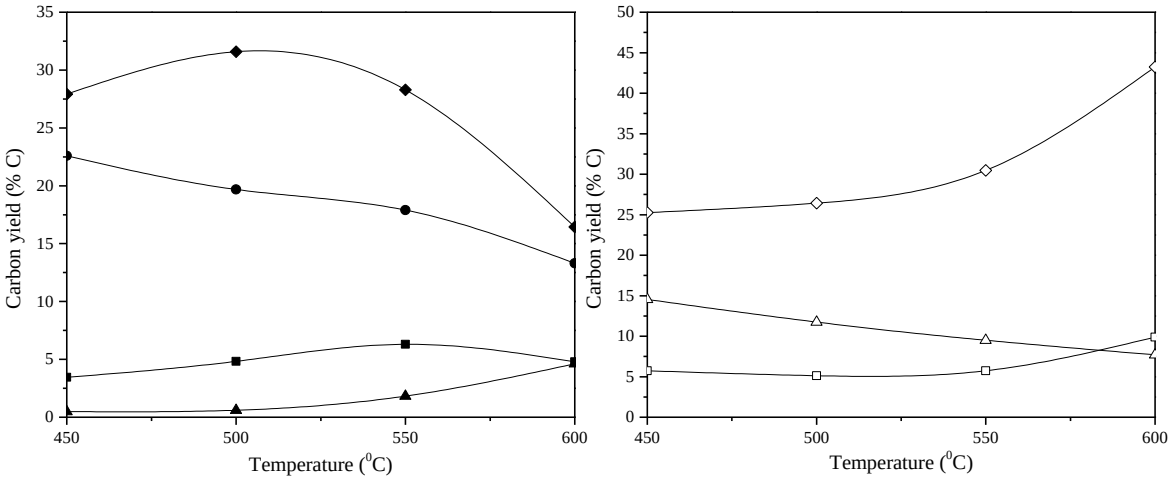

Figure 2.5. Product yields from cellulose CFP as a function of temperature with 250 g catalyst at He: 880 sccm and WHSV = 0.24 hr^{-1}. Key: (a) ◆:Aromatics ■:C_2-C_4 Olefins ▲:Methane ●:Unidentified (b) ◇:CO □:CO_2 Δ:Char+Coke

2.3. Conclusions

We carried out CFP of cellulose in a bubbling fluidized bed reactor. We obtained a maximum of 39.5% carbon yield of aromatics from cellulose as compared to reported values of 15.5% carbon yield from CFP of pine wood. This indicates that most of the aromatics formed from biomass during CFP come from the cellulose portion of the biomass. This also suggests that the lignin component of the biomass decreases the aromatics yield.

Using the Assemblage Model, we calculated hydrodynamic parameters and compared them against the experimental product yields to elucidate the effects of bubble hydrodynamics on the reaction. Average bubble sizes were predicted not to change significantly and no trends were observed between product yield and bubble size. Further use of the Assemblage Model suggested that the resolution of this model for hydrodynamic effects intrinsic to bubbles is too low to observe in our experimental reactor. However, these effects are likely to become more important at larger scales. This lack of resolution was confirmed experimentally, as no significant trends were observed when changing the hole-spacing on the distributor plate.

We used different catalyst bed heights to study how bubble residence time and gas residence time affect product yields. The aromatic yield increased from 27.6% carbon at a bed height of 6.4 cm to 31.6% carbon at a bed height of 17.6 cm. The monocyclic aromatic selectivity was higher at lower bed heights. Thus, for a bubbling fluidized bed reactor, gas residence time is an important parameter for tuning the aromatic product distribution.

CHAPTER 3

Catalytic Fast Pyrolysis of Lignocellulosic Biomass in a Process Development Unit with Continual Catalyst Addition and Removal

Jae, J.; Coolman, R.J.; Mountziaris, T.J.; Huber, G.W., Catalytic Fast Pyrolysis of Lignocellulosic Biomass in a Process Development Unit with Continual Catalyst Addition and Removal. *Chem. Eng. Sci.*, **2014**, 108, 33-46.1[39]

- My contribution to this work consisted of upgrading the PDU to allow fluidization with CO, CO_2, ethylene, and propylene, and collecting the associated data.
- Jae, J. constructed the reactor, collected the data majority of the data, and wrote the paper that this chapter is based upon.
- Mountziaris, T.J. and Huber, G.W. were the primary investigators of this study.

3.1. Background

A major obstacle in CFP operation is catalyst deactivation due to the formation of carbon residues. The carbon residues are formed from either pyrolysis of biomass (char) or by heterogeneous chemistry (coke). For CFP of biomass, it is desirable to use a regeneration furnace alongside the fluidized bed to combust char and coke deposited on (and amidst) the catalyst particles. This reactivates the catalyst before it is returned to the reactor, allowing for steady state operation.

While the coupling of reaction-regeneration reactors is well-suited concept for biomass pyrolysis, only a few papers have been reported using this configuration for catalytic pyrolysis of biomass.[5, 69-71] Lappas et al.[5] reported the use of a circulating fluid bed (CFB) reactor with continuous solid regeneration for catalytic pyrolysis of biomass. Their unit consists of a riser reactor, fluid bed regenerator, and a stripper. They presented 3-hr steady state operation data using either a ZSM-5 additive or a fluid catalytic cracking (FCC) catalyst with continuous catalyst recirculation. They employed 400-500°C for the reactor temperature and 700°C for the regenerator temperature. They obtained organic liquid product yields of up to 21 wt% over the ZSM-5 additive. However, the liquid product was a mixture of acids, aldehydes, ketones, furans, and phenols with a very low hydrocarbon yield (0.58 wt%). Zhang et. al.[70] also reported continuous catalytic pyrolysis of rice stalk in an internally interconnected fluidized bed (IIFB) reactor using a spray-dried ZSM-5 catalyst. In their reactor system, a catalytic pyrolysis bed is internally connected with a combustion bed so that the coke and char on the catalyst is combusted in the combustion bed and the regenerated catalyst is sent back to the catalytic pyrolysis bed for continuous operation. They reported total 20% carbon yield of aromatics and olefins with 3 hr time on stream.

The objective of this chapter is to demonstrate CFP technology at steady-state conditions by using a reactor that allows continual removal and addition of catalyst from a bubbling fluidized bed. The aromatic and olefin yields are a function of temperature, biomass weight hourly space velocity (WHSV), and catalyst-to-biomass feed ratio. The effects of catalyst-bed mass and fluidization-gas velocity were also investigated to understand how the hydrodynamics (e.g. bubble growth and vapor residence time) affect CFP chemistry and reactor performance. In addition to inert fluidizers, a simulated recycle stream of CFP product gases consisting of CO, CO_2 and olefins was used to test the viability of subsequent olefin aromatization in the presence of CO and CO_2. We also studied the stability of the spray-dried ZSM-5 catalyst by subjecting it to repeated reaction/regeneration cycles.

Prior to reaction, the catalyst was calcined in a muffle furnace at 580°C for 12 hr. For a typical run, 550 g of the catalyst was loaded in the reactor. Simulated recycle stream experiments were conducted with a Ga-promoted spray-dried ZSM-5 prepared by incipient-wetness impregnation. A $Ga(NO_3)_3$ solution (with an amount of 2.5 wt% Gallium with respect to the whole spray-dried ZSM-5) was slowly added via dropper to calcined ZSM-5 until it became slurry. The impregnated Ga-ZSM-5 was then dried at 110°C overnight and calcined at 600°C for 12 hr in a muffle furnace.

A schematic of the PDU is shown in Figure 3.1. The PDU consists of a fluidized bed reactor, a catalyst hopper, a catalyst inlet line, a catalyst outlet line, a biomass hopper, and a biomass inlet line. The reactor is a 4-inch outer diameter 316 stainless-steel tube with a free board height of 30 inches. The top of the freeboard expands to a 6-inch outer diameter to suppress entrainment of catalyst particles in the exit gas stream. The catalyst bed was supported by a distributor made from a 316-stainless-steel wire mesh (50 X 250 mesh). The portion of reactor

below the distributor plate served as a gas preheater. This bottom section of the reactor was loosely packed with quartz wool to encourage gas distribution and heat transfer. The catalyst was fluidized with nitrogen controlled by a mass flow controller (Brooks) in the range of 3.2 – 11 slpm. The reactor was externally heated with a four-zone electric furnace to minimize the temperature gradient across the reactor. All zones were maintained at reaction temperature. The temperatures inside the reactor were measured by K-type thermocouples inserted to a penetration depth of 1 cm.

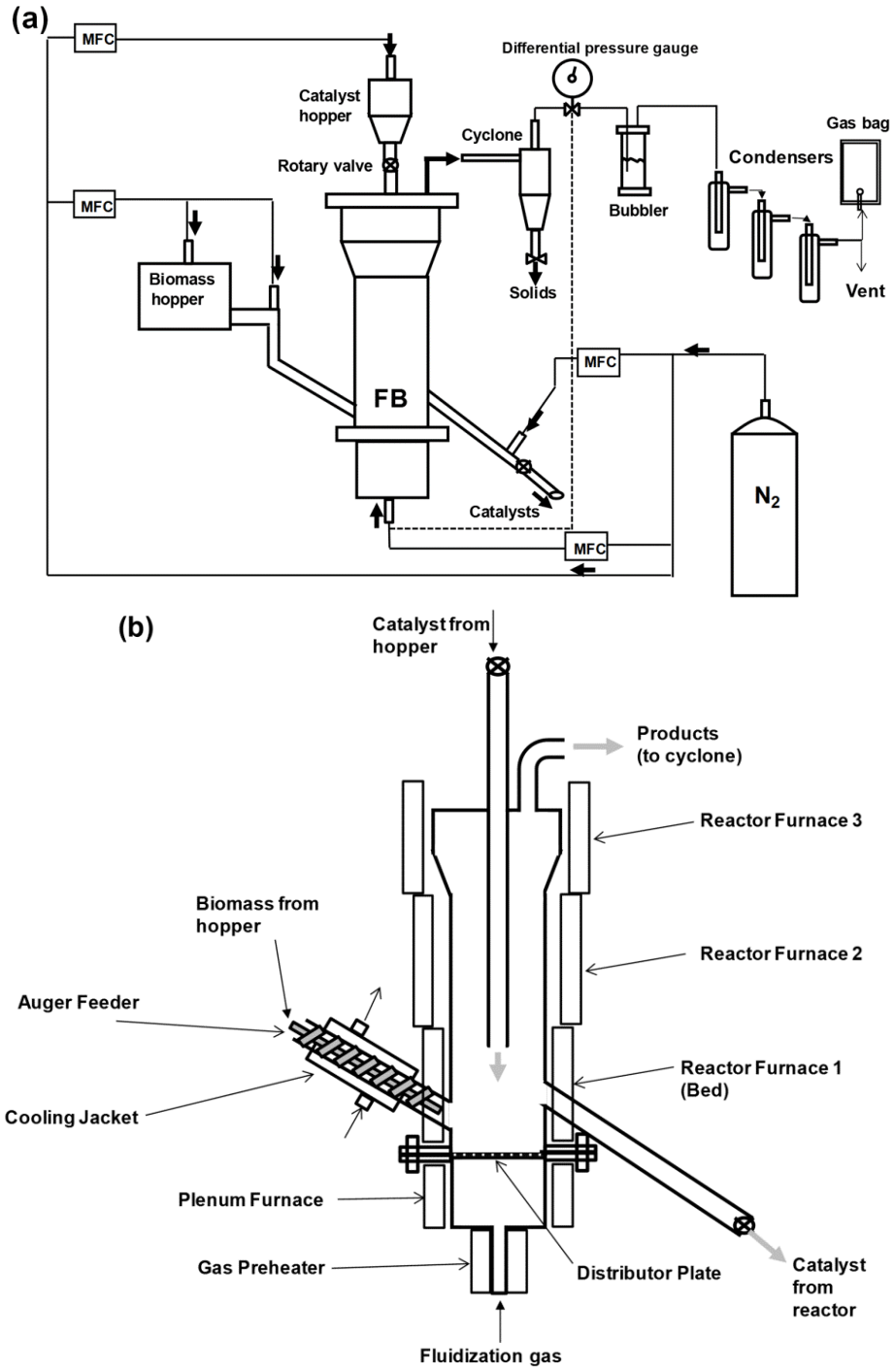

Figure 3.1. Experimental setup of the process development unit. (a) Schematic of the process development unit and (b) detailed cross-sectional drawing of the reactor.

The pinewood feedstock was loaded into a sealed feed hopper (Tecweigh, volumetric feeder) where a motor-controlled stainless-steel auger conveyed it to the biomass inlet line. The

auger motor was calibrated using a mass scale and stopwatch. The biomass inlet line (jacket cooled to a temperature of 0°C) contained a second conveyor which delivered the biomass into the reactor at a point 1 inch above the distributor. To maintain an inert environment in the feeding system, the hopper was swept with nitrogen at a rate of 2 slpm. This nitrogen sweep also served to prevent product vapors from flowing into the pinewood feeding system.

The catalyst was loaded into a separate catalyst hopper located on the top of the reactor and added continuously to the reactor through the catalyst inlet line by a specially designed ball valve (Swagelok, T60M thermal series ball valve). Two wells were drilled into the solid valve ball to serve as a device to meter catalyst. The valve turnover rate was used to adjust the mass flow rate of the catalyst. After metering, catalyst fell onto the catalyst bed through the catalyst inlet line which ended at a point 6 inches above the distributor. The catalyst hopper was swept with nitrogen at a rate of 0.8 slpm to prevent flow of product vapors into the catalyst-feeding system.

During operation, bed particles were continuously removed from the reactor through the catalyst outlet line connected to the side of the reactor at a point 1.5 inch above the distributor. The same value for catalyst input was used for catalyst removal. A small nitrogen flow at a rate of 0.040 slpm was introduced through the catalyst outlet line to strip any remaining products from the catalyst. To maintain a constant fluidized-bed weight, the particle removal rate was manually adjusted in response to changes in pressure drop across the fluidized bed, which was measured with an analog differential pressure gauge (0 to 8 inches aqueous).

The gas exiting the reactor was passed through a cyclone where any entrained solids were removed. Solids were periodically removed from the cyclone during the reaction through the 2-way valve (open/close) installed in the bottom of the cyclone. The collected solids were mostly

composed of the entrained, fine catalyst particles. The mass of the collected cyclone solids was typically less than 2% of the bed mass, and did not have a significant combustible fraction.

Product gases exited the cyclone and entered a condenser train. First the vapors entered a stainless-steel bubbler filled with a stripping solvent (water or ethanol) chilled via an ice/water bath. After the bubbler, a series of eight glass cold-finger condensers captured the remaining condensable products. The first two condensers were maintained at 0°C in an ice/water bath. The following six condensers were maintained at -55°C in a dry ice/acetone bath. For runs using ethanol as the stripping solvent, each condenser was filled with 10 to 20 ml of ethanol to trap aromatic species more efficiently. The non-condensed vapors exiting the condenser train were collected in 5-liter Tedlar gas sampling bags every 30 min. The output gas flow rate was measured using a soap-film flow meter prior to the gas sampling.

After the reaction, liquids from the bubbler and the condensers were combined, and their volume was determined via a graduated cylinder. The solution was then analyzed with gas chromatography–mass spectrometry (GC-MS) for identification of products and gas chromatography–flame ionization detector (GC-FID) for quantification of products. The gas products in the gas sampling bag were also analyzed with GC-FID for C_3–C_4 products and gas chromatography–thermal conductivity detector (GC-TCD) for C_1–C_2 products. Carbon content of the output bed particles was determined with solid Total Organic Carbon (solid TOC) analysis. The coked catalyst was collected, transferred into alumina crucibles, and regenerated in the muffle furnace at 580°C for 16 hr in air for reuse as an active catalyst.

A typical reaction lasted for 2.5 hr, though we were able to achieve more than 7 hr of steady-state operation; a maximum imposed by the capacity of the condensers.

The catalyst was characterized before and after 30 reaction/regeneration cycles by powder X-ray Diffraction (XRD, Philips X'Pert Pro Diffractometer), and scanning electron microscope (SEM, JEOL JEM-5400 Scanning electron microscope).

3.2. Results and Discussion

3.2.1. Determination of minimum fluidization velocity

In the Appendix, Figure 6.2 shows the pressure drop across the catalyst bed against fluidizer flow rate and superficial velocity at 600°C. At velocities less than minimum fluidization, the bed is packed and the pressure drop increases with velocity. Once the bed is fluidized, the pressure drop remains constant at a value of the bed weight divided by the cross-sectional area of the reactor. A bed mass of 550 g corresponds to a pressure drop of 2.5 inches aqueous (inAq). The minimum fluidization velocity at 600°C is 0.48 cm/s, corresponding to a fluidizer flow of 0.8 slpm. The calculated minimum fluidization velocity with Equation 2.5 was close to this value, giving 0.48 cm/s at 600°C. The reaction was carried out at 3.2 – 8.0 slpm of distributor flow rate, corresponding to a superficial velocity 4 – 10 times of minimum fluidization velocity.

3.2.2. Hydrodynamic conditions as a function of the fluidizer flow rate and the bed mass

Table 3.1 shows the hydrodynamic values (average bubble diameter, expanded-bed height (as opposed to packed-bed height), and bubble residence time) as determined by the Assemblage Model for the experimental conditions used in this study (e.g. fluidizer flow rate and bed mass) as inputs. The average bubble size increases with increases in fluidizer flow and bed mass. Larger bubbles move with greater velocity, so they have a lower residence time. Conversely, increases in fluidizer flow increase the volume of the bubble phase, which increases the height of the bed, though this is a relatively small effect compared to increasing the bed mass. Larger bed masses increase the distance bubbles must travel, so increases in bed mass increase the bubble residence

time. Larger beds also allow the bubbles to reach a higher degree of coalescence, so the average bubble size increases. Thus, an increase in the fluidizer flow will increase the bubble diameter and decrease the vapor residence time, while an increase in bed height will increase both the bubble diameter and the vapor residence time.

Table 3.1. Average bubble size, bubble residence time, and expanded bed height as estimated by the Assemblage Model. Model uses total flow ($\dot{n}_{total}$), bed mass (m_{bed}), and temperature (T_{bed} = 600°C) as inputs.

$\dot{n}_0$ (slpm)	fluidizer flow rate	5	5	5	3.2	5	8	11
$\dot{n}_{feed}$ (slpm)	feed tube flow rate	2	2	2	2	2	2	2
$\dot{n}_{product}$ (slpm)	product flow rate	0.91	1.40	1.90	0.91	0.91	0.91	0.91
$\dot{n}_{total}$ (slpm)	Sum of $\dot{n}_0$, $\dot{n}_{feed}$, $\dot{n}_{product}$ (model input)	7.91	8.40	8.90	6.11	7.91	10.91	13.91
m_{bed} (g)	bed mass (model input)	550	850	1150	550	550	550	550
d_b (cm)	average bubble diameter	1.11	1.60	2.06	0.95	1.11	1.39	1.67
u_b (cm/s)	bubble velocity	41.59	49.17	55.45	37.53	41.59	47.91	53.90
δ (%)	fraction of bed occupied by bubble phase	13.10	11.78	11.07	11.07	13.10	15.86	18.07
L_f (cm)	bed height (fluidized)	13.34	20.31	27.27	13.04	13.34	13.78	14.15
expansion (%)	expansion from static bed	43.84	41.69	40.57	40.57	43.84	48.55	52.56
τ_b (s)	bubble residence time	0.33	0.42	0.50	0.35	0.33	0.29	0.27
τ_f (s)	average vapor residence time	1.36	1.92	2.42	1.69	1.36	1.04	0.86

3.2.3. PDU yield experiments

3.2.3.1 Gas product concentrations as a function of time on stream

Figure 3.2 shows the time on stream concentrations of gaseous products during CFP of pinewood in the PDU. All product concentrations quickly reach the maximum within 10 min time on stream and remain constant for the following 6 hr time on stream. This illustrates that we have achieved a steady-state condition through use of on-stream addition of active catalyst and removal

of deactivated catalyst, coke and char. A slight decrease in gas concentrations after 250 min time on stream is due to the decrease in the biomass flow rate from depletion of the amount of biomass inside the biomass hopper. Because product concentrations are at steady-state, we used the data points collected after 150-min time on stream period to study the effect of the various operating parameters.

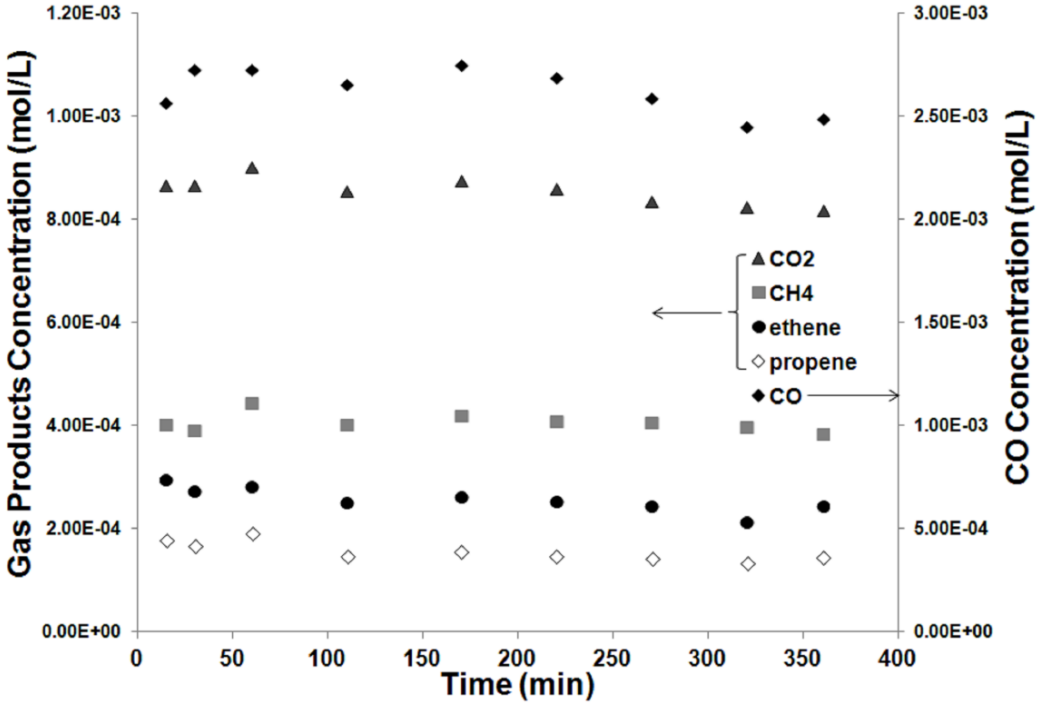

Figure 3.2. Gas phase product concentrations as a function of time on stream for catalytic fast pyrolysis of pine sawdust. Reaction conditions: spray-dried ZSM-5 catalyst, pine wood feed at 0.3 WHSV, catalyst to biomass ratio of 6, 600°C reaction temperature, 5 slpm N_2 fluidization flow rate (corresponding to a superficial fluidization velocity of 3.0 cm/s), and 550 g of catalyst.

3.3.3.2 Effect of reaction temperature

The product yields for CFP of pine wood in the PDU at different temperatures are shown in Table 3.2 and Figure 3.3. During the reaction, other operating parameters (including WHSV, catalyst to biomass ratio, fluidization gas flow rate, and bed mass) were held constant. Each run lasted for 2.5 hrs. We produced a maximum aromatic yield of 14.2% carbon at temperature of

600°C with the spray-dried ZSM-5 catalyst. It should be noted that the aromatic yield obtained at 600°C in the PDU for 150 min time on stream is close to our previously reported

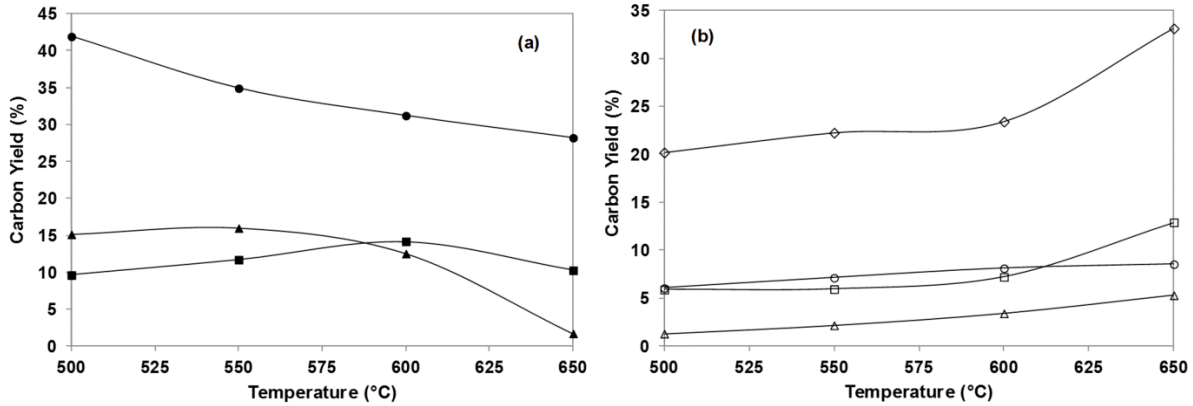

Figure 3.3. Effect of temperature on the carbon yield for CFP of pine wood in the PDU. Reaction conditions: spray-dried ZSM-5 catalyst, pine wood feed at 0.3 WHSV, catalyst to biomass ratio of 6, 5 slpm N_2 fluidization flow rate, 550 g of bed mass, and 150 min total reaction time. Key: (a) ■:Aromatics ●:Char+Coke ▲:Unidentified (b) ◊:CO □:CO_2 ○:Olefins Δ:Methane.

maximum aromatic yield of 13.9% obtained from the first 30 min time on stream in a smaller fluidized bed reactor.[12] Both product yield and selectivity are functions of temperature. The aromatic yield increases from 9.6% to 14.2% as temperature increases from 500°C to 600°C. The aromatic yield then decreases to 10.5% with further increasing temperature to 650°C. The yields of all the gaseous products, including olefins, CO, CO_2, and methane increase with temperature. The coke yield decreases with temperature as shown in Figure 3.3. These results suggest that gasification reactions are favored at higher temperatures. These trends were similar to our previous data of 30 min time on stream in the fluidized bed reactor.[12, 15] The detailed product yield and selectivity at different temperatures are listed in Table 3.2.

Table 3.2. Detailed carbon yield distribution and product selectivity for CFP of pine wood at different temperatures. Aromatic selectivity is defined as the moles of carbon in the product divided by the total moles of aromatic carbon. Olefin selectivity is defined as the moles of carbon in the product divided by the total moles of olefin carbon. Unidentified species include heavy byproducts and tars which are not detectable with GC and HPLC.

	Temperature (°C)			
	500	550	600	650
Overall Yields (%C)				
Carbon Monoxide	20.2	22.2	23.4	33.1
Carbon Dioxide	5.9	5.9	7.2	12.9
Methane	1.3	2.2	3.4	5.3
Olefins	6.0	7.1	8.1	8.5
Aromatics	9.6	11.7	14.2	10.3
Char+Coke	41.9	34.9	31.2	28.2
Total Balance	**84.9**	**84.0**	**87.5**	**98.3**
Unidentified	15.1	16.0	12.5	1.7
Aromatic Selectivity (%C)				
Benzene	17.8	20.3	27.6	41.2
Toluene	43.3	48.5	44.9	38.7
Ethyl-Benzene	1.3	0.6	0.4	0.4
m-Xylene and p-Xylene	23.9	17.7	13.0	7.7
Styrene	0.5	0.8	1.8	3.0
o-Xylene	5.1	3.7	2.8	1.4
Benzofuran	0.4	0.4	0.2	0.2
Phenol	0.7	0.4	0.6	0.7
Indene	2.2	2.3	3.5	3.4
Naphthalenes	4.8	5.1	5.4	3.4
Olefin Selectivity (%C)				
Ethylene	43.1	46.1	50.8	63.3
Propylene	47.4	47.0	43.5	32.0
Butene	5.8	3.7	2.4	1.1
Butadiene	3.8	3.2	3.3	3.7

The selectivities for both aromatic and olefin compounds are strong functions of temperature. The main aromatic products include benzene, toluene, xylenes, and naphthalenes. Benzene selectivity increases from 17.8% to 41.2%, while xylenes (total of meta, ortho and para isomers) selectivity decreases from 29% to 9.1% as temperature increases from 500 to 650°C. The olefins produced include ethylene, propylene, butene, and butadiene. Ethylene selectivity

increases, whereas propylene, butane, and butadiene selectivities decrease with increasing temperature.

3.3.3.3 Effect of Weight Hourly Space Velocity (WHSV)

The carbon yields for CFP of pine wood at 600°C as a function of weight hourly space velocity (WHSV) are shown in Figure 3.4 and Table 3.3. WHSV is defined as the mass flow rate of feed divided by the mass of catalyst in the reactor. The WHSV was adjusted from 0.15 to 0.9 hr^{-1} by changing the biomass feed rate from 82.5 – 500 g/hr while the catalyst bed mass of 550 g and the carrier flow from below of 5 slpm were held constant. The vapor residence time was also changed over these conditions due to generation of pyrolysis vapors during CFP of biomass. The overall trends on product yields at different WHSV were similar to our previous data in the fluidized bed reactor.[12, 15] The aromatic yield goes through a maximum of 14.2 % at WHSV = 0.3 hr^{-1}. Further increasing the WHSV to 0.9 hr^{-1} decreases the aromatic yield to 10.2%. The olefin yield initially decreases from 8.7% to 8.1% with increasing WHSV from 0.15 to 0.3 hr^{-1} and then increases from 8.1% to 8.9% over the rest of WHSV range. The CO and methane yields increase with WHSV from 0.15 to 0.9 hr^{-1} while the CO_2 and coke yields decrease in this same range. The amount of unidentified carbon also increases from 9.7% to 17.9% with increasing WHSV. The unidentified carbon is mostly high molecular weight oligomer species that are trapped in the cyclone, bubbler and condensers including tar. These unidentified species were visually detected in the bubbler and other liquid condensed products. However, we were not able to identify these species with GC-MS or HPLC. WHSV also influences the aromatic and olefinic selectivities. The benzene and toluene selectivities increase, while the xylenes and naphthalenes selectivities decrease as WHSV increases from 0.3 to 0.9 hr^{-1}. The ethylene selectivity decreases, whereas the

propylene, butene, and butadiene selectivities increase with increasing WHSV from 0.15 to 0.9 hr^{-1}.

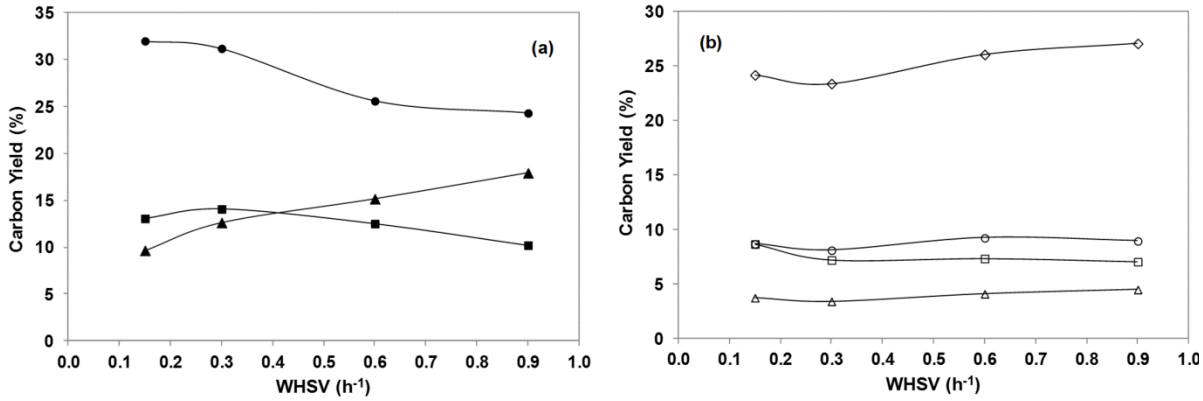

Figure 3.4. Effect of biomass WHSV on the carbon yield for CFP of pine wood. Reaction conditions: spray -dried ZSM-5 catalyst, 600°C, catalyst to biomass ratio of 6, 5 slpm N_2 fluidization flow rate, 550 g of bed mass, and 150 min total reaction time. WHSV is defined as the mass flow rate of feed divided by the initial mass of catalyst in the reactor. Key: (a) ■:Aromatics ●:Char+Coke ▲:Unidentified (b) ◊:CO □:CO_2 ○:Olefins Δ:Methane.

Table 3.3. Detailed carbon yield distribution and product selectivity for CFP of pine wood at different biomass WHSV.

	WHSV (hr^{-1})			
	0.15	0.3	0.6	0.9
Expanded bed height (cm)	13.27	13.34	13.50	13.65
Bubble diameter (cm)	1.08	1.11	1.21	1.30
Vapor residence time (s)	1.42	1.36	1.23	1.12
Overall Yields (%C)				
Carbon Monoxide	24.2	23.4	26.1	27.1
Carbon Dioxide	8.7	7.2	7.3	7.0
Methane	3.7	3.4	4.1	4.5
Olefins	8.7	8.1	9.1	8.9
Aromatics	13.1	14.1	12.5	10.2
Char+Coke	32.0	31.2	25.6	24.3
Total balance	**90.3**	**87.4**	**84.7**	**82.1**
Unidentified	9.7	12.6	15.3	17.9
Aromatic Selectivity (%C)				
Benzene	37.5	27.6	29.8	32.2
Toluene	42.7	44.9	46.4	46.9
Ethyl-Benzene	0.3	0.4	0.7	0.7
m-Xylene and p-Xylene	9.2	13.0	11.3	10.5
Styrene	0.9	1.8	1.7	1.6
o-Xylene	2.0	2.8	2.3	2.6
Benzofuran	0.1	0.2	0.3	0.4
Phenol	0.2	0.6	0.6	0.3
Indene	3.9	3.5	2.5	2.2
Naphthalenes	3.2	5.4	4.3	2.6
Olefin Selectivity (%C)				
Ethylene	53.3	50.8	44.2	42.8
Propylene	43.9	43.5	46.3	46.1
Butene	1.5	2.4	2.8	4.7
Butadiene	1.3	3.3	6.7	6.4

3.3.3.4 Effect of catalyst-to-biomass feed ratio

We also studied the effect of changing the catalyst to biomass ratio on the product selectivity. The catalyst to biomass ratio is defined as the mass flow rate of catalyst in divided by the mass flow rate of wood feed in. In these experiments the catalyst bed mass was held constant. Figure 3.5 and Table 3.4 show the product yields and selectivity as a function of catalyst to biomass ratio for CFP of pine wood at 600°C and 0.3 hr^{-1} WHSV. A catalyst to biomass ratio was

maintained in the range of 3-9 by changing the catalyst mass flow rates from 540 to 1530 g/hr. The catalyst to biomass ratio is directly related to the catalyst residence time which can be approximated as the mass flow rate of catalyst divided by the catalyst bed mass. For a 550 g bed, the catalyst residence time decreased from 60 to 20 min as the catalyst to biomass ratio increased from 3 to 9. As shown in Figure 3.5, the aromatic yield goes through a maximum of 14.2 % at a catalyst to biomass ratio of 6 and catalyst residence time of 30 min. The coke yield decreases from 33% to 28.9% while the unidentified carbon yield increases from 8.9% to 15.5% as the catalyst to biomass ratio decreases from 9 to 3. This loss of activity at low catalyst to biomass ratios is most likely due to an increase in coke on the catalyst surface. These results thus indicate that if CFP is operated below a certain catalyst to biomass ratio and above a certain catalyst residence time, coke will accumulate on the catalyst surface causing a loss of aromatic yield. For instance, the amount of coke on the catalyst increases from 2.0 to 4.1 wt% as the catalyst to biomass ratio decreases from 9 to 3. However, the gaseous product yields and the aromatic and olefin selectivities do not change with the catalyst to biomass ratio tested in this study as shown in Table 3.4.

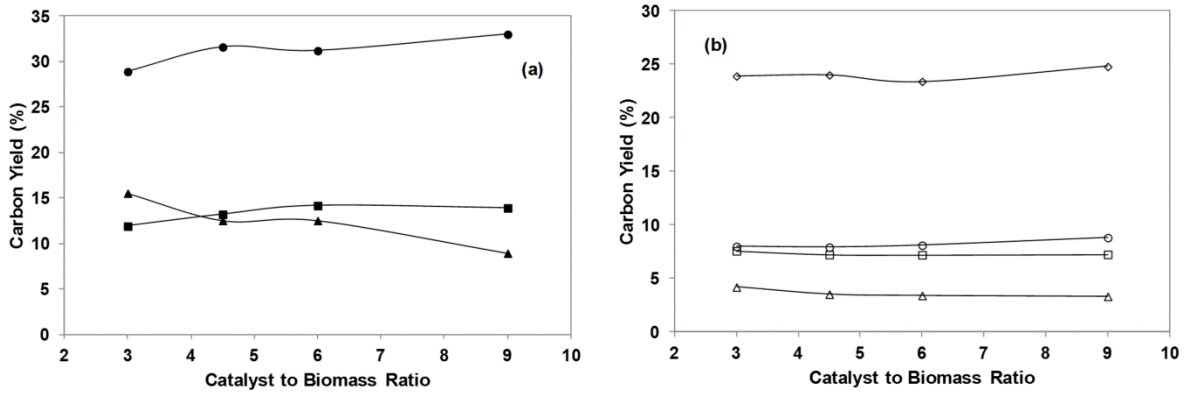

Figure 3.5. Effect of catalyst to biomass ratio on the carbon yield for CFP of pine sawdust. Reaction conditions: spray-dried ZSM-5 catalyst, 0.3 wood WHSV, 600°C reaction temperature, 5 slpm N_2 fluidization flow rate, 550 g of bed mass, and 150 min total reaction time. Catalyst to biomass ratio is defined as the mass flow rate of catalyst divided by the mass flow rate of feed. Key: (a) ■:Aromatics ●:Char+Coke ▲:Unidentified (b) ◊:CO □:CO_2 ○:Olefins Δ:Methane.

Table 3.4. Detailed carbon yield distribution and product selectivity for CFP of pine wood at different catalyst to biomass ratios.

	Catalyst to biomass ratio			
	3.0	4.5	6.0	9.0
Overall Yields (%C)				
Carbon Monoxide	23.9	24.0	23.4	24.8
Carbon Dioxide	7.6	7.2	7.2	7.2
Methane	4.2	3.5	3.4	3.3
Olefins	8.0	7.9	8.1	8.8
Aromatics	11.9	13.2	14.2	13.9
Coke	28.9	31.6	31.2	33.0
Total balance	**84.5**	**87.5**	**87.5**	**91.1**
Unidentified	15.5	12.5	12.5	8.9
Aromatic Selectivity (%C)				
Benzene	28.5	29.8	27.6	28.8
Toluene	47.3	46.2	44.9	48.9
Ethyl-Benzene	0.6	0.6	0.4	0.5
m-Xylene and p-Xylene	12.1	12.3	13.0	12.0
Styrene	1.9	1.8	1.8	1.5
o-Xylene	2.4	2.5	2.8	2.5
Benzofuran	0.3	0.2	0.2	0.2
Phenol	0.5	0.5	0.6	0.4
Inden	2.6	2.5	3.5	2.0
Naphthalenes	3.8	3.6	5.4	3.3
Olefin Selectivity (%C)				
Ethylene	49.6	50.6	50.8	48.5
Propylene	41.8	41.7	43.5	43.2
Butene	3.2	2.8	2.4	3.3
Butadiene	5.4	4.8	3.3	4.9

3.3.3.5 Effect of fluidization-gas flow rate

The effect of fluidization gas flow rate on the product yield and selectivity for CFP of pine wood is shown in Figure 3.6 and Table 3.5. The average bubble diameter and vapor residence time as a function of fluidization gas velocity is also shown in Table 3.5. Typical bubbling fluidized bed reactors operate with a fluidization gas velocity 3 to 20 fold higher than minimum fluidization velocity[72] which is within the same range we operated in these experiments. The expanded bed height slightly increases from 13.04 cm to 14.15 cm with increasing fluidization gas velocity. The size of bubbles increases from 0.95 to 1.67 cm, while the vapor residence time decreases from 1.69

to 0.86 sec with increasing fluidization gas flow rates from 3.2 to 11 slpm. The product yield shows a strong dependence on the change in the fluidization gas velocity. Both the aromatic and coke yields decrease from 15.5% to 11.2% and from 32.5% to 29.8%, respectively as the fluidization gas flow rates increase from 3.2 to 11 slpm. This suggests that the lower fluidization gas velocity has a positive effect on CFP chemistry, increasing the aromatic yield. Importantly, the olefin yield increases from 7.8% to 8.6% with increasing fluidization gas flow rates. This is indicative that the olefins are converted to aromatics more efficiently with lower fluidization gas flow rate. Thus, these results suggest that the longer vapor residence time and the smaller bubble size could improve the aromatic yield during CFP of biomass. The selectivities for aromatic and olefin compounds also show a trend with fluidization gas velocity. Benzene and toluene carbon selectivities both increase, while xylenes and naphthalenes decrease with increasing the gas flow rate, suggesting that the faster gas velocity limits the formation of xylenes and naphthalenes by the secondary reaction [73]. For olefins, ethylene selectivity decreases, whereas butene and butadiene selectivity increase with an increase in gas flow rate. An increase in C_4 olefins with the higher gas velocity indicates that these olefins leave the reactor before converting into aromatics.

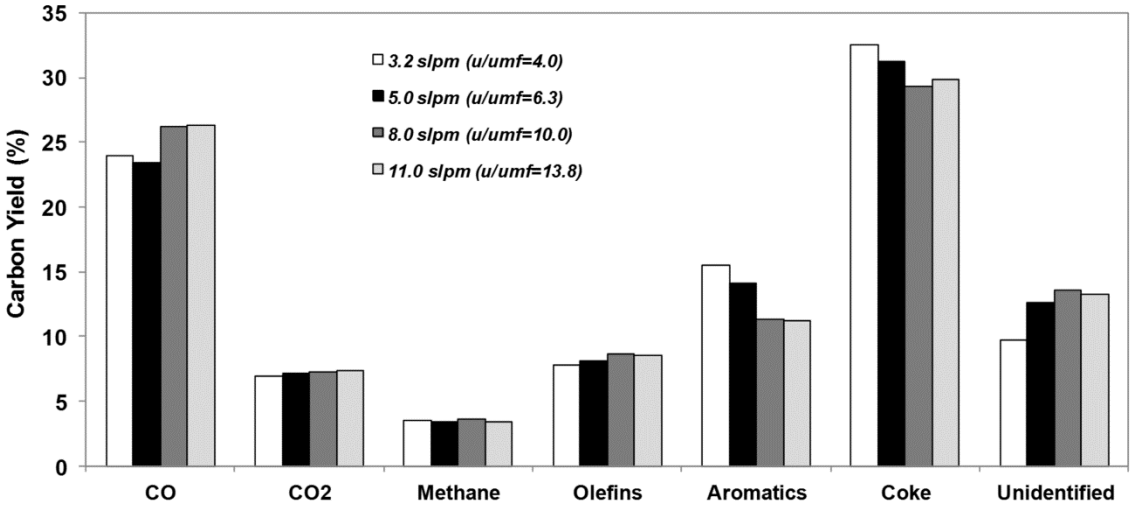

Figure 3.6**.** Effect of fluidization gas flow rates on the carbon yield for CFP of pine sawdust. Reaction conditions: ZSM-5 catalyst, 0.3 wood WHSV, catalyst to biomass ratio of 6, 600°C reaction temperature, 550 g of bed mass, and 150 min total reaction time. u/u_{mf} is the ratio of fluidization gas velocity to minimum fluidization gas velocity. Key: 3.2 slpm (white), 5.0 slpm (black), 8.0 slpm (dark grey), and 11.0 slpm (light grey).

Table 3.5. Detailed carbon yield distribution and product selectivity for CFP of pine wood at different fluidization gas flow rates.

	N_2 flow rate (slpm)			
	3.2	5.0	8.0	11.0
Expanded bed height (cm)	13.04	13.34	13.78	14.15
Bubble diameter (cm)	0.95	1.11	1.39	1.67
Vapor residence time (s)	1.69	1.36	1.04	0.86
Overall Yields (%C)				
Carbon Monoxide	24.0	23.4	26.2	26.3
Carbon Dioxide	7.0	7.2	7.3	7.3
Methane	3.5	3.4	3.6	3.5
Olefins	7.8	8.1	8.6	8.6
Aromatics	15.5	14.2	11.4	11.2
Coke	32.5	31.2	29.3	29.8
Total balance	**90.3**	**87.4**	**86.5**	**86.7**
Unidentified	9.7	12.6	13.5	13.3
Aromatic Selectivity (%C)				
Benzene	27.5	27.6	34.7	33.8
Toluene	44.1	44.9	46.6	46.2
Ethyl-Benzene	0.4	0.4	0.5	0.4
m-Xylene and p-Xylene	14.7	13.0	9.8	10.7
Styrene	1.7	1.8	1.6	1.6
o-Xylene	2.8	2.8	1.9	1.8
Benzofuran	0.2	0.2	0.2	0.1
Phenol	0.3	0.6	0.4	0.4
Indene	2.8	3.5	2.1	2.1
Naphthalenes	5.6	5.4	2.3	2.8
Olefin Selectivity (%C)				
Ethylene	53.5	50.8	50.0	50.2
Propylene	40.6	43.5	41.6	41.3
Butene	2.8	2.4	3.2	3.1
Butadiene	3.1	3.3	5.3	5.4

3.3.3.6 Effect of catalyst-bed mass

The effect of catalyst bed height on CFP of pine wood was investigated as shown in Figure 3.7 and Table 3.6. In these experiments the WHSV was held constant at 0.3 hr^{-1}. The change of the hydrodynamic conditions in the reactor is also outlined in Table 3.6.

Table 3.6. Detailed carbon yield distribution and product selectivity for CFP of pine wood at different static bed masses.

	Bed mass (g)		
	550	850	1150
Expanded bed height (cm)	13.34	20.31	27.27
Bubble diameter (cm)	1.11	1.6	2.06
Vapor residence time (s)	1.36	1.92	2.42
Overall Yields (%C)			
Carbon Monoxide	23.4	24.3	25.2
Carbon Dioxide	7.2	7.2	7.9
Methane	3.4	3.4	4
Olefins	8.1	7.8	8.1
Aromatics	14.2	13.3	13
Coke	31.2	33	34.9
Total balance	**87.5**	**88.9**	**93.2**
Unidentified	12.5	10.9	6.8
Aromatic Selectivity (%C)			
Benzene	27.6	29	30.8
Toluene	44.9	46.5	47.6
Ethyl-Benzene	0.4	0.5	0.4
m-Xylene and p-Xylene	13	12.1	10.6
Styrene	1.8	1.5	1.2
o-Xylene	2.8	2.9	2.5
Benzofuran	0.2	0.2	0.3
Phenol	0.6	0.4	0.3
Indene	3.5	2.6	2.1
Naphthalenes	5.4	4.4	4.2
Olefin Selectivity (%C)			
Ethylene	50.8	51.7	49.7
Propylene	43.5	42	43.5
Butene	2.4	2.9	3.3
Butadiene	3.3	3.4	3.4

When the bed mass was increased from 550 to 1150 g, the Assemblage Model predicted the expanded bed height to increase from 13.34 to 27.27 cm. The higher bed height leads to the formation of larger bubbles from 1.11 to 2.06 cm and an increase of vapor residence time from 1.36 to 2.42 sec. As shown in Figure 3.7, increasing the bed mass from 550 to 1150 g caused the

yield of aromatics to slightly decrease from 14.2% to 13.0%. Importantly, the coke yield increases from 31.2% to 34.9%, while the unidentified carbon yield decreases from 12.5% to 6.8% as the catalyst bed mass increases. The yields of the gaseous products, including CO, CO_2, and CH_4 increase with increasing the catalyst bed mass. In the higher bed masses, a larger bubble causes poorer interchange between the bubbles and the surrounding emulsion.[74] Because the desired reactions take place predominantly in the emulsion, larger bubbles can have a negative effect on these reactions. Conversely, longer bubble residence times create more opportunity for bubble-emulsion transfer[41], but this effect is understood to be canceled out by the increase in reactant concentration since the experiments were all done at the same WHSV. The aromatic selectivity also shows the trends with catalyst bed height. Both benzene and toluene carbon selectivity slightly increase while xylenes and naphthalenes decrease with increasing the bed height, as shown in Table 3.5. This result also suggests that the higher bed masses lead to poorer gas-catalyst interaction due to the formation of large bubbles. It is proposed that naphthalenes are formed by the secondary reaction of monocyclic aromatics with oxygenates.[73] Thus, the decrease of the naphthalene selectivity with increasing bed height could be linked to the slower mass transfer between the catalyst and the large bubble.

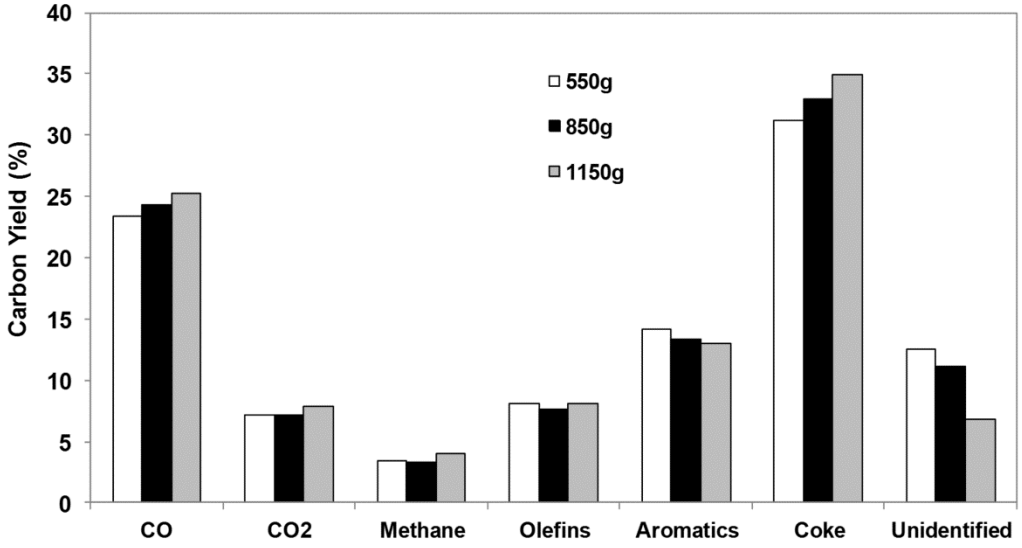

Figure 3.7. Effect of catalyst bed mass on the carbon yield for CFP of pine sawdust. Reaction conditions: spray-dried ZSM-5 catalyst, 0.3 wood WHSV, catalyst to biomass ratio of 6, 600°C reaction temperature, 5 slpm N_2 fluidization flow rate, and 150 min total reaction time. Key: 550 g of bed mass (white), 850 g of bed mass (black), and 1150 g of bed mass (grey).

3.2.4 Recycling of product gases and mass balance

In an industrial reactor, the non-condensable gases produced during CFP of wood would be recycled to the reactor as fluidization gas.[12] This configuration also allows for additional aromatization of olefins. For these reasons, it was desired to test CFP with a simulated recycle gas stream of CO, CO_2, ethylene, and propylene. Although co-fed olefins have been shown to aid in the production of aromatics from CFP[12], it was not known whether this effect would hold true in the presence of CO and CO_2. Gallium-promoted ZSM-5 was used because this modification has been shown to increase the aromatic yield of CFP.[75] It should be pointed out that the Ga-ZSM-5 catalyst (Intercat. Inc. ZSM-5) prepared for this study did not have as high an aromatic yield as our previous Ga-ZSM-5 catalyst (Intercat. Inc. ZSM-5) because of differences in catalyst preparation. These differences were primarily due to the challenges with scaling up large amounts

of catalyst. (In our previous method of preparation, we prepared 90 g of catalyst but in this chapter, we prepared 550 g of catalyst.)

To simulate the conditions for recycling the product gases, a mixed gas stream with a molar composition of 44.4% CO, 14.1% CO_2, 2.1% ethylene, 1.0% propylene, and 38.5% N_2 was used as a fluidization gas. Table 3.7 shows the fluidization gas composition and its conversion during CFP of wood. Table 3.8 shows the carbon yield and selectivity for the different products from CPF of wood using N_2 and product gas as a fluidizer, respectively. Due to the difficulties in preparing large quantities of Ga-impregnated catalyst, the catalyst input and output features were disabled. The data was collected after 30 min time on stream, a duration that we have previously shown to be long enough to obtain steady-state data, but short enough to avoid the onset of catalyst deactivation due to coking. The aromatic yield of 22% obtained from CFP of wood with simulated recycle gas is higher than the 18% from CFP of wood with N_2. Thus, the higher aromatic yield with the product gas is due to the conversion of olefins into additional aromatics. These results also suggest that CO and CO_2 gases do not have any negative impact on CFP chemistry. CFP with the simulated recycle gas also shows the higher selectivity for xylenes and the lower selectivity for benzene and naphthalenes.

Table 3.7. Fluidization gas composition and conversion for the CFP of pine wood using N_2 gas and simulated product gas as a fluidizer gas, respectively. Reaction conditions: Ga promoted ZSM-5 catalyst, 0.3 wood WHSV, 500°C reaction temperature, 550 g of bed mass, and 30 min total reaction time.

	Fluidization gas	
	N_2 fluidizer	Simulated Recycle fluidizer
N_2 (sccm)	3200 for fluidization 2000 for feed purge	0 for fluidization 2000 (38.5%) for feed purge
CO (sccm)	-	2306 (44.4%)
CO_2 (sccm)	-	731 (14.1%)
Ethylene (sccm)	-	107 (2.1%)
Propylene (sccm)	-	54 (1.0%)
	Feed composition (Moles of carbon)	
Biomass	3.72	3.72
CO	0	3.4
CO_2	0	1.08
Ethylene	0	0.32
Propylene	0	0.24
	Fluidization gas conversion	
Moles CO out / in	NA	1.2
Moles CO_2 out / in	NA	1.44
Moles Ethylene out / in	NA	0.72
Moles Propylene out/ in	NA	0.71

Table 3.8. Detailed carbon yield distribution and product selectivity for CFP of pine wood using N_2 gas and simulated product gas as a fluidizer gas, respectively. Yield is defined as net moles of carbon (out minus in) in the product divided by moles of carbon in the biomass.

	Fluidization gas	
	N_2 fluidizer	Simulated Recycle fluidizer
Overall Yields (%C)		
Carbon Monoxide	20.1	15
Carbon Dioxide	5.7	10.3
Methane	2.6	2.5
Olefins	4.7	-3.6
Aromatics	17.7	21.8
Coke	29.1	32.5
Total balance	**79.9**	**78.5**
Unidentified	20.1	22.5
Aromatic Selectivity (%C)		
Benzene	24.4	20.7
Toluene	37	38
Ethyl-Benzene	0.7	1.5
m-Xylene and p-Xylene	13.7	20.6
Styrene	1.1	1.2
o-Xylene	3.7	4.7
Benzofuran	0.6	1.6
Phenol	1.4	1
Indene	2.7	1.2
Naphthalenes	14.6	9.5
Olefin Selectivity (%C)		
Ethylene	70.5	53.6
Propylene	26.4	42.8
Butene	1.6	2.2
Butadiene	1.5	1.5

3.2.5 Coke deposition on the catalyst

After reaction, the collected coked catalyst has two distinguishable morphologies of particles: “upper char+coke” (>250 microns) which are primarily particles of biomass char with small amounts of catalyst agglomerated onto it, and “lower char+coke” (<250 microns) which consists primarily of catalyst particles containing coke formed from biomass vapors (Figure 3.8).

Approximately 20 and 80 wt% of the coked catalyst collected from each run were “upper” char+coke and “lower” char+coke, respectively. Separation of these two morphologies was achieved with a 250 μm sieve (60 mesh). The upper and lower char+coke were combusted at a ramping rate of 5°C/min to 600°C in the TGA. The temperature programmed oxidation curves of the coked catalysts are shown in Figure 3.9. Thermogravimetric curves (TG, in wt.%) shows that the upper char+coke contained more carbon (~10.4 wt% on catalyst) than the lower char+coke (~2.7 wt% on catalyst). In addition, differential thermogravimetric curve (DTG, in wt%/°C) shows that the upper coke is combustible at two different temperatures, 410°C and 530°C, respectively, in which the low temperature peak (410°C) is larger than the high temperature peak (530°C). The combustion of the lower coke occurs at 150°C, 410°C, and 530°C in which most the coke is combusted at 530°C. These results suggest that the upper coke is mostly char formed from homogeneous reactions of the pyrolysis products since combustion mainly occurs at low temperature (e.g. 410°C) [76]. In contrast, the lower char+coke is probably mostly coke formed from heterogeneous reactions in the catalyst pores where 530°C is required for combustion.

Figure 3.8. Picture of upper char+coke (>250 μm), lower char+coke (<250 μm), and the ZSM-5 catalyst after combustion of the char+coke.

3.2.6 Stability of the catalyst in reaction-regeneration cycles

To study the stability of the ZSM-5 catalyst during CFP, the catalyst was subjected to 30 successive reaction-regeneration cycles. The catalyst was exposed to a total reaction time of over 15 hrs and a total regeneration time of over 450 hrs. A total reaction time was calculated from the average catalyst residence time for each run (approximately 30 min). For each cycle the reaction was performed for 4 - 5 hrs at the standard conditions: temperature of 600°C, WHSV of 0.3 hr^{-1}, catalyst to biomass ratio of 6, fluidization gas flow rate of 5 slpm, and catalyst bed mass of 550 g. After reaction the spent catalyst was collected and regenerated in air at 580°C for 15 to 20 hr. Importantly, during the regeneration any ash accumulated on the catalyst surface was not removed as the spent catalyst was regenerated in crucible in the muffle furnace with stagnant air. The product yield and selectivity in successive reaction-regeneration cycles are shown in Figure 3.10. For the carbon yields of olefins, CO, CO_2, and methane, the catalysts after 5 and 30 reaction-regeneration cycles show similar results as compared to the fresh catalyst. However, there is a slight decrease in the aromatic yield from 14.2% to 13.1% after the fifth regeneration. Then, there is another decrease in the aromatic yield from 13.1% to 12.2% after the thirtieth regeneration. These results suggest that the catalyst loses a slight activity in successive reaction-regeneration cycles. However, a comparison between 5 cycles and 30 cycles shows that the decrease becomes less significant as the number of cycles increases.

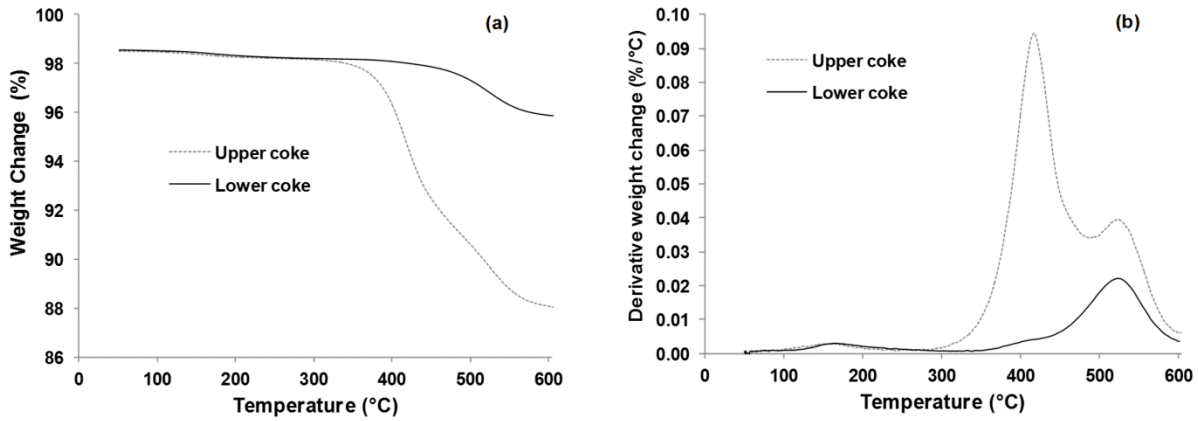

Figure 3.9. TGA (a) and derivative weight curves (b) in the combustion of upper char+coke and lower char+coke.

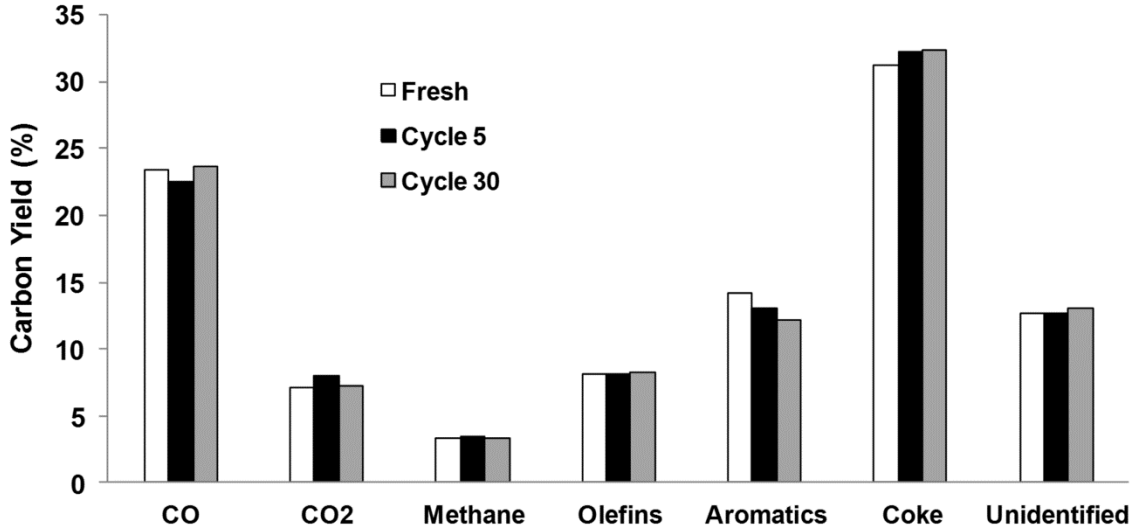

Figure 3.10. Catalytic fast pyrolysis of pine wood with a fresh ZSM-5, the ZSM-5 after 5 reaction-regeneration cycles, and the ZSM-5 after 30 reaction-regeneration cycles. Reaction conditions: 0.3 wood WHSV, catalyst to biomass ratio of 6, 600°C reaction temperature, 550 g of bed mass, 5 slpm N_2 fluidization flow rate, and 150 min total reaction time.

Figure 3.11 shows the X-ray diffraction patterns of the fresh ZSM-5 and the ZSM-5 after 30 reaction-regeneration cycles. The crystal structure and crystallinity of the ZSM-5 were intact after 30 reaction-regeneration cycles. SEM images were also recorded for the catalysts (Figure 3.12). Both catalysts had a broad range of particle sizes between 40 μm and 150 μm. There were no significant differences in particle sizes between two catalysts. However, the ZSM-5 catalyst after

30 reaction-regeneration cycles shows some broken pieces of catalyst particles. The particle attrition could result from the collision between catalyst particles in the fluidized bed reactor.

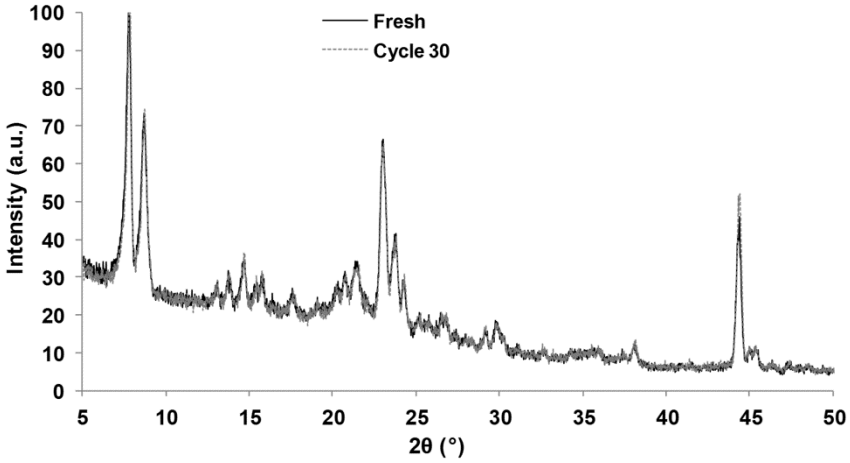

Figure 3.11. X-ray diffraction patterns of the fresh catalyst (black line) and the catalyst after 30 reaction-regeneration cycles (grey dotted line).

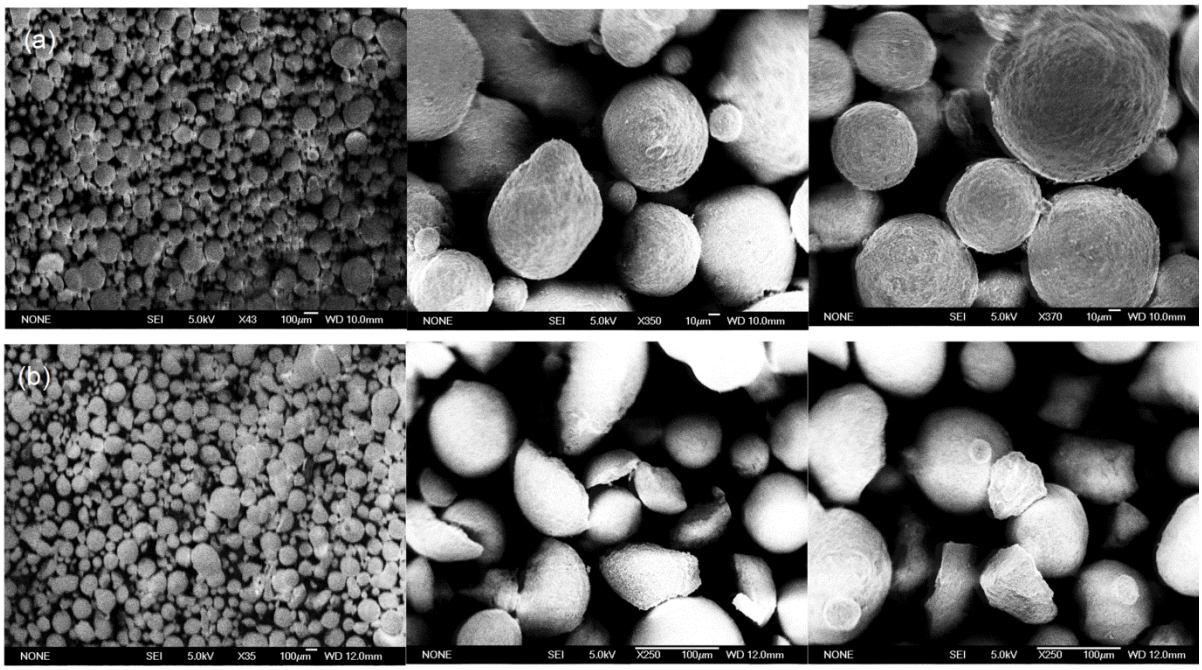

Figure 3.12. SEM images of (a) the fresh catalyst and (b) the catalyst after 30 reaction-regeneration cycles.

The crystallinity of the ZSM-5 is intact after 30 reaction-regeneration cycles, thus dealumination might not be the case. That crystallinity was maintained in the presence of product

steam at high temperature suggests hydrothermal stability of the catalyst. Another possibility for the slight decrease in activity is that mineral impurities from biomass could poison the acid sites of the ZSM-5. To test this possibility, the ZSM-5 catalyst, after 30 reaction-regeneration cycles, was subjected to elemental analysis to measure its mineral contents. As shown in Table 3.9, four common minerals in biomass, including Ca, K, Mg, and Mn are present up to 0.21% in the catalyst after 30 reaction-regeneration cycles. Thus, it is possible that these minerals deposited on the catalyst may poison the acid sites.

Table 3.9. Elemental analysis of the catalyst after 30 reaction-regeneration cycles.

Element	Fresh ZSM-5	ZSM-5 after 30 reaction-regeneration cycles
Calcium (wt%)	0	0.136
Potassium (wt%)	0	0.142
Magnesium (wt%)	0	0.211
Manganese (ppm)	0	131

3.3. Conclusions

Continuous production of aromatics and olefins from Catalytic Fast Pyrolysis (CFP) of wood was achieved in a specially designed process development unit (PDU), a bubbling fluidized bed reactor with continuous addition and removal of catalyst particles. The PDU can maintain the constant product yield and selectivity over an extended reaction period (e.g. 7 hrs). The yields and selectivity for aromatics and olefins were dependent on operating parameters: temperature, biomass WHSV, and catalyst to biomass ratio. Results obtained in the PDU were similar to results obtained in previous smaller bubbling fluidized bed reactors without catalyst addition. These results indicate that CFP can effectively produce aromatics and olefins from biomass in a continuous reactor. In addition, the hydrodynamics of the reactor can influence the product yields. For example, the fluidization gas velocity and catalyst bed height impact the product yield and

distribution. The lower gas velocity and smaller bubble size increased the aromatic yields up to 15.5% due to the increased vapor residence time and the improved mass transfer. The product gas, including CO, CO_2 and olefins could be recycled to serve as a fluidization gas during the operation. Olefins were converted into additional aromatics while CO and CO_2 were inert for CFP reaction. The spray-dried ZSM-5 catalyst was fairly stable during a repeated reaction-regeneration cycles. The catalyst maintained catalytic activity up to 30 successive reaction-regeneration cycles. However, although the crystallinity and porosity of the catalyst is intact, there were a loss in some of acid sites and mineral impurities after 30 reaction-regeneration cycles. The mineral impurities from the biomass might be the main source of poisoning for the acid sites.

CHAPTER 4

Effect of Steam on the Catalytic Fast Pyrolysis of Cellulose

Yang, H.; Coolman, R.J.; Karanjkar, P.; Wang, H.; Xu, Z.; Chen, H.; Moutziaris, T.J.; Huber, G.W., The Effect of Steam on the Catalytic Fast Pyrolysis of Cellulose. *Green Chemistry*, **2015** 17, 2912-2923.[77]

- My contribution to this work was construction (shared with Karanjkar, P.) and maintenance of the fluidized-bed reactor, data interpretation and experimental design and planning.
- Yang, H. (with the assistance of Wang, H.) collected all the data in this study and wrote the paper that this chapter is based on.
- Xu, Z. provided support for several of the analytical techniques used in this study.
- Chen, H.; Moutziaris, T.J. and Huber, G.W. were the primary investigators of this study.

4.1. Background

In contrast to fossil fuels, biomass feedstocks possess high contents of both moisture and oxygen.[2, 78, 79] Drying and dehydration reactions produce large amounts of steam during CFP, much of which condenses as water in the liquid-phase products.[80] Little is known about the effect of this steam on CFP chemistry. The presence of steam during un-catalyzed biomass pyrolysis is understood to change gas, char+coke, and liquid yields and promote the removal of oxygen from the liquid.[81] Williams, et al. found that the presence of steam during zeolite-catalyzed upgrading of oxygenated biomass pyrolysis vapors led to the formation of large amounts of gaseous products with a yield in excess of 70% at 550°C, proposing that water can act as H_2 donor.[82] Gilbert, et al. studied the influence of water on the conversion of furan over ZSM-5 and found that water hydrolyzes furans to produce more propylene and CO_2.[83]

In CFP, steam may also affect catalyst integrity. Iliopoulou et al. found that treatment of mesporous Al-MCM-41 at 550°C under a 20% steam atmosphere caused a significant reduction in acidity and porosity.[84] Ong, et al. found that steam treatment of ZSM-5 for 5hr at 450°C under a pure steam atmosphere caused irreversible dealumination through stable tetrahedrally-coordinated extra-framework aluminum neutralizing aluminum/oxygen tetrahedra in the lattice, thus reducing the number of Brønsted acid sites.[85] Corma et al. studied the steam catalytic cracking of naphtha over ZSM-5 at 650°C with a steam vapor fraction between 0% and 35.7% and found their catalyst underwent intense dealumination, cracking rates decreased after steam exposure times of 600 sec, and these effects are more apparent at higher temperatures.[86]

In addition to steam causing irreversible dealumination, previous research has demonstrated reversible deactivation as it can compete with reactant species (specifically n-heptane) for adsorption on active sites, thus negatively affecting the catalyst's activity.[87] Corma,

et al. found that post-synthesis treatment with phosphorous, introduced to enhance the hydrothermal stability, slowed down catalyst deactivation for steam catalytic cracking.[88] Lee, et al. found that the phosphorus-treated HZSM-5 (P/ZSM-5) exhibited lower acidity, higher hydrothermal stability and improved dimethyl ether (DME) selectivity in methanol conversion compared to the phosphorus-free HZSM-5.[89]

Zeolite catalysts used in fluidized beds are spray dried with a binder in order to obtain larger and more attrition-resistant particles with other desirable fluidization characteristics.[90] The presence of binder can affect catalyst behavior through (1) changes in the proton-exchange efficiency, (2) blocking of the zeolite channels, and (3) channels in the binder trapping coke precursors which cause a significant decrease in the amount of coke deposited on the zeolite.[91, 92]

The objective of this chapter is to elucidate the separate effects of (1) the long-term influences of steam's irreversible effects on the catalyst during CFP and how this affects product distribution, and (2) the interaction steam itself has with changing the product distribution through potentially acting as a homogeneous catalyst, a reactant species, or a heterogeneous catalyst site blocker.

The experimental apparatus for experiments shown in this chapter are shown in Figure 4.1. The fluidized bed reactor is a 316 stainless-steel 4.92-cm ID pipe with a freeboard height of 37 cm. Ninety grams of catalyst were loaded into the reactor; a loading corresponding to roughly 15% of the reactor volume. Prior to reaction, the catalyst was calcined in-situ at 600°C in air flowing at 600 sccm. Above the freeboard is a disengaging zone which expands to a 7.79-cm ID pipe. The catalyst bed is supported by a distributor plate made from two layers of 304 stainless-steel cloth (200 mesh) glued to a stainless-steel screen for support. The main reactor body and space beneath

the distributor plate (henceforth referred to as the plenum) were sealed together using bolted flanges.

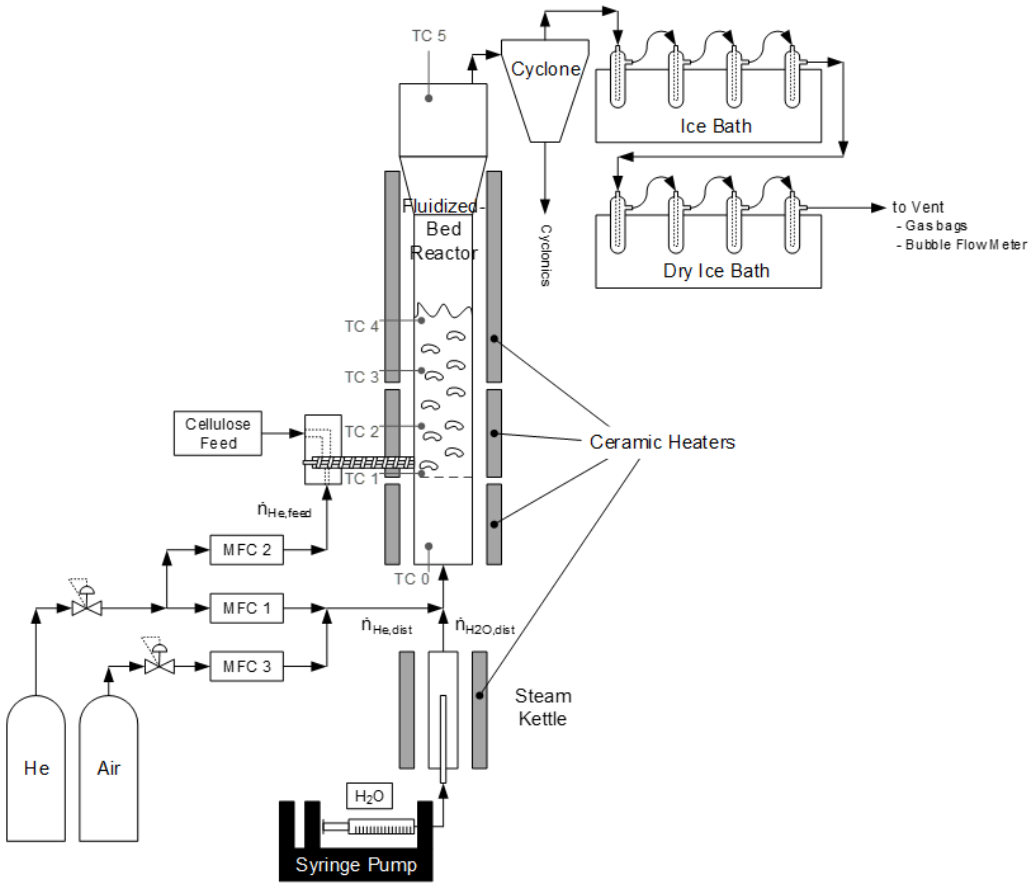

Figure 4.1. Flow diagram of bubbling fluidized bed for catalytic fast pyrolysis (CFP).

A typical run was carried out for 30 min time on stream. The catalyst was fluidized using helium and/or steam at a rate of 600 sccm (henceforth referred to as the fluidizer gas). Steam was delivered to the reactor using a syringe pump and in-line steam kettle. A stainless-steel auger equipped with a variable speed motor and rotary fitting fed cellulose into the side of the reactor. Cellulose was supplied to this auger via a sealed feed hopper (calibrated prior via balance and stopwatch). To maintain an inert environment and encourage the rapid delivery of biomass to the reactor, the hopper and augur were swept with helium at a rate of 400 sccm (henceforth referred

to as the feeding gas). Gas flows were selected to operate the reactor in the bubbling fluidized-bed regime. During the reaction, product gases exited the top of the reactor and were passed through a cyclone. The solid-free vapors were then bubbled through four condensers each containing ~20 ml isopropanol maintained at 0°C using an ice bath. Here, most organic species were captured through dissolution. The stream was then passed through four condensers maintained at -55°C using a dry-ice/acetone bath to condense remaining organics. The non-condensable gases were then either vented, plumbed through a soap-film flow meter, or sampled in Tedlar gas bags (Restek) for GC analysis. After cellulose feeding, the reactor was purged with 1000 sccm of helium for another 30 min to ensure a complete purge of all volatile organic products. The condensers were then removed and rinsed with isopropanol to collect all product liquids. The volume of isopropanol/product solution was recorded and analyzed via GC to quantify products.

After feeding and purge, the reactor temperature was increased to 600°C, and the carrier gas was switched to air for two hours combust char+coke and regenerate the catalyst. As described in Chapter 1, gravimetric analysis with Ascarite was performed to calculate char+coke yields.

A Perkin-Elmer-emission spectrometer plasma 400 was used to do elemental analysis of the catalyst. A 100-mg sample of catalyst was completely dissolved in 2 ml of hydrofluoric acid (50%) and several drops of boric acid (7%) were added to protect against the formation of volatile SiF_4. The solution was heated at 80–90°C for seven minutes to allow some of the hydrofluoric acid to evaporate before cooling. About 2ml of nitric acid (10%) and several ml of boric acid (7%) were added to the solution, then water was added to bring the solution volume to 50 ml.

The acidity of the samples was measured using Temperature Programmed Desorption (TPD) of isopropylamine (IPA-TPD) and ammonia (NH_3-TPD) using a Micromeritics® Autochem II 2920 with an inline Thermal Conductivity Detector (TCD). Before testing, the

catalyst was heated up to 600°C for 2hr in helium to remove adsorbed water or organic species. For IPA-TPD, once the 100-mg sample was saturated with IPA at 50°C for 20min, helium was flushed at 50sccm for 2hr in the temperature range of 50-700°C at a heating rate of 10°C/min. For NH_3-TPD, once the 100-mg sample was saturated with NH_3 at 100°C for 30 min, helium was flushed at 12sccm for 2hr in the temperature range of 150-700°C at a heating rate of 5°C/min. The number of Brønsted acid sites was calculated based on the TCD signal for NH_3 and propylene, the products of IPA decomposition. The total number of acid sites was calculated based on the TCD signal for NH_3. The number of Lewis acid sites was taken as the difference between the total number of acid sites and the number of Brønsted acid sites.

The zeolite crystallinity was determined by a Bruker D8 Discover diffractometer using CuKa radiation (l=1.542 Å). The scattering angle 2θ was varied from 5° to 60°. The crystal size was calculated using the Scherrer equation.

The BET surface area and pore volume of the samples were calculated by N_2 adsorption/desorption isotherms obtained at-196^{o}C using a Micromeritics, ASAP2020 adsorption analyzer. Prior to N_2 adsorption, the samples were degassed at 300°C overnight under vacuum.

The particle size distribution and surface morphology of catalyst was measured with a scanning electron microscope (SEM, LEO 1550 VP).

4.2. Results and discussion

4.2.1 Effect of steam partial pressure on product yields and selectivity

To test the effect of steam's presence on CFP of cellulose, some fraction of the input carrier helium gas was replaced with an equivalent molar flowrate of steam. The fraction of steam was varied over a range of 0% to 60%. This upper bound of 60% represents a fluidization gas completely entirely made up of steam (600 sccm) and a feed gas consisting of helium (400 sccm).

The hydrodynamic parameters are listed in Table 4.1. Average bubble size, rise velocity and residence times for each phase were affected more-so by outlet gas flow rate than input composition. Regardless, these hydrodynamic properties were predicted to remain relatively stable throughout the range of vapor fraction tested.

Table 4.1. Estimated average bubble size, bubble residence time, and expanded bed height as estimated from Assemblage Model. Temperature: 500°C, WHSV: 0.4 hr^{-1}, bed mass: 90 g, time on stream: 30 min, Fluidizer gas: He/Steam mix @ 600 sccm, Feeding Gas: He @ 400 sccm.

Parameter	**Definition**					
Input steam fraction (%)	Steam vapor fraction / (Fluidizer gas + Feed gas)	0%	5%	24%	40%	60%
Outlet gas flowrate (sccm)	Measured by volume flow meter	1,609	1,667	1,715	1,438	1,479
Steam partial pressure (torr)	Steam flow rate / Outlet gas flow rate × Reactor pressure	0	25	109	211	310
$d_{b.ave}$ (cm)	Average bubble diameter over the height of the bed	0.83	0.85	0.87	0.8	0.81
$u_{b.ave}$ (cm/s)	Average bubble rise velocity over the height of the bed	33.02	33.46	33.83	32.04	32.3
δ (%)	Fraction of the bed occupied by the bubble phase	11.61	11.98	12.28	10.79	11.01
L_f (cm)	Height of the fluidized bed	8.55	8.59	8.62	8.47	8.49
Expansion (%)	% height increase from packed to fluidized bed	41.41	42.01	42.5	40.12	40.47
τ_f (s)	Average gas residence time in the fluidized bed	1.2	1.16	1.14	1.32	1.29
τ_e (s)	Gas residence time in the emulsion phase	19.18	22.35	26.18	26.65	25.73
τ_b (s)	Gas residence time in the bubble phase	0.26	0.26	0.26	0.27	0.27

Figure 4.2 shows the product carbon yields at different steam vapor fractions in the range of 0-41%. A fresh catalyst was loaded into the reactor prior to each reaction test. The main products include aromatics, olefins, CH_4, CO, CO_2, char+coke, and some light oxygenates. The aromatics consisted of benzene, toluene, ethyl-benzene, xylenes, styrene, indene, and naphthalene. The

identifiable oxygenates consisted of benzofuran, phenol, acetyaldehyde, acetic acid, hydroxyacetone, and 5-hydroxymethyl furfural.

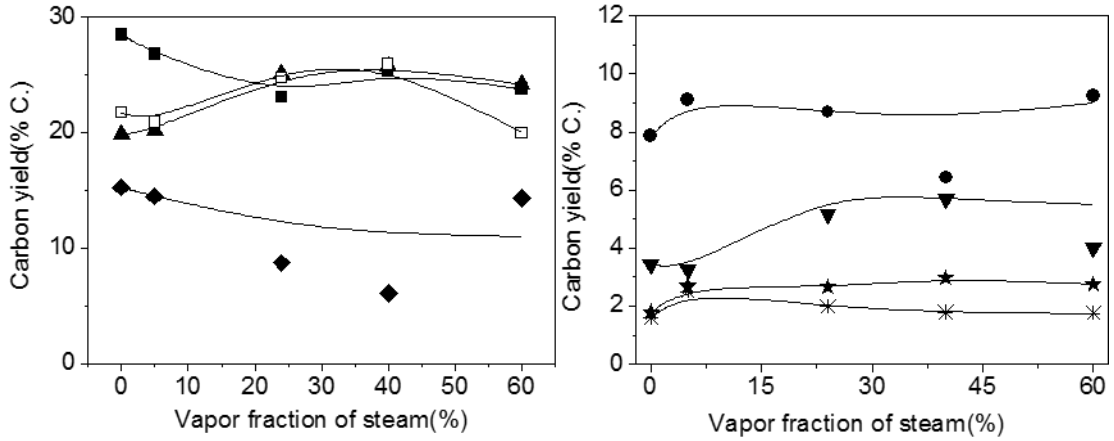

Figure 4.2. Carbon yield as function of input vapor fraction of steam for catalytic fast pyrolysis of cellulose with fresh ZSM-5 catalyst. (Reaction conditions: Cellulose feed, WHSV: 0.4 hr^{-1}, Temperature: 500°C, time on stream: 30 min, 90 g catalyst.) Key: ■:Aromatics ▲:CO ◆:Char+Coke ●:Olefins ▼:CO_2 ★:Methane *:Identifiable Oxygenates □:Unidentified carbon

The aromatic yield decreased linearly from 28 to 22% as input vapor fraction of steam increased from 0% to 24%, but remained close to 22% yield with further increases to steam vapor fraction. Carbon monoxide showed a trend contrary to aromatics, increasing with steam vapor fraction (perhaps as H_2O reacted with char+coke precursors) up to 24% steam. The char+coke yield decreased from 15 to 5% as the steam fraction increased from 0% to 40% and then it increased with further steam vapor fraction. Olefins, methane, and identifiable oxygenate yields showed no obvious change with steam vapor fraction. The yield of unidentified carbon not detected in any of the product phases (calculated as the balance carbon of the cellulose feed, presumed to be larger oxygenated compounds) increased with increasing vapor fraction of steam and reaching the maximum yield at 27%, and then decreasing.

The aromatics selectivity did not change with input vapor fraction of steam, as shown in Figure 4.3. Benzene and toluene were the two main liquid products at these reactions conditions,

each with a selectivity of about 35%. However, the olefin selectivity did change with steam vapor fraction, as shown in Figure 4.4. Increasing the steam vapor fraction increased the ethylene selectivity and decreased the propylene selectivity. The amount of butenes and pentenes was very low and no clear change was shown with respect to steam vapor fraction.

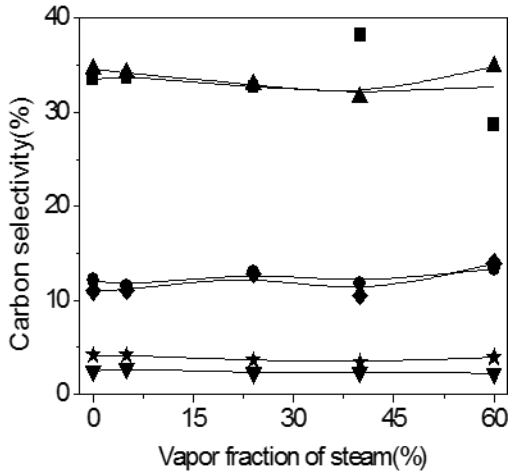

Figure 4.3. Aromatic carbon selectivity as function of input vapor fraction of steam for catalytic fast pyrolysis of cellulose with ZSM-5 catalyst. (Reaction conditions: Cellulose feed, WHSV: 0.4hr^{-1}, Input steam fraction: 60%, Temperature: 500°C, time on stream: 30 min, 90 g catalyst.) Key: ■:Benzene ▲:Toluene ◆:Xylenes+Ethylbenzene ●:Napthalenes, ▼:Styrene ★:Indene

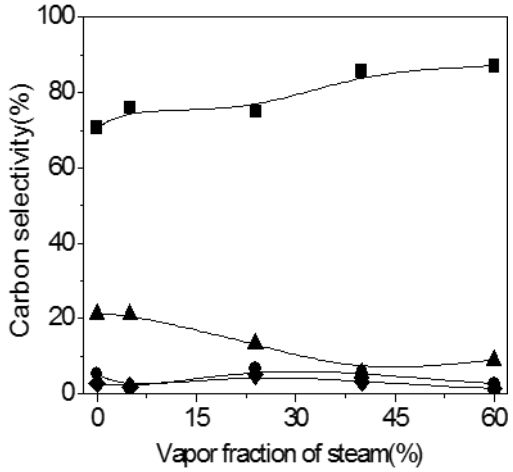

Figure 4.4. Olefin carbon selectivity as function of input vapor fraction of steam for catalytic fast pyrolysis of cellulose with ZSM-5 catalyst. (Reaction conditions: Cellulose feed, WHSV: 0.4hr^{-1}, Input steam fraction: 60%, Temperature: 500°C, time on stream: 30 min, 90 g catalyst.) Key: ■:Ethylene ▲:Propylene ◆:Butenes ●:Pentenes

4.2.2. Effects of alternating no-steam and steam

The data in the previous section were collected with fresh catalyst for each run. These data offered little insight as to whether these trends were driven due to steam causing irreversible changes to the catalyst, or steam itself interfering with the reactions of pyrolysis and/or catalysis. To elucidate this matter, a series of cellulose CFP reactions were performed over a single 90-g batch of catalyst wherein the fluidizer gas was alternated as helium and steam (Temp. = 500°C, WHSV = 0.4hr^{-1}, time-on-stream = 30 min, fluidizer flow = 600sccm.) At the conclusion of these "no-steam/steam runs", the catalyst had been exposed to steam for a total of 330 min, though the catalyst had been run through cellulose CFP for a time roughly twice that. A small amount of catalyst (~1.0 g) was extracted after each steam run for analysis.

4.2.3. Influence of steam on catalyst

4.2.3.1. Brønsted:Lewis Ratio Via TPD

Figure 4.5 shows the catalyst acidity as a function of steam exposure time during cellulose CFP. The Brønsted acidity undergoes a 25% decrease during the first 30 min of steam exposure followed by a gradual decrease. The Lewis acidity increased with steam exposure, suggesting that Brønsted sites converted to Lewis sites as the catalyst underwent dealumination as described by Ong et al.[85]. The total acidity of the catalyst decreased from 114μmol/g to 42μmol/g. This analysis shows that the most significant acidity changes occur during the initial 30 min of exposure to steam.

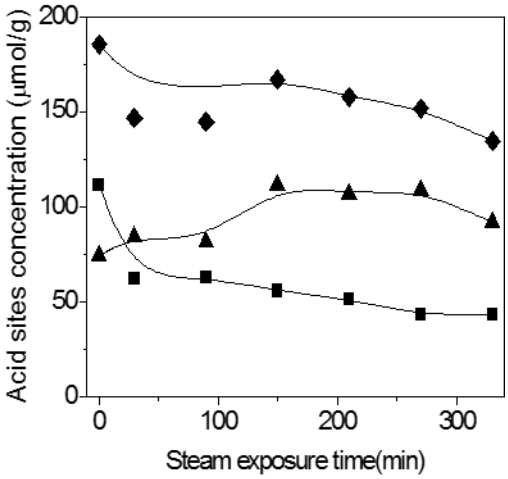

Figure 4.5. Catalyst acid-site concentration as a function of steam exposure time. (Reaction conditions: Cellulose feed, WHSV: 0.4hr^{-1}, Input steam fraction: alternating between 0% and 60%, Temperature: 500°C, time on stream: 30 min, 90 g catalyst.) Key: ■:Brønsted sites ▲:Lewis sites ◆:Total acid sites

4.3.3.2. Si:Al Ratio via ICP

As shown Figure 4.6, ICP analysis showed that the Al and Si content within the catalyst (consisting of both zeolite and binder) did not change after steam exposure. Other researchers observed loss of framework aluminum in the presence of steam, though at higher temperatures. Corma, et al. found that a 35% steam atmosphere can remove some ZSM-5 framework Al during catalytic cracking of naphtha for production of propene and ethane at 500-700°C when vapor fractions of steam exceed 17.8%.[86] Iliopoulou, et al. also found that steam presence decreases the acidity and Al content of MCM-41 at 550°C and 750°C for vapor fractions of steam of 20%.[84]

The phosphorus content was also measured via ICP and found to be stable with steaming, remaining at a value of ~3.85%wt as shown in Figure 4.6. Both binder and phosphorus have been reported to inhibit the volatilization of framework aluminum via steaming.[89, 93]

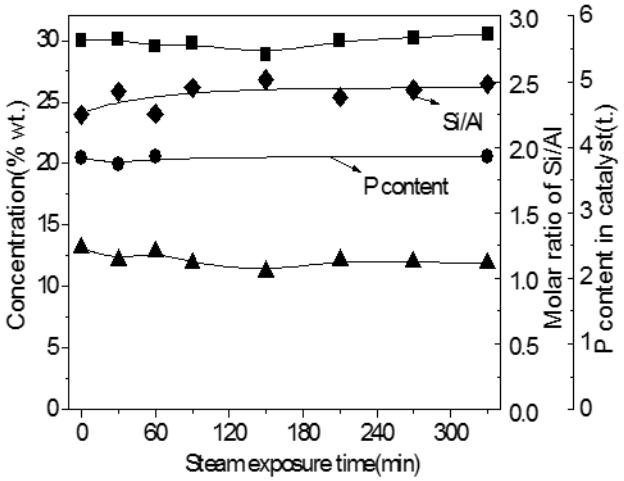

Figure 4.6. ZSM-5 Si and Al concentrations as a function of steam exposure time. (Reaction conditions: Cellulose feed, WHSV: 0.4hr^{-1}, Input steam fraction: alternating between 0% and 60%, Temperature: 500°C, time on stream: 30 min, 90 g catalyst.) Key: ■:Si concentration ▲:Al concentration ◆:Si:Al molar Ratio ●:P concentration

4.3.3.3. Crystallinity via XRD

The powder XRD patterns of the steamed ZSM-5 samples are shown in Figure 4.7A. The intensity and peak positions of all of the zeolite samples are in good agreement with previously reported spectra, including typical diffraction peaks at 2θ = 7.88° (011), 8.76° (020), 23.0° (501), 23.84° (033) and 24.3° (133).[94, 95] No change in the XRD peak positions or new peaks appeared after steam exposure. However, the zeolite crystal size increased from ~50 nm to ~80 nm after a steam exposure time of 60 min and remained stable with further steaming as shown in Figure 4.7B. This decrease in crystallite size may cause further decreases in catalyst activity by decreasing diffusion limitations.[96-98]

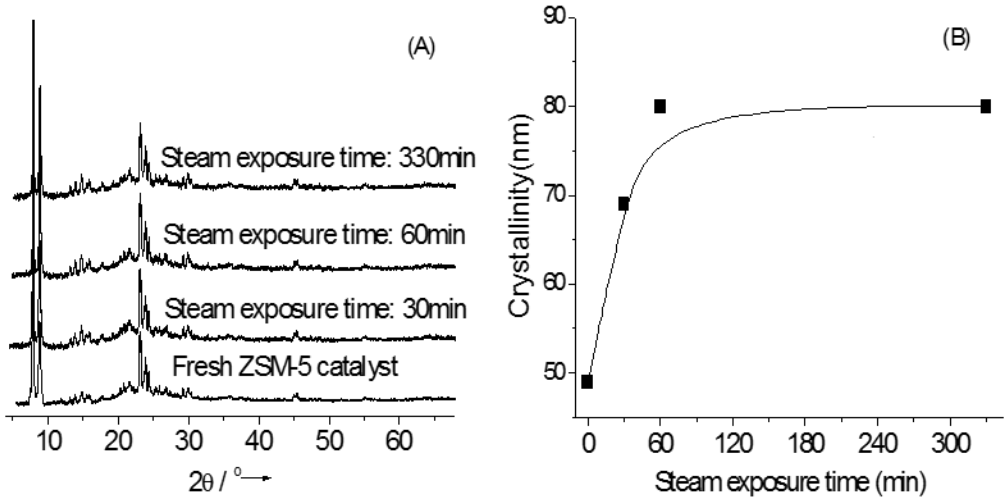

Figure 4.7. XRD pattern of steamed ZSM-5 catalyst. (Reaction conditions: Cellulose feed, WHSV: 0.4hr^{-1}, Input steam fraction: alternating between 0% and 60%, Temperature: 500°C, time on stream: 30 min, 90 g catalyst.) A: XRD pattern; B: Crystallinity of ZSM-5 catalyst

4.3.3.4. Porosity via nitrogen adsorption

The BET surface area and pore volume distribution based on liquid N_2 isothermal adsorption at -196°C are shown in Table 4.2 and Figure 4.8, as calculated from methods described by Sing et al.[99]. Because these calculations rely on BET theory (which makes assumptions not applicable to microporous materials) these measurements are intended only be used in relation to one-another, an in a relative (and not an absolute) sense. The surface area, the micropore (<2 nm) area, and the mesopore (3–4 nm) volume increased during the first 30 min of steaming. As micro- and meso-pores are necessary for the formation of aromatics, this increased pore population most likely increases the formation of aromatic products[33]. In contrast, the volume of macropores (>50 nm) decreased with steaming in the first 30 min. Since these large pores are located between zeolite crystals and within the binder, this suggests that macropores collapsed with steam exposure, a finding which is consistent with the increase in zeolite crystallite size as shown from the XRD measurements. With fewer macropores, micropores are more susceptible to blockage by char+coke, thus inhibiting the formation of the hydrocarbon pool, and lowering the catalyst

activity[100, 101]. The micropore area and micropore volume both decreased below their initial values at 330 min steam exposure time. The population of large macropores (>50 nm) did not change substantially after its initial change within the first 30 min, suggesting that at this time the macropores had finished collapsing and the zeolite crystals began the process of fusing. The SEM images shown in Figure 4.9 qualitatively further confirmed this result.

Table 4.2. BET surface area and pore volume parameters of steamed catalyst. (Reaction conditions: Cellulose feed, WHSV: 0.4hr^{-1}, Input steam fraction: alternating between 0% and 60%, Temperature: 500°C, time on stream: 30 min, 90 g catalyst.)

Sample	BET SurfaceArea (m^2/g)	External surface area* (m^2/g)	Micropore area* (m^2/g)	Micropore volume (cc/g)	Average pore size (nm)
Fresh catalyst	108.86	36.93	130.19	0.04	7.06
30 min	156.1	38.44	187.89	0.0598	4.49
60 min	145.67	50.89	219.11	0.0486	3.73
330 min	109.48	49.81	112.61	0.0314	5.13

*External surface area, micropore area, and pore volume derived based on t-plot method, Average pore size is calculated with 4V/A by BET. Determined from the N_2 isothermal uptake at P/P_0:0.10–0.90 at -196°C

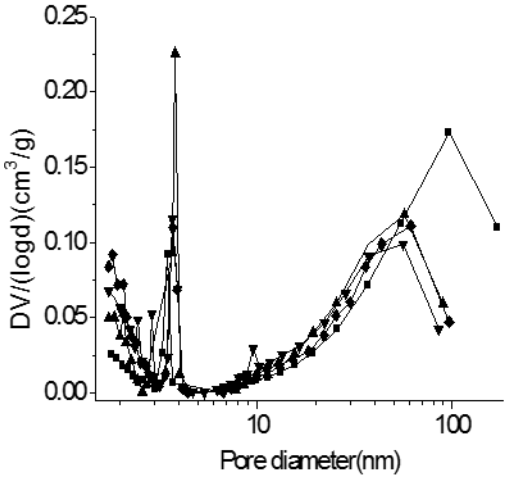

Figure 4.8. Mesopore size distributions determined from BJH adsorption, (Reaction conditions: Cellulose feed, WHSV: 0.4hr^{-1}, Input steam fraction: alternating between 0% and 60%, Temperature: 500°C, time on stream: 30 min, 90 g catalyst.) Key: ■:fresh catalyst ▲:30 min of steaming ▼:60 min of steaming ◆:330 min of steaming

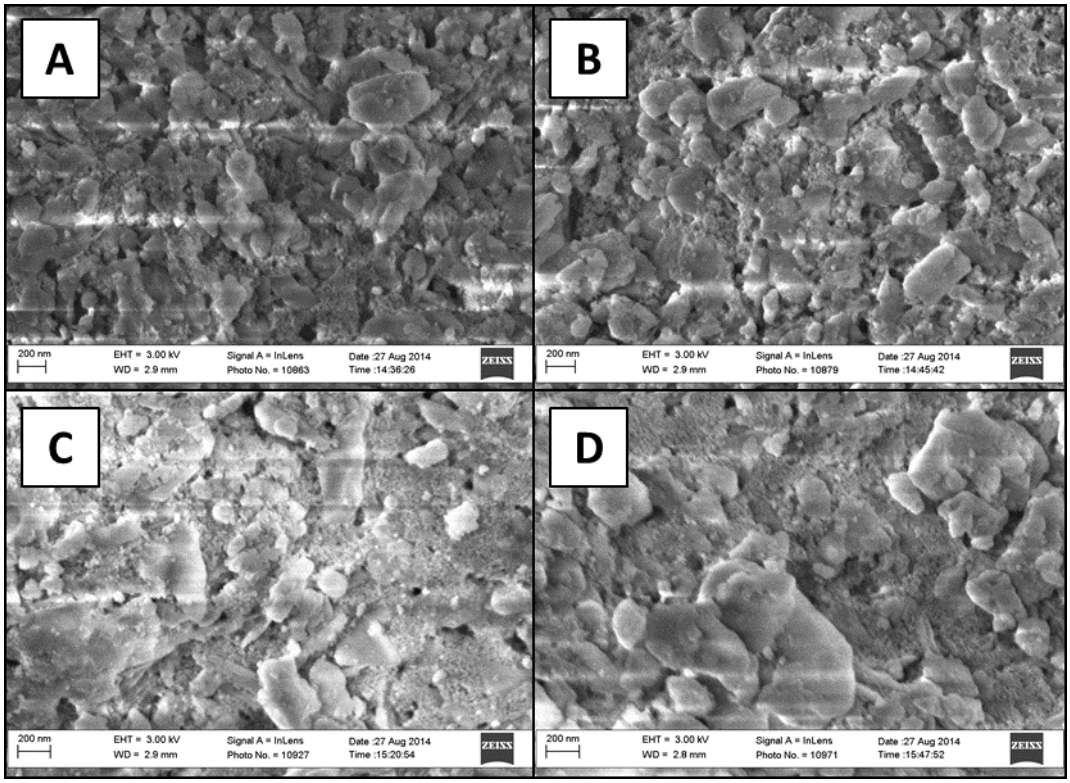

Figure 4.9. Surface morphology of steamed catalyst based on SEM. (Reaction conditions: Cellulose feed, WHSV: 0.4hr^{-1}, Input steam fraction: alternating between 0% and 60%, Temperature: 500°C, time on stream: 30 min, 90 g catalyst.) A:fresh catalyst B:30 min of steaming C:60 min of steaming D:330 min of steaming

4.3.3.5. Particle size distribution and Physical integrity via SEM

The particle size distribution was determined via SEM as shown in Figure 4.10 and Figure 4.11. Fresh catalyst particles are almost exclusively spherical, but with a large fraction of fines (<20µm). In the first 30 min of steaming, the largest difference is the loss of these fines, though the peak population size above 20µm does increase slightly from 40µm to 50µm, suggesting that the particles are already beginning to agglomerate. With further steam exposure (60 min), the particles agglomerated further and shifted the peak population size to 90µm. More irregularly-shaped particles appear as smaller particles become agglomerated with larger particles as shown in Figure 4.11. Above a steam exposure time of 60 min, the particles appear to have finished

agglomerating, as the peak population size remains at 90μm. Past 60 min however, more catalyst fragments appear, suggesting that catalyst attrition becomes important at longer durations of use, though this will be true regardless of whether there is steam present in the reactor.

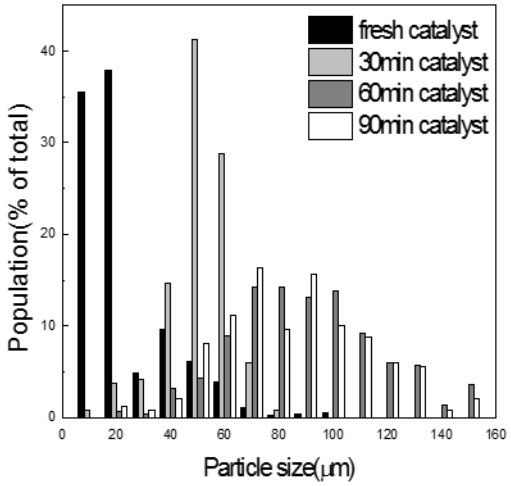

Figure 4.10. Particle size distribution of steamed catalyst based on SEM. (Reaction conditions: Cellulose feed, WHSV: 0.4hr^{-1}, Input steam fraction: alternating between 0% and 60%, Temperature: 500°C, time on stream: 30 min, 90 g catalyst.)

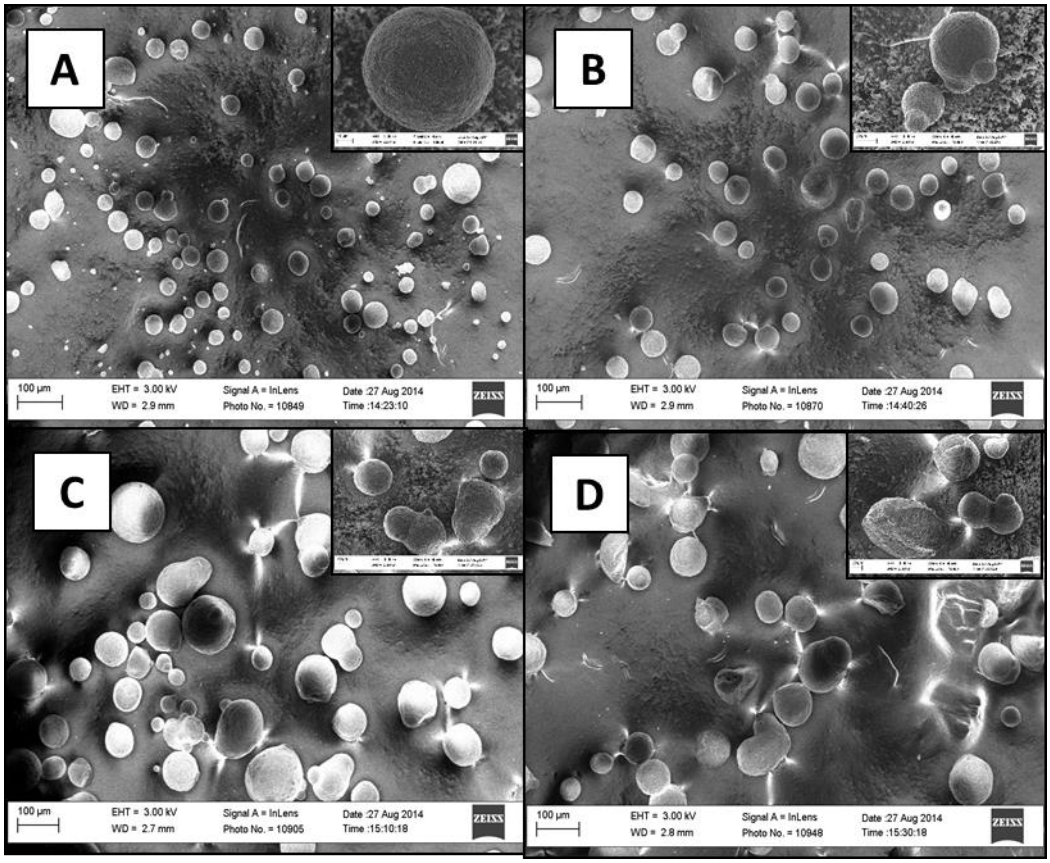

Figure 4.11. SEM images of typical catalyst particles at various stages of steaming. Inset photos show examples of various stages of particle agglomeration. (Reaction conditions: Cellulose feed, WHSV: 0.4hr^{-1}, Input steam fraction: alternating between 0% and 60%, Temperature: 500°C, time on stream: 30 min, 90 g catalyst.) A:fresh catalyst B:30 min of steaming C:60 min of steaming D:330 min of steaming

4.3.3.6. Influence of steam on product yields

Figure 4.12 shows the progress of product yields for the alternating no-steam/steam runs as a function of steam-exposure time. The data have been separated into runs performed without steam co-feeding (Figure 4.12A and Figure 4.12C) and with steam co-feeding (Figure 4.12B and Figure 4.12D). Clearly, steaming changes the product yield. For the CFP runs without steam co-feeding, the yield of aromatics decreased gradually from 29 to 18% over the course of steaming. The char+coke yield decreased from 15 to 7.8% over the course of steaming, while the olefin and methane yields showed a gradual increase. The CO and CO_2 both went through a maximum yield

at 60 min and 30 min of steaming respectively, gradually decreasing thereafter. The identified oxygenates increased slightly from 1.5 to 3% in the first 60 min but remained stable thereafter. The results indicate that the product yields are greatly affected by the structural changes to the catalyst induced by steam exposure, as most changes to the catalyst properties do change before 90 min of steam exposure as shown in Figure 4.5 through Figure 4.11. The pore-size distribution doesn't change after 30 min of steam exposure, crystal growth stops occurring after 60 min steam exposure, and the particle size distribution doesn't change after 60 min steam exposure. Past steam exposure times of 60 min, the yields of aromatics, char+coke, CO, and CO_2 seem to correlate with decreases in Brønsted acidity. The unidentified balance carbon increased with steam exposure, suggesting that heavier unidentifiable oxygenated species were produced in greater amounts as the catalyst underwent these changes.

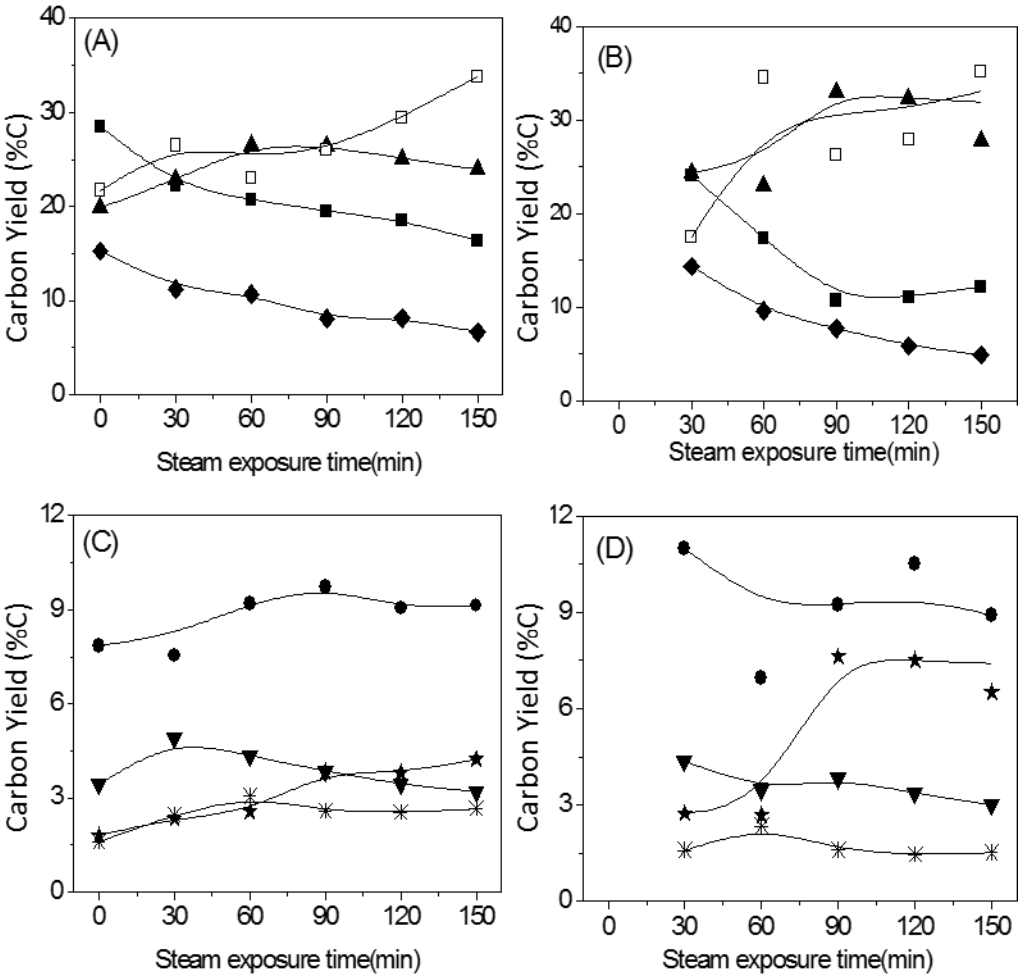

Figure 4.12**.** Carbon yield as function of catalyst steam exposure time for catalytic fast pyrolysis of cellulose with ZSM-5 catalyst. (Reaction conditions: Cellulose feed, WHSV: 0.4hr^{-1}, Input steam fraction: alternating between 0% and 60%, Temperature: 500°C, time on stream: 30 min, 90 g catalyst.) A,C: Without steam co-feeding; B,D: With steam co-feeding. Key: ■:Aromatics ▲:CO ◆:Char+Coke □:Unidentified Carbon ●:Olefins ▼:CO_2 ★:Methane *:Identifiable Oxygenates

For CFP runs with steam co-feeding, the changes in the product yield can be divided into two ranges: before and after the first 90 min. With steam co-feeding, the carbon yield of aromatics decreased from 24% to 10% in the first 90 min, but remained constant after. CO and methane showed the opposite tendency and their yields became enhanced particularly in the first 90 min, and remained somewhat constant with further steaming. With steam co-feeding, the char+coke yield decreased gradually from 15% to 5% over the entire 150 min of steam exposure. The CO_2

yield slightly decreased from 4% to 3%. The olefin yield for steam co-feeding did decrease over the span of steaming, though these results are noisy in the range of <90 min, so it cannot be said whether this change was abrupt (as with aromatics, CO and methane), or gradual (as with char+coke and CO_2). The identifiable oxygenate species yield was stable at about 1.5%. As was the case without steam co-feeding, unidentified balance carbon increased with steam exposure, again suggesting that heavier unidentifiable oxygenated species were produced in greater amounts as the catalyst underwent changes.

4.3.3.7 Influence of steam on aromatic and olefin selectivities

The aromatic selectivity changed over the course of steam-exposure time as shown in Figure 4.13. For runs without steam co-feeding (Figure 4.13A), the aromatic selectivities did not change. For runs with steam co-feeding (Figure 4.13B), the first 90 min of steaming caused the benzene selectivity to increase and the toluene selectivity to decrease. The carbon selectivity of xylenes decreased while that of styrene increased in that same period. The napthalenes and indene selectivities did not change. After 90 min of steam exposure, all the selectivities were fairly constant. These results suggest that changes to the catalyst (such as decreases in the amount of Brønsted acidity, shrinking of mesopore area, and increases in zeolite crystallinity) did not show great influence on aromatics selectivity, but the presence of steam did enhance the formation of toluene over benzene in the first 30 min.

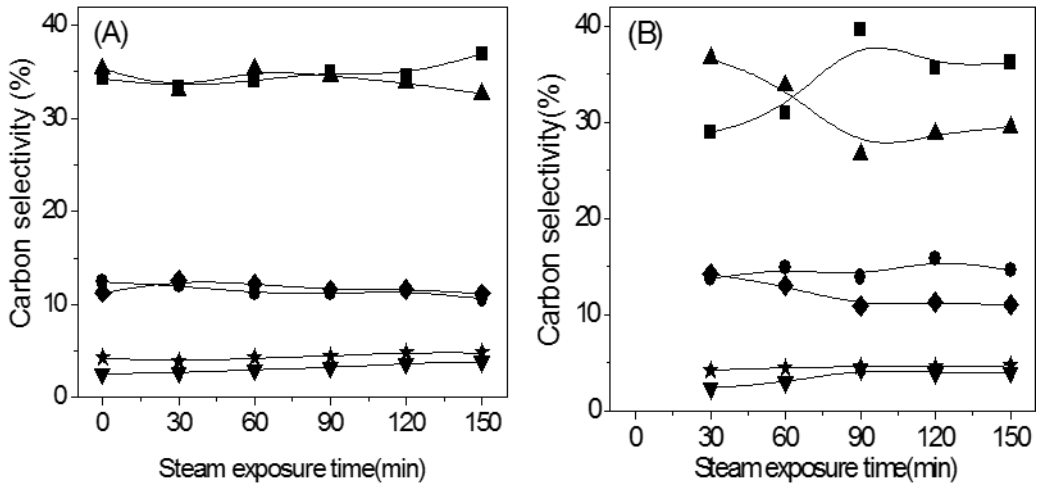

Figure 4.13. Aromatic carbon selectivity as function of steam co-feeding time for catalytic fast pyrolysis of cellulose with ZSM-5 catalyst. (Reaction conditions: Cellulose feed, WHSV: 0.4hr^{-1}, Input steam fraction: alternating between 0% and 60%, Temperature: 500°C, time on stream: 30 min, 90 g catalyst.) A: Without steam co-feeding; B: With steam co-feeding. Key: ■:Benzene ▲:Toluene ◆:Xylenes+Ethylbenzene ●:Napthalenes ▼:Styrene ★:Indene

The ethylene selectivity increased and the propylene selectivity decreased with steam exposure time for runs both with and without steam co-feeding as shown in Figure 4.14. The shift in both data sets is similar, even though steam co-feeding consistently produces more ethylene than without steam co-feeding. In both cases, the yields of butenes and pentenes is quite low (<1%), and steam co-feeding had no observable effect during the process of cellulose CFP.

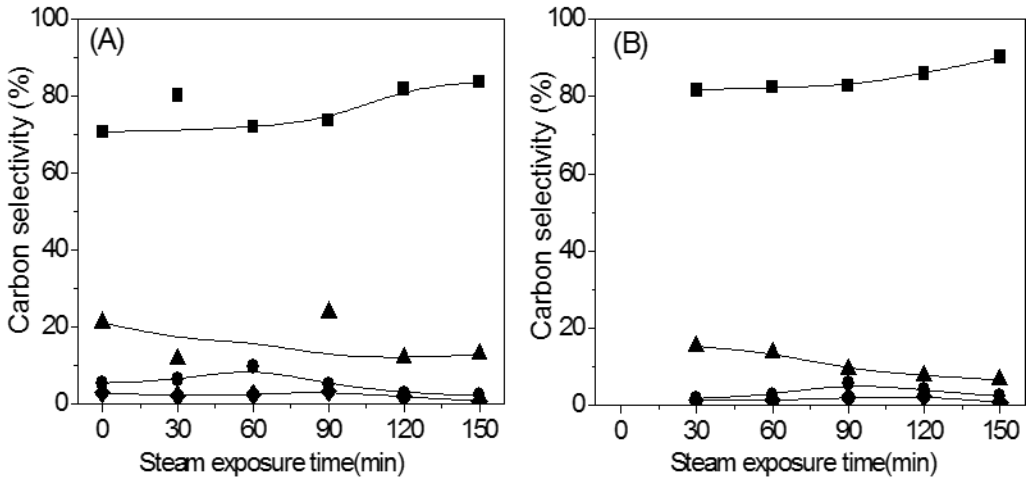

Figure 4.14. Olefin carbon selectivity as function of steam co-feeding time for catalytic fast pyrolysis of cellulose with ZSM-5 catalyst. (Reaction conditions: Cellulose feed, WHSV: 0.4hr^{-1}, Input steam fraction: alternating between 0% and 60%, Temperature: 500°C, time on stream: 30 min, 90 g catalyst.) A: Without steam co-feeding, B: With steam co-feeding. ■:Ethylene ▲:Propylene ◆: Butenes ●:Pentenes

4.2.4. Influence of steam on homogeneous and heterogeneous reactions

Student's t-test was performed to distinguish between (1) the long-term influences of steam's irreversible effects on the catalyst during CFP and how this affects product distribution, and (2) the interaction steam itself has with changing the product distribution through potentially acting as a homogeneous catalyst, a reactant species, or a heterogeneous catalyst site blocker. The results are shown in Table 4.3. Three runs were taken from each no-steam/steam data set. In each case, the data selected had a steam exposure time greater than 90 min because before this point, product yields changed too rapidly for an average to have any meaning. Although product yields do change after 90min, for the runs selected, an average is representative. The average ($\bar{x}$) and standard deviation (s) are shown for each group and compound in each data set. Also shown is the t-statistic (t) and whether this value is statistically significant to within 95% confidence (and in which direction). Within the confines of 95% confidence, steam co-feeding was found to decrease

the yields of aromatics, char+coke, and identifiable oxygenates, and increase the yields of methane and CO. No measurable change in the yield of CO_2 was observed.

Table 4.3. The influence of steam on cellulose CFP based on Student's t-test (Reaction conditions: Cellulose feed, WHSV: 0.4hr^{-1}, Input steam fraction: alternating between 0% and 60%, Temperature: 500°C, time on stream: 30 min, 90 g catalyst.) $\bar{x}$ = sample mean, s = sample standard derivation, t = t-statistic, 1-α = confidence level, t_{crit} = threshold of statistical significance according to chosen α. "↑" indicates a statistically significant increase, "↓" indicates a statistically significant decrease, and "—" indicates no statistically significant change.

	no steam (n = 3)		steam (n = 3)			α = 5%
	$\bar{x}$	s	$\bar{x}$	s	t	$t_{crit} = \pm 2.78$
CO	**25.16%**	**1.25%**	**31.89%**	**3.94%**	**2.82**	↑
CO_2	**3.49%**	**0.33%**	**3.54%**	**0.65%**	**0.12**	—
Char+Coke	**7.62%**	**0.84%**	**5.51%**	**0.51%**	**-3.7**	↓
Methane	**3.95%**	**0.24%**	**7.45%**	**0.92%**	**6.39**	↑
Aromatics	**17.46%**	**1.65%**	**11.16%**	**0.58%**	**-6.24**	↓
Benzene	6.19%	0.41%	3.94%	0.23%	-8.19	↓
Toluene	5.89%	0.72%	3.19%	0.20%	-6.28	↓
Xylenes	1.58%	0.23%	0.89%	0.05%	-5.1	↓
Naphthalene	1.94%	0.25%	1.82%	0.25%	-0.59	—
Ethyl-Benzene	0.42%	0.02%	0.36%	0.03%	-3.96	↓
Styrene	0.62%	0.02%	0.44%	0.03%	-8.72	↓
Indene	0.82%	0.06%	0.52%	0.04%	-7.31	↓
Olefins	**9.31%**	**0.36%**	**10.16%**	**1.09%**	**1.28**	—
C_2	7.33%	0.49%	9.06%	1.02%	2.64	—
C_3	1.49%	0.61%	0.73%	0.12%	-2.12	—
C_4	0.18%	0.11%	0.14%	0.11%	-0.47	—
C_5	0.31%	0.14%	0.23%	0.18%	-0.58	—
Id. Oxygenates	**3.26%**	**0.09%**	**2.06%**	**0.07%**	**-18.22**	↓
Benzofuran	0.22%	0.01%	0.20%	0.00%	-2.24	—
Phenol	0.45%	0.05%	0.41%	0.02%	-1.49	—
Hydroxyacetone	0.11%	0.01%	0.06%	0.02%	-4	↓
HMF	0.60%	0.04%	0.63%	0.10%	0.4	—
Acetylaldehyde	0.85%	0.04%	0.43%	0.08%	-8.47	↓
Furan	0.96%	0.09%	0.31%	0.08%	-9.6	↓
2-MF	0.05%	0.09%	0.02%	0.04%	-0.53	—
Acetic acid	0.01%	0.00%	0.01%	0.01%	-2.35	—
TOTAL	**70.24%**	**3.92%**	**71.77%**	**6.76%**	**0.34**	—
Unidentified Carbon	29.76%	3.92%	28.23%	6.76%	0.34	—

Steam co-feeding decreased the yield of all aromatics species except naphthalene, though any changes to olefin yields were not statistically significant. For oxygenates, steam co-feeding decreased the yield of acetylaldehyde, furan and hydroxyacetone, though no measurable influence was observed for other oxygen-containing species detected.

Worth noting is the near statistical significance in the yield changes in ethylene and propylene. While the effects at this level of confidence are not measurable within this sample size, these results do suggest that there may be an effect of steam co-feeding that causes an increase in the yield of ethylene and a decrease in the yield of propylene. These results run contrary to the work of Gilbert et al. who showed for furan CFP, more propylene is formed with steam co-feeding.[83] While this disparity might be attributable to differences in operating temperature and/or vapor residence time, a stronger implication is that cellulose does not form a furan-related intermediate during CFP.

In comparison with steam co-feeding, the carbon yield of aromatics, char+coke and oxygenates showed higher yields, while that of CO and methane is lower for the run without steam co-feeding for each catalyst with same steam exposure time. We speculate that steam is competing with pyrolytic vapors for adsorption on active sites and therefore reversibly blocking the catalytic sites.[86] Also the presence of steam might dilute the concentration of aromatics intermediates/pyrolytic vapors, and lowered aromatics conversion, and decrease aromatics and char+coke yield.[87] However, the presence of steam might enhance the steam-shifting and methanation of carbon-containing pyrolytic vapors and char+coke with more CO and CH_4 formed, especially at steam exposure times over 90 min, as the influence of steam on catalyst is diminished, and the influence of steam on cellulose pyrolysis become much more important and clear.[82]

4.3. Conclusions

Steam's effect on catalytic fast pyrolysis of cellulose was studied at 500°C using a ZSM-5 catalyst in a bubbling fluidized bed reactor. Steam affects CFP through (1) irreversible changes to the catalyst structure and (2) direct interference through changing chemistries of pyrolysis and/or catalysis.

Steam caused dealumination caused a conversion of Brønsted acidity to Lewis acidity. In the first 60 min of steam exposure, the catalyst was also found to change in pore structure as more fine mesopores formed at the cost of larger mesopores in the binder. Exposure of the catalyst to steam increased the zeolite crystal size. Furthermore, the catalyst particles size agglomerated to form larger particles with steam co-feeding.

These irreversible catalyst changes were observed to effect product yields, both with and without steam co-feeding. In both cases, steamed catalyst had a lower aromatics and char+coke yield and a higher methane and unidentified products yield.

Reversible effects of steam co-feeding were also observed. Steam co-feeding lowers yields of aromatics, char+coke, and identifiable oxygenate species, increases yields of CO and methane, and does not change the overall yields of CO_2 and olefins. The data suggest that steam co-feeding favors the production of ethylene over propylene, but more data are required to confirm this finding.

CHAPTER 5

Effects of Contact Time and Coking on the Catalytic Fast Pyrolysis of Cellulose

The contents in this chapter have been submitted as a journal article in *Green Chemistry*:

Yang, H.; Coolman, R. J.; Karanjkar, P. U.; Wang, H.; Dornath, P.; Chen, H.; Fan, W.; Conner, W. C.; Mountziaris, T. J.; Huber, G. W., The Effects of Contact Time and Coking on the Catalytic Fast Pyrolysis of Cellulose, *submitted Aug 11, 2016*.

- Yang, H. (under Huber, G. W. and Chen, H., and with support from Wang, H.) collected all the reactor data in this study, prepared most of the figures, and assisted with experimental design and data interpretation.
- My contribution to this work (under Huber, G. W. and Mountziaris, T. J.) was reactor construction (shared with Karanjkar, P.), maintenance, experimental design, planning, data interpretation, and writing this paper.
- Dornath, P. (under Fan, W.) collected the argon-adsorption data.
- Chen, H.; Mountziaris, T. J.; Fan, W.; Conner, W. C.; Huber, G. W. were the primary investigators of this study.

5.1. Background

While previous work has examined the effects of catalyst contact time (as the inverse of WHSV) on product yield, these comparisons were performed at constant time-on-stream and across the same mass of catalyst bed.[39, 49, 50, 102] Unfortunately this data is of limited value because the catalyst accumulates coke and char during the reaction and thereby decreases in activity. The main objective of this work is to compare product yields across multiple orders of magnitude of catalyst contact time whilst maintaining constant catalyst activity by controlling for loadings of char and/or coke. This data will provide insights into the mechanism of CFP, similar to how scans of catalyst contact time ($LHSV^{-1}$) for Mobil's Methanol-to-Gasoline (MTG) revealed that methanol is first converted into dimethyl ether which then is converted into olefins and aromatics (Figure 5.1).[9]

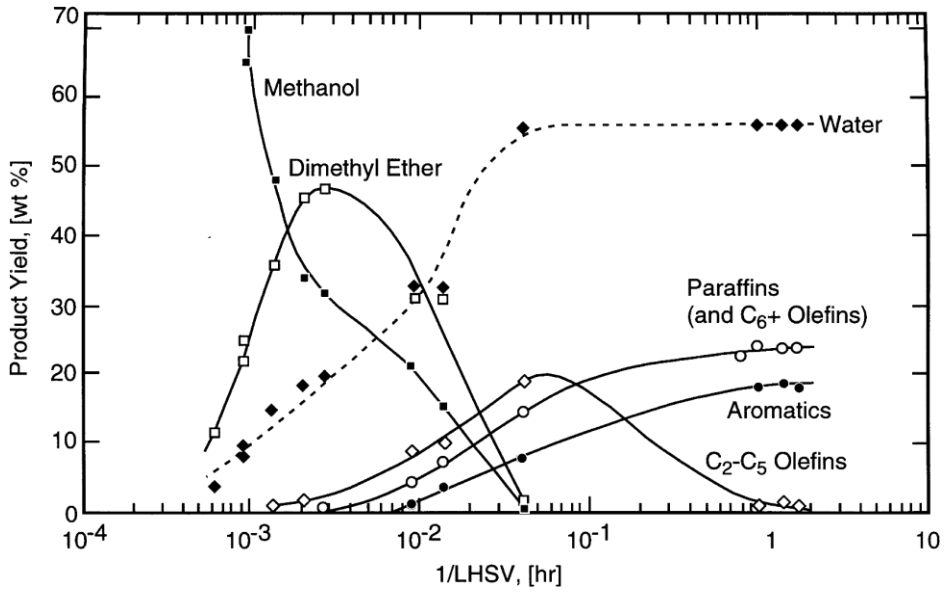

Figure 5.1. Scan of space velocity for Mobil's Methanol-to-Olefins (MTO) process spanning four orders-of-magnitude. (Reproduced from Stöcker by permission of Elsevier Science B.V., Amsterdam)

Previous work has shown that lignin forms coke under CFP conditions[103]. To isolate and study the production aromatics and olefins (and in contrast to previous studies by our group which

used pinewood sawdust[39, 49]), pure cellulose was used as a model compound for lignocellulosic biomass.

We also investigated the effects that coking has on catalyst activity. With the aim of determining what loadings of char+coke render the catalyst inactive, we examined the effects of char+coke on product yield, acidity, and micro-/meso-porosity. These quantifications additionally provide insight into how much char+coke needs to combusted off the catalyst to regenerate it.

Experiments from this chapter were done in the same apparatus described in Chapter 4. A diagram of the system is shown in Figure 5.2, differing from Figure 4.1 in that it does not contain a syringe pump or steam kettle.

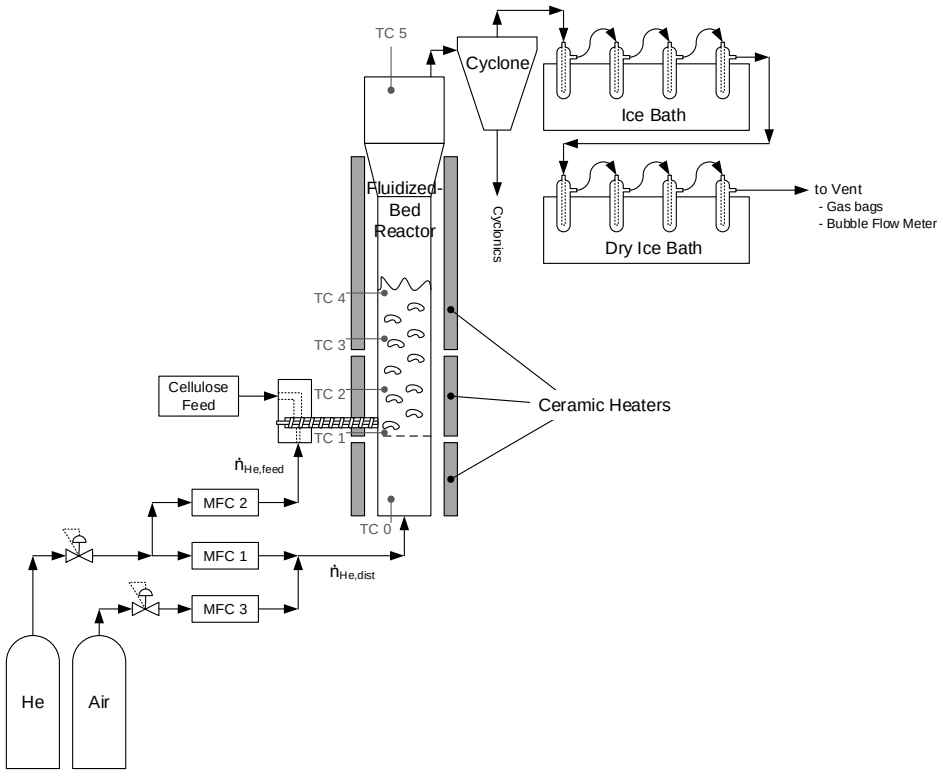

Figure 5.2. Schematic of experimental system used for catalytic fast pyrolysis.

The objective of this chapter is to understand how CFP product yields are affected by (1) varying space velocity (the inverse of catalyst contact time) while the catalyst remains active, and

(2) various degrees of catalyst coking. For each experiment 30-240 grams of fresh catalyst was loaded into the reactor, corresponding to roughly 5-40% of the total reactor volume.

Table 5.1 and Figure 5.3 show how changes in catalyst contact time (τ_{cat}) affect the other three residence times (τ_b, τ_f, τ_r). All four quantities increase together; albeit to different degrees depending on the value of τ_{cat}.

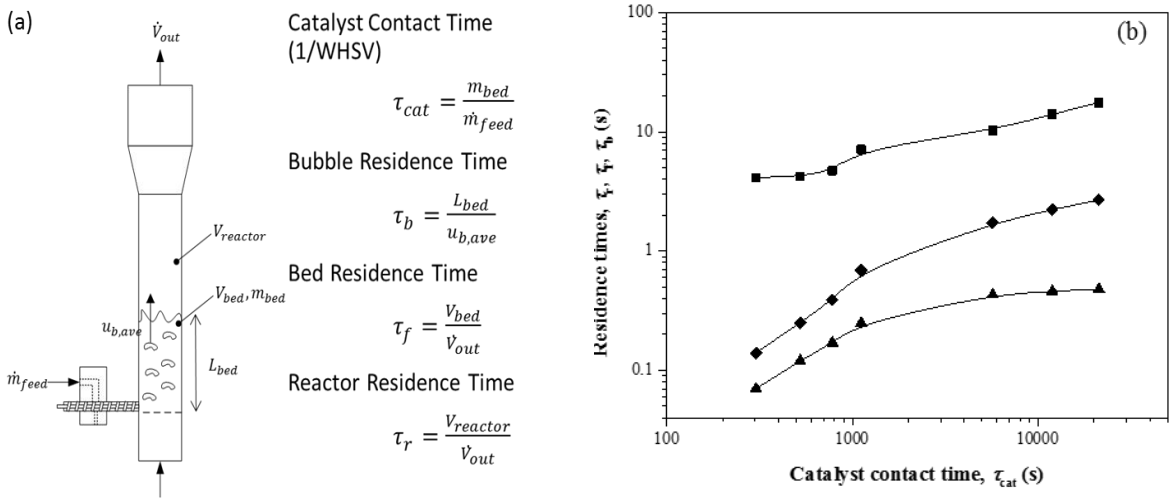

Figure 5.3. (a) Definitions of various residence times (same as Figure 1.1) (b) The effect of catalyst-contact time τ_{cat} (for all experimental values tested in this study) on other residence times. Key: ■:Reactor residence time τ_r (from bubble flow meter), ◆:Bed residence time τ_f (from Assemblage Model), ▲:Bubble residence time τ_b (from Assemblage Model).

A typical reaction was carried out over a duration of 1 to 30 min time-on-stream. The reactor and plenum were resistively heated to a target temperature of 500°C. The catalyst was fluidized using helium at a rate of 600 sccm.

The liquid product dissolved in isopropanol was analyzed for aromatics using a Shimadzu GC2010 gas chromatograph with an Agilent HP INNOWax column (60 m, 0.32 mm, 0.5 μm) and a flame ionization detector (FID). Column max temperature: 260°C. Carrier gas: He. Injection mode: split ratio of 10. Temperature Program: Initial temperature 70°C, hold time 10 min, then heat up to 95°C at 2°C·min^{-1}, then heat up to 240°C at 15°C and hold for 10 min.

The liquid products were also analyzed using a high-performance liquid chromatograph (HPLC; Shimadzu, LC-20AT) equipped with an RI (RID-10A) detector. Separation was achieved using a Biorad Aminex HPX-87H column at 303 K with 5 mM H_2SO_4 as the mobile phase flowing at a rate of 0.6 $mL \cdot min^{-1}$. For each analysis, the injection volume was 1 μL.

Non-condensable gases collected in gas bags at various times during the reaction were analyzed using a refinery gas analyzer Shimadzu GC2014 system with (1) Restek Rtx (RTX) – Alumina column and a flame-ionization (FID) detector to analyze methane and C_2–C_5 olefins and (2) RTX–MS-5A column and RTX-Q-plot column with a thermal conductivity detector (TCD) to analyze CO and CO_2, respectively.

The reactor configuration did now allow for on-stream catalyst sampling; the catalyst bed was sampled only after on-stream feeding had concluded by removing the feed auger before the reactor was set to combustion mode.

Textural characterization was performed using Ar adsorption/desorption isotherms obtained at -196°C using Quantachrome Autosorb iQ Automated Gas Sorption system. The RLRS-BET surface areas were calculated from the P/P_0 from 0.003 to 0.5. The total volume was calculated at P/P_0=0.95. The pore-size distribution was calculated using the NLDFT (non-local density functional theory) adsorption kernel in AsiQwin v3.01 (Quantachrome) for Ar adsorbed in cylindrical pores of silica at 87 K.

TPO of the spent catalysts was performed with a TA instrument Q500 system. For these experiments, approximately 20 mg of sample was loaded onto a Pt pan. The samples were first heated to 120°C with $10°C \cdot min^{-1}$ for 10 min and further heated to 700°C with $10°C \cdot min^{-1}$ ramp rate in 50 $mL \cdot min^{-1}$ O_2 flow. The weight loss because of char+coke was then obtained by taking into consideration the peaks in the range of 325–700°C.

The acidity of the catalyst samples was measured using TPD of isopropylamine (IPA-TPD) and ammonia (NH_3-TPD) using a Micromeritics® Autochem II 2920 Chemisorption Analyzer with an inline TCD. Before testing, the catalyst was heated up to 600°C for 2 hr in helium to remove adsorbed water or organic species. For IPA-TPD, once the 100-mg sample was saturated with IPA at 50°C for 20 min, helium was flushed at 50 sccm for 2 hr to remove any physisorbed isopropylamine. TCD measurements were then taken while heating the sample from 50°C to 700°C at a heating rate of $10°C \cdot min^{-1}$. For NH_3-TPD, the 100-mg sample was saturated with NH_3 at 100°C for 30 min, helium was flushed at 50 sccm for 2 hr to remove any physisorbed ammonia. TCD measurements were then taken while heating the sample from 150°C to 700°C at a heating rate of $5°C \cdot min^{-1}$. The number of Brønsted acid sites was calculated based on the TCD signal for NH_3 and propylene from IPA-TPD; the products of isopropylamine decomposition. Total acid sites were calculated based on the TCD signal for ammonia from NH_3-TPD. The number of Lewis acid sites was taken as the difference between total acid sites and Brønsted acid sites.

5.2. Results and Discussion

5.2.1. Effects of catalyst contact time on product yield, selectivity, and catalyst

Table 5.1 and Figure 5.4 report the carbon yields of products as a function of catalyst contact time (τ_{cat}) at a constant weight turnover (≤ 1). The weight turnover was approximately 1 for catalysts contact times less than ~2,000 s. At catalyst contact times greater than ~2,000 s, the time-on-stream would have been prohibitively long to reach a turnover of ~1, so these reactions were terminated after ~30 min.

The target temperature of every reaction was 500°C, though in practice bed temperatures fell within a range of 500±40°C. Temperatures listed in this study are the average temperature of catalyst bed over the duration of the reaction with a plus-or-minus range encompassing 95% of the

temperatures logged at an interval of 0.5 sec. The reasons for difficulty in maintaining constant bed temperature were that cellulose was fed at room temperature and the decomposition of cellulose is endothermic[78], hence bed temperature reduced quickly especially for low contact times. Increases in bed temperature at higher contact times may be attributed to the exothermic conversion of cellulose into coke.

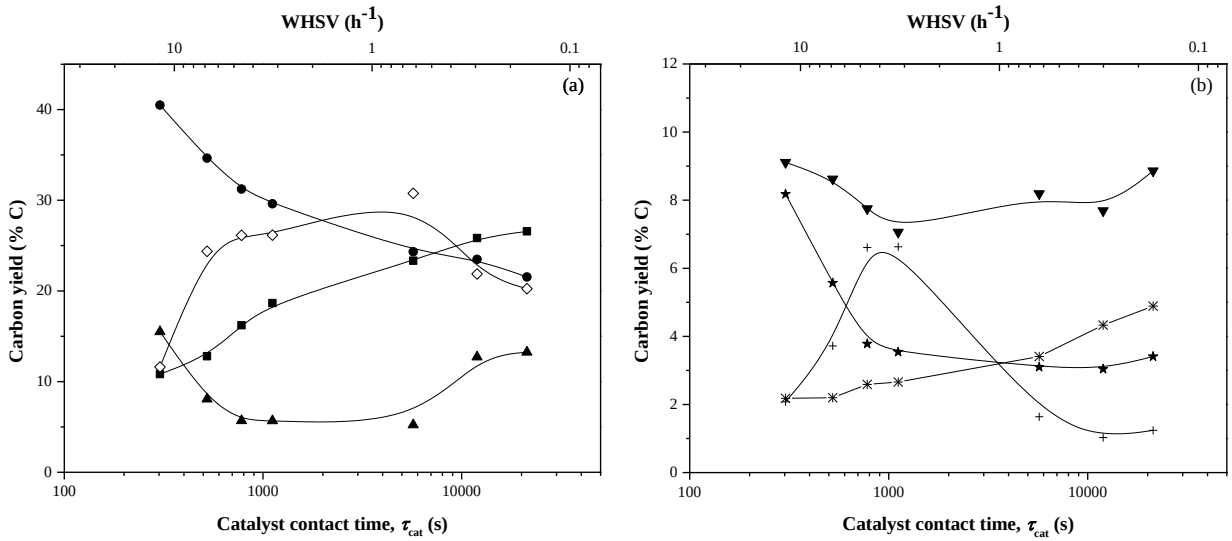

Figure 5.4. Carbon yield as function of catalyst contact time τ_{cat} ($WHSV^{-1}$) for catalytic fast pyrolysis of cellulose with fresh ZSM-5 catalyst. (Reaction conditions: Cellulose feed, Temperature: 500°C) Key: (a) ■:Aromatics ●:CO ▲:Char+Coke, ◇:Unidentified Carbon (b) ▼:Olefins+Aliphatics *:CO_2 ★:Methane +:Identified Oxygenates

Table 5.1. Carbon yield of products as function of catalyst contact time (Reaction conditions: Cellulose feed, Temperature: 500°C, 30-240 g catalyst)

Catalyst contact time τ_{cat} (s)	**303**	**523**	**780**	**1,116**	**5,702**	**11,952**	**21,312**
WHSV (hr^{-1})	**12.67**	**6.88**	**4.62**	**3.23**	**0.63**	**0.3**	**0.17**
Catalyst mass (g)	32	60	90	120	240	240	240
Time-on-stream (min)	6.5	10	15	20	31	31	30
Weight turnover	1.29	1.15	1.15	1.08	0.33	0.16	0.08
Outlet molar flow (sccm)	7,792	7,594	6,818	4,511	3,125	2,294	1,829
Temperature (°C)	512±30	529±19	520±11	519±7	526±1.5	527±2.6	529±0.6
Bubble res. time τ_b (s)	0.07	0.12	0.17	0.25	0.43	0.46	0.48
Bed res. time τ_f (s)	0.14	0.25	0.39	0.69	1.72	2.22	2.69
Reactor res. time τ_r (s)	4.13	4.24	4.72	7.13	10.29	14.02	17.59
CO	**40.5%**	**34.7%**	**31.2%**	**29.6%**	**24.3%**	**23.5%**	**21.5%**
CO_2	**2.2%**	**2.2%**	**2.6%**	**2.7%**	**3.4%**	**4.3%**	**4.9%**
Char+Coke	**15.5%**	**8.1%**	**5.7%**	**5.7%**	**5.2%**	**12.7%**	**13.2%**
Methane	**8.2%**	**5.6%**	**3.8%**	**3.5%**	**3.1%**	**3.0%**	**3.4%**
Aromatics	**10.8%**	**12.8%**	**16.2%**	**18.7%**	**23.3%**	**25.8%**	**26.6%**
Benzene	4.6%	4.9%	5.7%	6.3%	8.1%	9.6%	10.9%
Toluene	2.3%	3.8%	5.6%	6.8%	8.1%	8.6%	8.2%
Xylenes	0.5%	0.4%	1.5%	1.8%	2.1%	2.1%	1.9%
Naphthalenes	1.9%	1.6%	1.7%	2.0%	3.4%	3.8%	3.8%
Ethyl benzene	0.2%	0.7%	0.4%	0.3%	0.2%	0.3%	0.3%
Styrene	0.6%	0.6%	0.6%	0.6%	0.6%	0.5%	0.5%
Indene	0.8%	0.8%	0.8%	0.9%	1.0%	1.0%	0.9%
Olefins+Aliphatics	**9.1%**	**8.6%**	**7.8%**	**7.1%**	**8.2%**	**7.7%**	**8.9%**
C2	8.8%	7.9%	6.8%	4.7%	6.7%	7.0%	7.4%
C3	0.3%	0.3%	0.8%	1.8%	1.2%	0.6%	1.0%
C4	0.0%	0.2%	0.0%	0.2%	0.1%	0.1%	0.1%
C5	0.0%	0.3%	0.2%	0.3%	0.1%	0.1%	0.4%
Identified Oxygenates	**2.1%**	**3.7%**	**6.6%**	**6.6%**	**1.7%**	**1.0%**	**1.2%**
Benzofuran	0.2%	0.2%	0.2%	0.2%	0.1%	0.1%	0.1%
Phenol	0.5%	0.7%	0.8%	0.8%	0.4%	0.3%	0.2%
Hydroxyacetone	0.0%	0.0%	0.0%	0.0%	0.0%	0.0%	0.0%
HMF	0.3%	0.2%	0.2%	0.1%	0.2%	0.4%	0.5%
Acetaldehyde	0.5%	1.3%	2.4%	2.4%	0.4%	0.2%	0.2%
Furan	0.5%	1.1%	2.3%	2.3%	0.3%	0.1%	0.1%
2-methylfuran	0.0%	0.3%	0.7%	0.6%	0.0%	0.0%	0.0%
Acetic acid	0.0%	0.0%	0.1%	0.2%	0.2%	0.0%	0.0%
Unidentified Carbon	**11.6%**	**24.4%**	**26.1%**	**26.2%**	**30.8%**	**21.9%**	**20.3%**

The main products observed were aromatics, olefins, methane, CO, CO, char+coke, and light oxygenates. The aromatics consisted of benzene, toluene, ethylbenzene, xylenes, styrene, indene, and naphthalene. The identified oxygenates were benzofuran, phenol, acetaldehyde, acetic acid, hydroxyacetone, and 5-hydroxymethylfurfural (HMF). The HPLC analysis of the product showed no anhydrosugars in the liquid product.

Three different ranges of catalyst contact times were observed. At catalyst contact times <1,000 s, the aromatics and both unidentified and identified oxygenates showed a dramatic increase in the yield. The aromatics yield increased from 11% at catalyst contact time of 303 s to 19% at a contact time of 1,116 s whereas the yield of unidentified oxygenates increased from 12% to 26%. In contrast, the CO yield decreased from 40% to 30% as the catalyst contact time increased from 303 s to 1,116 s. Olefins and methane showed a similar trend as CO with their yields decreasing from 9% and 8% to 7% and 3% respectively. At intermediate catalyst contact times (1,000 – 10,000 s), the aromatics yield increased at a relatively lower rate. The yield of identified oxygenates decreased from 7% to 2% during this range of contact times and the yield of methane and olefins didn't change. At higher catalyst contact times (10,000 s – 22,000 s), the aromatics yield increased slowly to a maximum of 27%. The CO yield also decreased slowly reaching 22% carbon yield. The yield of unidentified oxygenates decreased from 31% to 20% as the catalyst contact time increased to 21,312 s. The char+coke yield increased from 5% to 13%.

The high yields of CO at short catalyst contact times suggest that at these conditions the biomass undergoes reactions similar to gasification. Alternatively, an oxygen-rich intermediate on the catalyst surface may be decomposing into CO, char+coke, and methane. The unidentified balance carbon goes through a maximum at intermediate catalyst contact times, suggesting that some unidentified intermediate (perhaps a furanic oligomer) forms at intermediate contact time and then converts into aromatics if it has adequate contact with the catalyst. This interpretation is consistent with our previous work on CFP of furan over a fixed bed of ZSM-5, wherein furan adsorbs in the form of oligomers which in turn form CO, olefins, and aromatics.[102]

To rule out the candidacy of compounds previously suspected to be intermediates (such as anhydrosugars, furanic compounds, and other oxygenated species)[28], we replicated the conditions

of CFP at a catalyst contact time (τ_{cat}) of 780 s (a condition demonstrated to produce a high amount of unidentified balance carbon) but replaced the catalyst bed with inactive quartz beads. The results of these experiments are compared in Table 5.2. The unidentified balance carbon for un-catalyzed fast pyrolysis (14.91%) was lower than that of the CFP (26.16%). Anhydrosugars were detected in the un-catalyzed products at a yield of 6.07% compared to the catalyzed reaction which saw no evidence of anhydrosugars. Lastly, the yield of identified oxygenates of the un-catalyzed reaction (9.01%) was higher than that for the catalyzed reaction (6.61%). This analysis rules out anhydrosugars, furanic compounds, and other identified oxygenated species as candidates for the undetectable intermediates species which are precursors to both CO (at low τ_{cat}) and aromatics (at high τ_{cat}). Detecting and identifying these intermediates is a topic for future study and will require the use of advanced analytical approaches that allow the identification of more functionalities and molecular weights as these intermediates cannot be analyzed with conventional analytical techniques like GC or HPLC.

Table 5.2. Carbon yield of products using bed of quartz beads or spray-dried ZSM-5. (Reaction conditions: Cellulose feed; Temperature: ~500°C; Bed mass: 90 g.)

Bed type	**Quartz**	**ZSM-5**
WHSV (hr^{-1})	NA	4.62
Feed rate (g/min)	6.37	6.92
Time-on-stream (min)	18	15
Temperature (°C)	465±20.8	520±11
CO	**41.1%**	**31.2%**
CO_2	**2.0%**	**2.6%**
Char+Coke	**4.7%**	**5.7%**
Methane	**8.7%**	**3.8%**
Aromatics	**0.6%**	**16.2%**
Benzene	0.1%	5.7%
Toluene	0.1%	5.6%
Xylenes	0.1%	1.5%
Napthalenes	0.1%	1.7%
Ethyl-Benzene	0.0%	0.4%
Styrene	0.1%	0.6%
Indene	0.1%	0.8%
Olefins/Aliphatics	**13.0%**	**7.8%**
Ethane	2.4%	1.0%
Ethylene	7.3%	5.2%
C3	2.4%	0.8%
C4	0.2%	0.0%
C5	0.7%	0.2%
Identified Oxygenates	**9.0%**	**6.6%**
Benzofuran	0.0%	0.2%
Phenol	0.2%	0.8%
Hydroxyacetone	1.0%	0.0%
HMF	0.1%	0.2%
Formic acid	0.1%	0.0%
Furfural	0.2%	0.0%
Acetylaldehyde	3.8%	2.4%
Furan	1.0%	2.3%
2-MF	1.8%	0.7%
Acetic acid	0.8%	0.1%
Anhydrosugars	**6.1%**	**0.0%**
Levoglucosan	1.2%	0.0%
Others	4.9%	0.0%
Unidentified Carbon	**14.9%**	**26.1%**

Figure 5.5 shows aromatic selectivity as a function of the catalyst contact time (calculated from the data in Table 5.1). Most striking is the interplay between benzene and toluene selectivity. While the yields of both aromatic compounds were found to increase with catalyst contact time,

an increase in toluene selectivity is always accompanied by a benzene decrease, and vice versa. The napthalenes follow a similar trend as the benzene. Similar behavior has been observed previously by our group.[77]

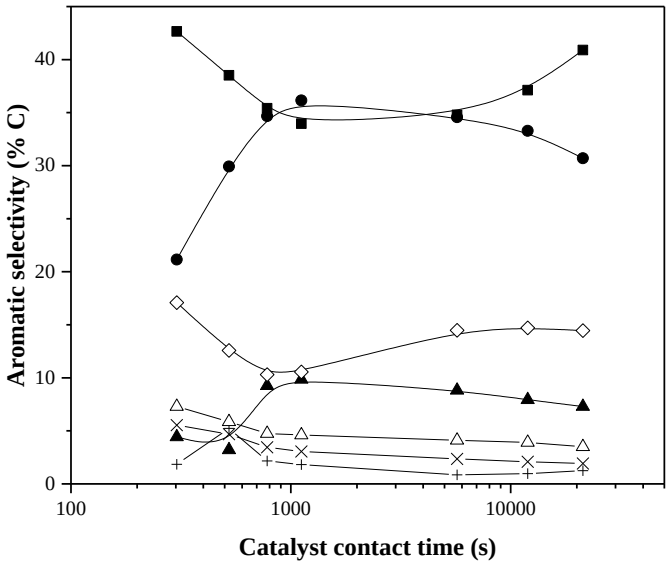

Figure 5.5. Aromatic selectivity as function of catalyst contact time τ_{cat} ($WHSV^{-1}$) for catalytic fast pyrolysis of cellulose with fresh ZSM-5 catalyst. (Reaction conditions: Cellulose feed, Temperature: 500°C.) Key: ■:Benzene ●:Toluene ▲:Xylenes ◇:Naphthalenes +:Ethylbenzene ×:Styrene △:Indene

Figure 5.6 shows the DTG (derivative weight change) of end-of-reaction catalyst TPO for selected reactions shown in in Table 5.1. At 300°C the first peak indicates combustion of un-pyrolized cellulose (verified through the TPO of raw cellulose with fresh ZSM-5, shown in **Error! Reference source not found.** found in Appendix). Between temperatures of 450°C and 600°C, we see the combustion of char+coke. For reactions with a catalyst contact time higher than 2,000 s, the runs were terminated before reaching a weight turnover of ~ 1, resulting in lower amounts of char+coke on a catalyst-mass basis. At both low and high catalyst contact times there is evidence of two morphologies of char+coke, though this data offers little suggestion as to which peaks are char and which are coke.

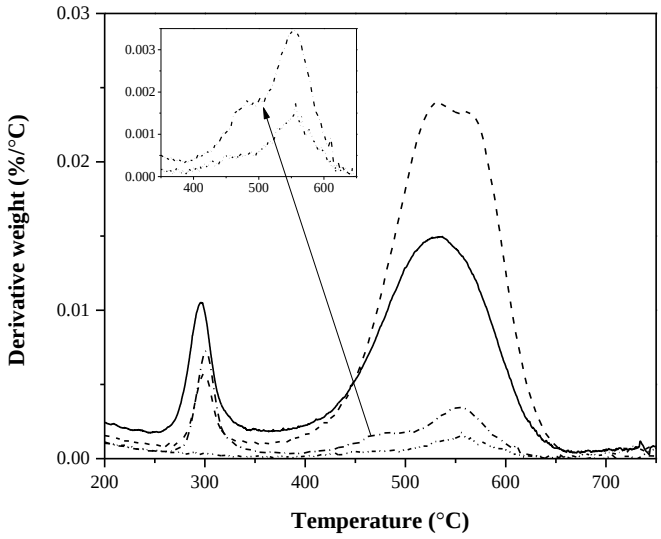

Figure 5.6. Derivative of weight change of TPO of samples with various catalyst contact times τ_{cat} ($WHSV^{-1}$) (Reaction conditions: Cellulose feed, Temperature: 500°C.) Catalyst contact time: 303 s (solid), 780 s (dash), 11952 s (dash dot), 21312 s (dash dot dot)

5.2.2. Effect of weight turnover on product yield, selectivity, and catalyst

Table 5.3 and Figure 5.7 show product yields as a function of mass turnover while WHSV was held constant at 12.27 hr^{-1}. The reaction time for these experiments varied between 1.5 min and 31 min to allow for quantification of aromatics and char+coke. It should be noted that about the catalyst-bed temperature varies within the bounds of 500°C ±40°C, the reasons for which are listed in the previous section.

Table 5.3. Carbon yield of products as function of weight turnover (Reaction conditions: Cellulose feed, WHSV: 12.27 hr^{-1}, Temperature: 500°C, Catalyst Mass: 30 g)

Weight turnover	**0.31**	**0.43**	**1.33**	**2.02**	**6.21**
Temperature (°C)	481±16	501±21	512±30	533±39	531±29
Time on stream (min)	1.50	2.20	6.50	10.00	31.00
Feed rate (g/min)	6.15	6.12	6.34	6.07	6.01
CO	**31.1%**	**37.1%**	**40.5%**	**41.0%**	**39.1%**
CO_2	**2.1%**	**2.2%**	**2.2%**	**1.8%**	**1.6%**
Char+Coke	**28.5%**	**25.8%**	**15.5%**	**10.1%**	**4.6%**
Methane	**4.9%**	**5.8%**	**8.2%**	**10.3%**	**10.4%**
Aromatics	**15.4%**	**12.5%**	**10.8%**	**8.2%**	**5.5%**
Benzene	4.9%	4.1%	4.6%	4.4%	3.1%
Toluene	4.3%	3.5%	2.3%	1.0%	0.7%
Xylenes	1.5%	1.1%	0.5%	0.2%	0.1%
Naphthalenes	2.3%	2.1%	1.9%	1.6%	0.8%
Ethyl benzene	0.7%	0.5%	0.2%	0.1%	0.0%
Styrene	0.6%	0.6%	0.6%	0.5%	0.3%
Indene	1.1%	0.7%	0.8%	0.6%	0.4%
Olefins+Aliphatics	**7.0%**	**7.1%**	**9.1%**	**9.4%**	**9.9%**
C2	6.5%	7.0%	8.8%	8.8%	9.0%
C3	0.1%	0.1%	0.3%	0.5%	0.9%
C4	0.2%	0.0%	0.0%	0.0%	0.0%
C5	0.3%	0.0%	0.0%	0.1%	0.0%
Identified Oxygenates	**7.3%**	**4.5%**	**2.1%**	**1.3%**	**1.1%**
Benzofuran	0.4%	0.4%	0.2%	0.1%	0.1%
Phenol	0.8%	0.6%	0.5%	0.2%	0.2%
Hydroxyacetone	0.2%	0.1%	0.0%	0.0%	0.0%
HMF	1.1%	0.9%	0.3%	0.2%	0.0%
Acetaldehyde	2.5%	1.1%	0.5%	0.4%	0.3%
Furan	1.8%	1.4%	0.5%	0.4%	0.5%
2-methylfuran	0.5%	0.2%	0.0%	0.0%	0.1%
Acetic acid	0.0%	0.0%	0.0%	0.0%	0.0%
Unidentified Carbon	**3.6%**	**5.0%**	**11.6%**	**17.8%**	**27.8%**

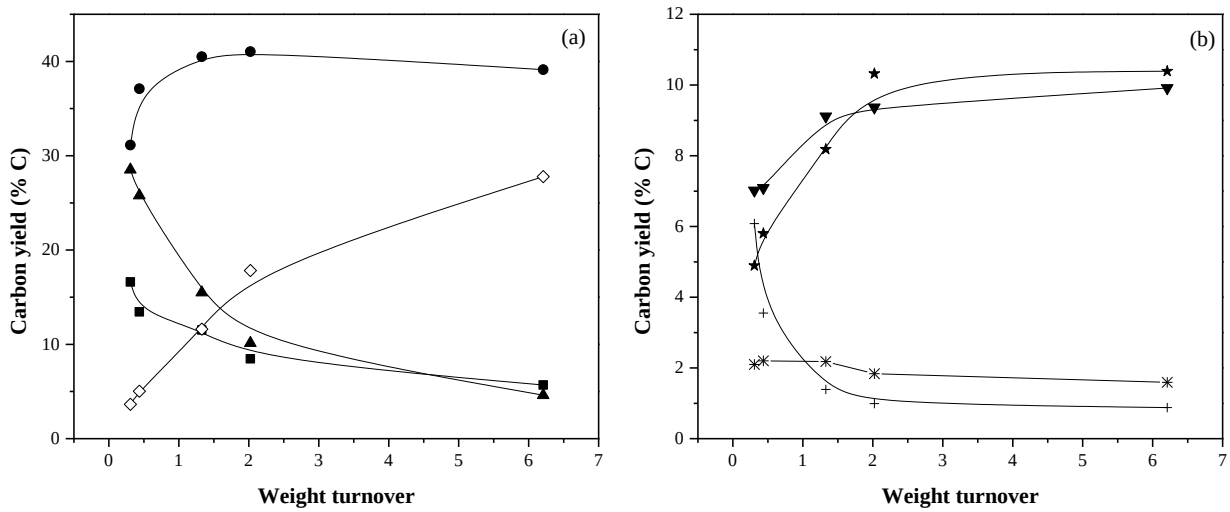

Figure 5.7. Carbon yield as function of weight turnover for catalytic fast pyrolysis of cellulose with fresh ZSM-5 catalyst. (Reaction conditions: Cellulose feed, WHSV: 12.27 hr^{-1}, Temperature: 500°C, Catalyst Mass: 30 g) Key: (a) ■:Aromatics ●:CO ▲:Char+Coke ◇: Unidentified carbon (b) ▼:Olefins *:CO_2 ★:Methane +:Identified Oxygenates

When the weight turnover increased from 0.31 to 6.21, aromatics yield decreased gradually from 15% to 6%, char+coke yield decreased from 29% to 5%. The yield of identified oxygenates also decreased from 7% to 1%. The CO yield increased initially from 31% to ~40% and then remained essentially the same at weight turnovers >1. Olefins and methane yield followed similar trend, with their yields increasing with weight turnover from 7% to 10% and from 5% to 10% respectively. With increasing weight turnover, the yield of unidentified carbon steadily increased from 4% to 28%.

The yields reported Table 5.3 and Figure 5.7 are averaged over the entire duration of the reaction, and are thus not representative of the amounts of products species produced at any given turnover. To measure how different degrees of coking affect the output product distribution at any point during a reaction, it is necessary to calculate a “differential yield”. Our choice of differential yield was evaluated using Equation 5.1, which follows the progress of product yields in real time. The results are shown in Table 5.4 and Figure 5.8.

$$\text{Differential Yield}_{i+½} = \frac{\text{Yield}_i \cdot \text{Turnover}_i - \text{Yield}_i \cdot \text{Turnover}_{i+1}}{\text{Turnover}_i - \text{Turnover}_{i+1}} \quad (5.1)$$

Table 5.4. Differential carbon yields provide estimates to the "real-time" yields of each group of product species during at each weight turnover.

Weight Turnover Interval	0.00-0.31	0.31-0.43	0.43-1.33	1.33-2.02	2.02-6.21
CO	31.1%	51.5%	42.2%	42.1%	38.2%
CO_2	2.1%	2.4%	2.2%	1.2%	1.5%
Char+Coke	28.5%	19.2%	10.5%	-0.1%	1.9%
Methane	4.9%	8.0%	9.3%	14.4%	10.4%
Aromatics	15.4%	5.4%	10.0%	3.2%	4.2%
Olefins+Aliphatics	7.0%	7.3%	10.1%	9.9%	10.2%
Identified Oxygenates	7.3%	-2.2%	0.9%	-0.4%	1.0%
Unidentified Carbon	3.6%	8.4%	14.8%	29.7%	32.6%

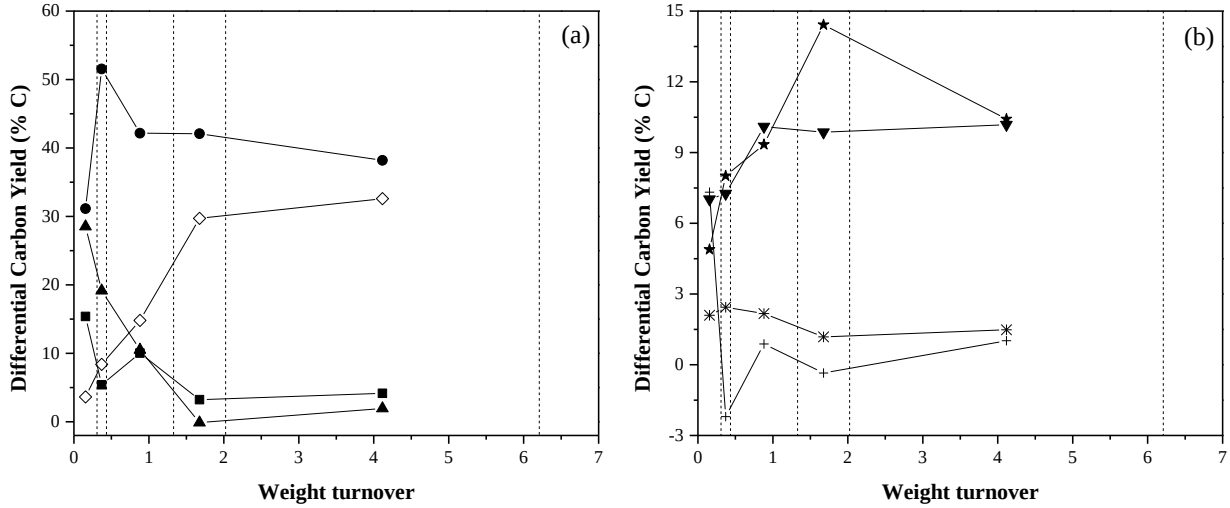

Figure 5.8. Differential carbon yields provide estimates to the "real-time" yields of each group of product species during at each weight turnover. The five vertical dotted lines indicate the turnovers from which the differential yields of each interval were calculated. (Reaction conditions: Cellulose feed, WHSV: 12.27 hr^{-1}, Temperature: 500 °C, Catalyst Mass: 30 g.) Key: (a) ■:Aromatics ●:CO ▲:Char+Coke ◇:Unidentified Carbon (b) ▼:Olefins+Aliphatics *: CO_2 ★:Methane +:Identified Oxygenates

A small number of differential yields were calculated to be less than zero, though their low magnitudes are consistent with differential yields close to zero with error bars of ±2%. As the catalyst accumulates char+coke, the production of char+coke decreases, starting at yields close to 30% with fresh catalyst, but decreases to close to 0% once the catalyst reaches a weight turnover

in the range of 1.33-2.02, and remains close to zero thereafter. Similarly, the aromatic yield decreases from 15% to 3-4% above weight turnovers of 1.33. Over the course of catalyst coking, the amount of unidentified balance carbon increased roughly in the same amount as the char+coke yield decreased. It is not known whether these undetectable compounds are the same intermediate compounds suggested by our catalyst-contact-time data; only that these compounds are not detectable with our current methods. Carbon monoxide was produced in significantly lower amounts (30%) at weight turnovers below 0.31, but reached a maximum of 50% between the turnovers of 0.31 and 0.43. Above turnovers of 0.43, the CO yield held constant around 40%. The identified oxygenates were produced at a yield of 7.32% until a turnover of 0.31 where the oxygenate yield dropped and remained at 0% (±2%). Olefin production increased from 7% to 10% over the course of the coking. Since olefins are known to be consumed in the presence of ZSM-5[9], this suggests that fewer of them are consumed as the catalyst deactivates. Methane production also increased from 5% to 10%, though this is likely due to more homogeneous chemistry occurring in the absence of active catalyst. Carbon dioxide production remained constant in the range of 1-2%.

Figure 5.9 shows aromatic selectivity as a function of weight turnover (calculated from the data in Table 5.2). As was the case in the previous section, an increase in benzene (and napthalenes) selectivity is always accompanied by a decrease toluene selectivity.

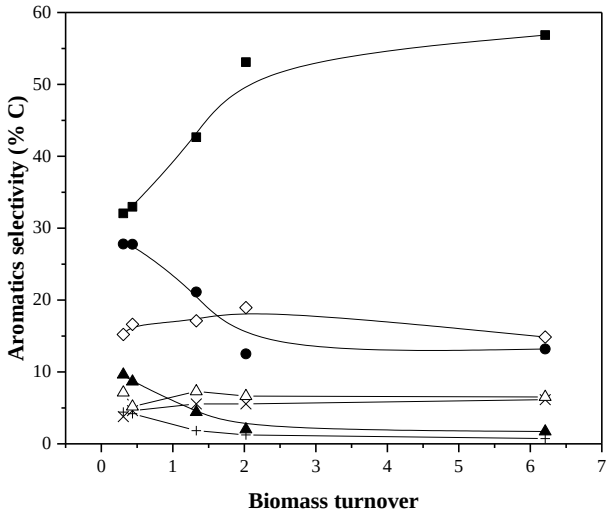

Figure 5.9. Aromatic selectivity as function of weight turnover for catalytic fast pyrolysis of cellulose with fresh ZSM-5 catalyst. (Reaction conditions: Cellulose feed, Temperature: 500°C.) Key: ■:Benzene ●:Toluene ▲:Xylenes ◇:Naphthalenes +:Ethylbenzene ×:Styrene, △:Indene

Figure 5.10 reports the TPO of used catalysts. The first peak of the derivative of weight change indicates combustion of un-reacted cellulose (verified through the TPO of raw cellulose with fresh ZSM-5, shown in **Error! Reference source not found.** found in Appendix). As before, there is evidence of two char+coke morphologies; the second of which only forms at high turnover. This finding is consistent with the literature, in particular Gamliel et al.[104] who reported the formation of a second char+coke morphology at high enough biomass-to-catalyst ratios (analogous to weight turnover), though their second morphology combusts at a lower temperature than their first.

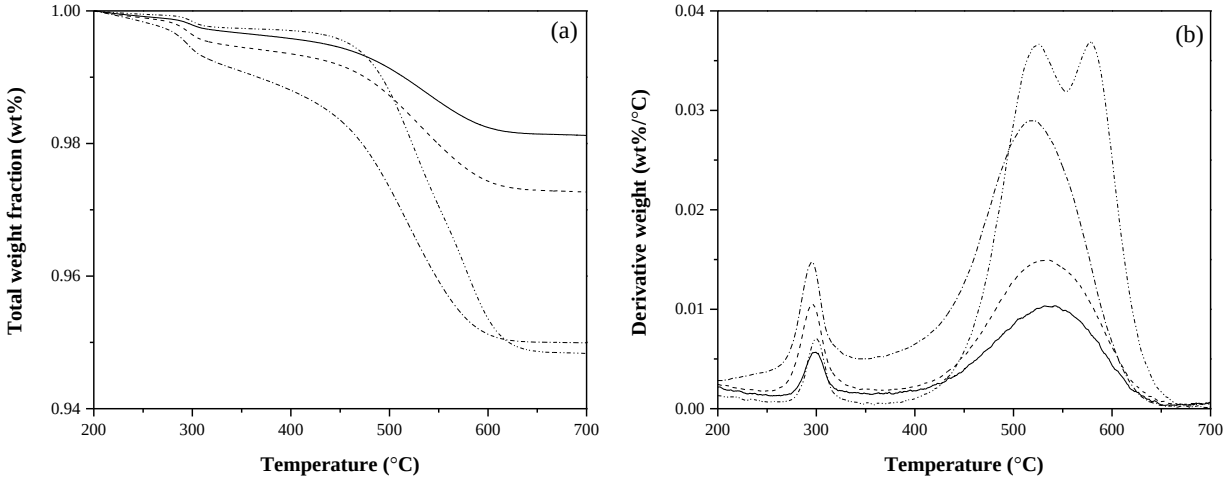

Figure 5.10. Weight change and derivative of weight change of temperature-programed oxidation of samples with various turnovers (Reaction conditions: Cellulose feed, WHSV: 12.27 hr^{-1}, Temperature: 500°C, Catalyst Mass: 30 g.) Weight turnover: 0.31 (solid), 1.33 (dash), 2.02 (dash dot), 6.21 (dash dot dot)

Table 5.5 reports the RLRS–BET surface area and pore volumes of fresh and used catalyst at different weight turnovers as described in section 4 of Hammond and Conner[105]. A more complete table and analysis is provided in the appendix as Table 6.2. Over the course of increasing weight turnover, the micropore volume decreased from around 30 $cm^3 \cdot g^{-1}$ to around 20 $cm^3 \cdot g^{-1}$. This is likely due to the blocking of micropores by the coke formed during the reaction. Up to a weight turnover of 2.02, the RLRS-BET surface area also decreased from about 30 $m^2 \cdot g^{-1}$ to about 15 $m^2 \cdot g^{-1}$, corresponding to a decrease in mesoporosity. The subsequent increase in RLRS-BET surface are may be due to deposited char+coke possessing some degree of mesoporosity.

Table 5.5. Argon RLRS–BET surface area and pore volume parameters of used catalyst. (Reaction conditions: Cellulose feed, WHSV: 12.27 hr^{-1}, Temperature: 500°C, Catalyst mass: 30 g.)

Weight Turnover	**0.00**	**0.31**	**1.31**	**2.02**	**6.21**
Micropore volume ($cm^3 \cdot g^{-1}$)	35.5	34.0	32.5	17.5	18.4
C_{BET} (dimensionless)	40.2	40.2	40.2	40.2	46.4
Monolayer volume ($cm^3 \cdot g^{-1}$)	7.5	5.2	5.1	3.6	4.9
RLRS-BET surface area ($m^2 \cdot g^{-1}$)	32.5	22.8	22.4	15.6	21.5

Figure 5.11 shows the pore-size distribution of the fresh and used catalysts. As the weight turnover increased from 0 to 6.21, there was a decrease in the number of micropores (pore size < 0.6 nm). This decrease in micropores likely has a role in decreasing the aromatics yield at higher turnovers since this porosity is needed for the formation of aromatics. Interestingly, the mesoporosity of the samples increased after a turnover of 0.31, suggesting again that the deposited char+coke may possess some degree of mesoporosity.

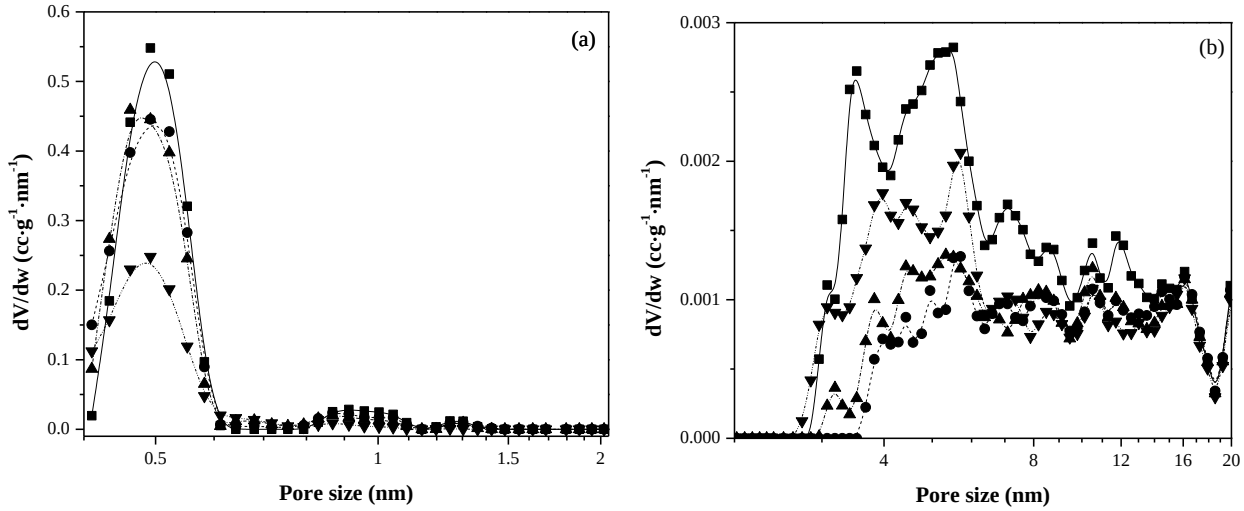

Figure 5.11. Pore size distribution obtained from argon adsorption isotherm. (Reaction conditions: Cellulose feed, WHSV: 12.27 hr^{-1}, Temperature: 500°C, Catalyst Mass: 30 g.) (a) Microporous region (b) Mesoporous region | Weight turnover: ■(solid):0.00, ●(dash):0.31, ▲(dash dot):1.33, ▼(dash dot dot):6.21

Figure 5.12 reports the Brønsted and Lewis acid-site concentrations in catalysts at different weight turnovers. Most importantly, the concentration of Brønsted acid sites decrease with increases in turnover. Since the total acidity remains roughly constant until a weight turnover of 1.33, this suggests that below this limit, increases in weight turnover convert Brønsted sites into Lewis sites. Above this turnover, the total acidity decreases suggesting that the accumulated char+coke blocks the acid sites from further interacting with any species present in the reactor. The interpretation that both microporosity and acidity are necessary for the production of aromatics is consistent with the review by Rezei et al.[106]

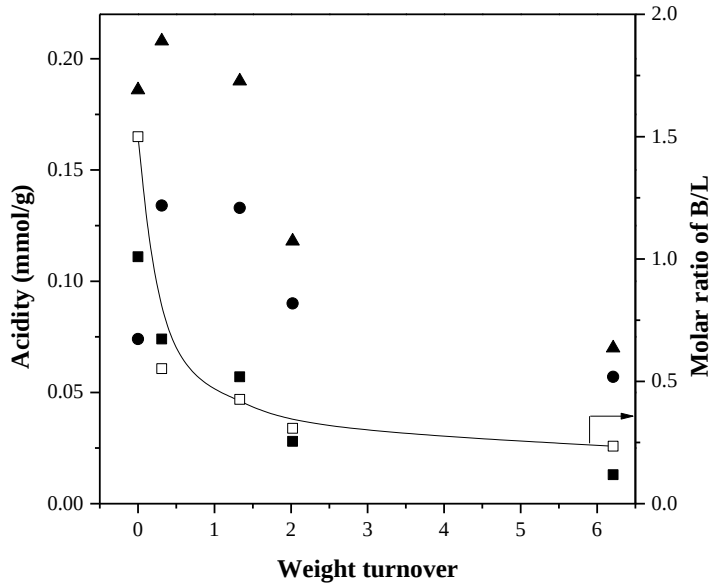

Figure 5.12. Catalyst acid-site concentration as a function of weight turnover. (Reaction conditions: Cellulose feed, WHSV: 12.27 hr^{-1}, Temperature: 500°C, Catalyst Mass: 30 g.) Key: ▲:Total acid site concentration ■:Brønsted site concentration ●:Lewis site concentration (Total minus Brønsted) □:Ratio of Brønsted sites to Lewis sites

5.3. Conclusions

Catalytic fast pyrolysis (CFP) of cellulose over ZSM-5 was studied in a bubbling fluidized-bed reactor to understand the effects of catalyst contact time ($WHSV^{-1}$) and coking.

Because accumulated coke deactivates the catalyst, the effect of catalyst contact time was studied at coke loadings for which the catalyst was still known to be active. CO and CH_4 are favored at low catalyst contact times (<1000 s), oxygenated and unidentified species at medium catalyst contact times (1000 s – 10,000 s), and aromatics and CO_2 at high catalyst contact times (>10,000 s). These findings suggest that some un-detectable intermediate (indirectly observed as missing balance carbon) is homogeneously converted into CO at low contact times (<1,000 s), and heterogeneously converted into aromatics at high contact times (>10,000 s).

Coking causes a loss of catalyst activity. The majority aromatic-producing activity was lost after site turnovers of 95 (cellulose monomers to Brønsted sites) corresponding to a weight

turnover of 2.0 (feed weight to catalyst weight). At this turnover, the aromatics yield (averaged over the length of the time on stream) is halved from 15 to 8%. At this point, the catalyst has also lost more than half of its Brønsted acidity and a little more than half of its microporosity.

CHAPTER 6

Final Remarks, Recommendations, and Suggestions for Future Work

CFP is a promising technique to convert biomass into petrochemical feedstocks including benzene, toluene, and xylene. Because of the catalyst deactivation due to accumulation of char and coke, a fluidized-bed reactor configuration with continuous regeneration of catalyst is ideal for CFP of biomass. Longer catalyst contact times are necessary for production of aromatics which can be accessed by operating CFP fluidized-bed reactors in the bubbling regime.

High-cellulose feeds are recommended for CFP production of aromatics. For pure cellulose, it is recommended that catalyst be regenerated once it reaches a weight turnover of approximately 2. This deactivation was shown to be the result of coke occupying Brønsted acid sites, and entering the catalyst micropores. Future work should explore what weight turnovers will be best for each feedstock. For estimating optimal catalyst-to-biomass feed ratio, we recommend starting with inverse of the weight turnover at which the catalyst becomes deactivated.

CFP of both sawdust and crystalline cellulose was demonstrated to corrode 316 stainless steel. Because of this, it is necessary to passivate the interior of a CFP reactor with ceramic coating; a process common in high-performance engines. Such coatings were demonstrated to work well within the lab setting.

The first step of heterogeneous conversion of cellulose into CO/water precursors is estimated to be faster than the homogeneous production of pyrolysis vapors (such as anhydrosugars). This suggests a benefit to heating biomass in the presence of catalyst instead of catalytic conversion of pyrolysis fumes. To ensure rapid heating, it is necessary to grind biomass to diameters on the order of 1 mm. Augers plumbed with rotary fittings and controlled gas flows

are recommended for feeding biomass into the fluidized bed. Because steam lowers the yield of aromatics, it is recommended that the biomass be dried after grinding.

While exposing the catalyst to steam does lower its aromatic-producing activity, the decrease in aromatic production levels off after steam exposure times less than 2 hours. Because this time span is so much shorter than the lifespan of the catalyst, it is estimated that the factors limiting the lifespan of the catalyst will be attrition (intrinsic bubbling fluidized beds) and contamination of the catalyst with wood ash.

Though several lumped kinetic models exist for cellulose fast pyrolysis (without catalyst),[28, 31, 107, 108] no publications have reported the kinetic parameters for the catalytic reactions involved in cellulose CFP. Cheng et al. suggested possible reactions for CFP of furan based on qualitative data[102] but kinetic parameters for reactions involved in furan CFP were not reported. Calculation of these parameters is mainly hindered because of the analysis of reaction intermediates in cellulose CFP. For example, Chapters 2 and 3 report unidentified carbon yields of 20-35 % carbon. This thesis demonstrates that these unidentified intermediate compounds cannot be anyhydrosugars or mono-cyclic furans. We believe them to be high-molecular-weight oxygenates which may further break down into smaller molecules. These compounds are harder to identify using conventional GC and GCMS approaches.

Recently, Tessarolo and co-workers used advanced mass spectrometric techniques such as Fourier Transform Ion Cyclotron Resonance Mass Spectrometry (FT-ICR-MS) and two-dimensional gas chromatography with time-of-flight MS to characterize bio-oils obtained from flash pyrolysis of biomass.[109] Oyama and co-workers used FT-ICR-MS to characterize upgraded bio-oils.[110] These techniques may be of use in identifying the intermediates in cellulose CFP.

APPENDIX

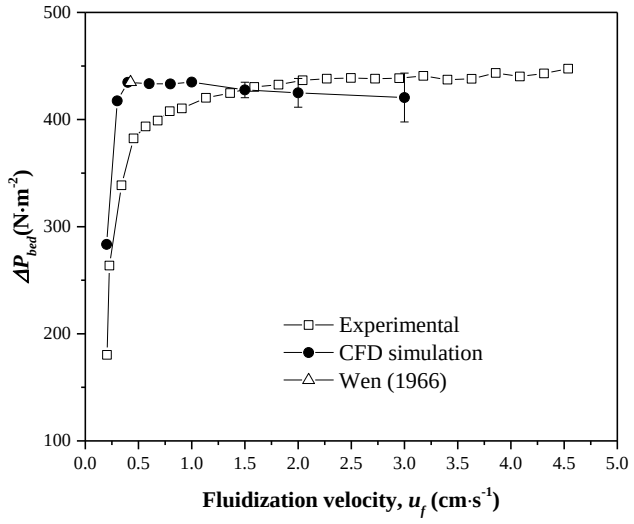

Figure 6.1. Pressure drop across the catalyst bed vs. fluidization velocity at 500°C results show two standard deviations in time above and below the mean inlet pressure. Error bars are for the CFD simulation and are not part of this thesis.

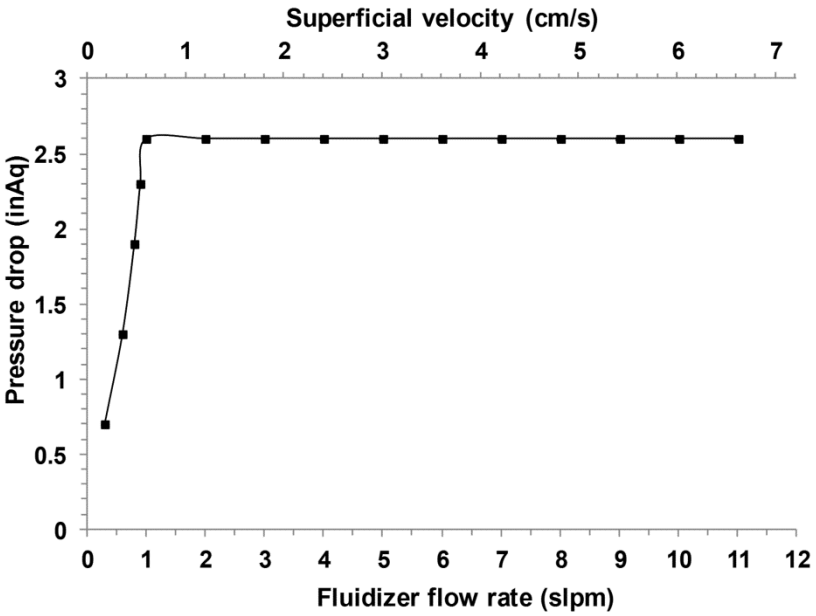

Figure 6.2. Pressure drop across the catalyst bed (in inches aqueous) at temperature 600°C with 550 g of ZSM-5 catalyst in the bed. A nitrogen flow rate of 0.8 slpm was identified as the minimum fluidization flow rate.

Table 6.1. Summary of studies conducted in fluidized beds with ZSM-5 that report aromatic yields.

Study	Feed Type	Fluidization type	Fluidizer type.	Temperature (°C)	Reactor Diameter (cm)	Fluidized Bed Weight (g)	τ_{cat} (s)	WHSV (h^{-1})	Feed Rate (g/hr)	Fluidizer flow. (slpm)
Chapter 5	Cellulose	Bubbling	Helium	500	4.92	30 - 240	300 - 21,000	0.17 - 12.67	41 - 405	1.00
Chapter 2	Cellulose	Bubbling	Helium	500	4.92	30 - 250	15,000 - 72,000	0.24 - 0.50	22 - 60	0.48 - 1.28
Dayton (2015)	Pine	Riser	Nitrogen	500 - 600	5.00	110,000 - 140,000	9,000	0.40	45,000	187
Chapter 3	Pine	Bubbling	Nitrogen	600	9.72	500	12,000	0.30	165 - 345	3.2
Chapter 3	Pine	Bubbling	Recycle	600	9.72	500	12,000	0.30	165 - 345	3.2
Paasikallio (2014)[2]	Pine	Circulating	Recycle	520	Not specified	94,000	16,920	0.21	20,000	Not specified
Mullen (2013)[3]	Switchgrass	Turbulent	Nitrogen	450 - 500	7.6	615	1,476	2.44	1,500	75
Paasikallio (2013)[4]	Forest Thinnings	Bubbling	Nitrogen	400 - 550	5.00	100	7,200	0.5	200	3.5
Lappas (2002)[5]	Biomass	Riser	Nitrogen	400	0.7	400	4,364	0.83	330	30

Study	gas (wt%)	solid (%wt)	total liquid (%wt)	aq. liquid (%wt)	org. liquid (%wt)	max. aromatics (%wt)
Chapter 5	46%	7%	-	-	16%	15%
Chapter 2	41%	6%	-	-	22%	22%
Dayton (2015)[6]	7%	50%	28%	18%	10%	2%
Chapter 3	30%	21%	36%	18%	18%	9%
Chapter 3	30%	24%	44%	14%	30%	11%
Paasikallio (2014)[2]	21%	27%	51%	19%	32%	2%
Mullen (2013)[3]	26%	21%	51%	22%	29%	3%
Paasikallio (2013)[4]	48%	18%	35%	21%	14%	1%
Lappas (2002)[5]	14%	22%	67%	30%	37%	3%

Table 6.2. BET and RLRS-BET results for spray-dried ZSM-5 at different weight turnovers. In RLRS-BET analysis, micropore volumes were selected and subtracted off to achieve C_{BET} values close to 40 and 200. This analysis sets plausible bounds for micropore volume.

Traditional BET

Weight Turnover	**0.00**	**0.31**	**1.31**	**2.02**	**6.21**
C_{BET} (dimensionless)	-132.2	-136.3	-155.3	-152.1	-135.4
Monolayer volume ($cm^3 \cdot g^{-1}$)	29.0	26.1	25.5	14.4	16.0
BET surface area ($m^2 \cdot g^{-1}$)	126.4	113.9	111.0	62.9	69.8

RLRS-BET

	Weight Turnover	**0.00**	**0.31**	**1.31**	**2.02**	**6.21**
Upper bound of micropore	Micropore volume ($cm^3 \cdot g^{-1}$)	35.5	34.0	32.5	17.5	18.4
	C_{BET} (dimensionless)	40.2	40.2	40.2	40.2	46.4
	Monolayer volume ($cm^3 \cdot g^{-1}$)	7.5	5.2	5.1	3.6	4.9
	RLRS-BET surface area ($m^2 \cdot g^{-1}$)	32.5	22.8	22.4	15.6	21.5
Lower bound of micropore	Micropore volume ($cm^3 \cdot g^{-1}$)	28.1	29.8	28.1	15.2	17.1
	C_{BET} (dimensionless)	198.9	109.5	196.6	193.6	198.7
	Monolayer volume ($cm^3 \cdot g^{-1}$)	12.3	8.0	8.0	5.0	5.5
	RLRS-BET surface area ($m^2 \cdot g^{-1}$)	53.6	35.0	34.8	21.9	24.0

Speculation Concerning Intermediate Species

Figure 5.4 (reproduced below) shows CFP product yields as a function of space velocity. The goal of this analysis was to elucidate the reaction steps of CFP, analogous to how Figure 5.1 demonstrates that in MTG, methanol becomes dimethyl ether, which becomes olefins, which become paraffins and aromatics.

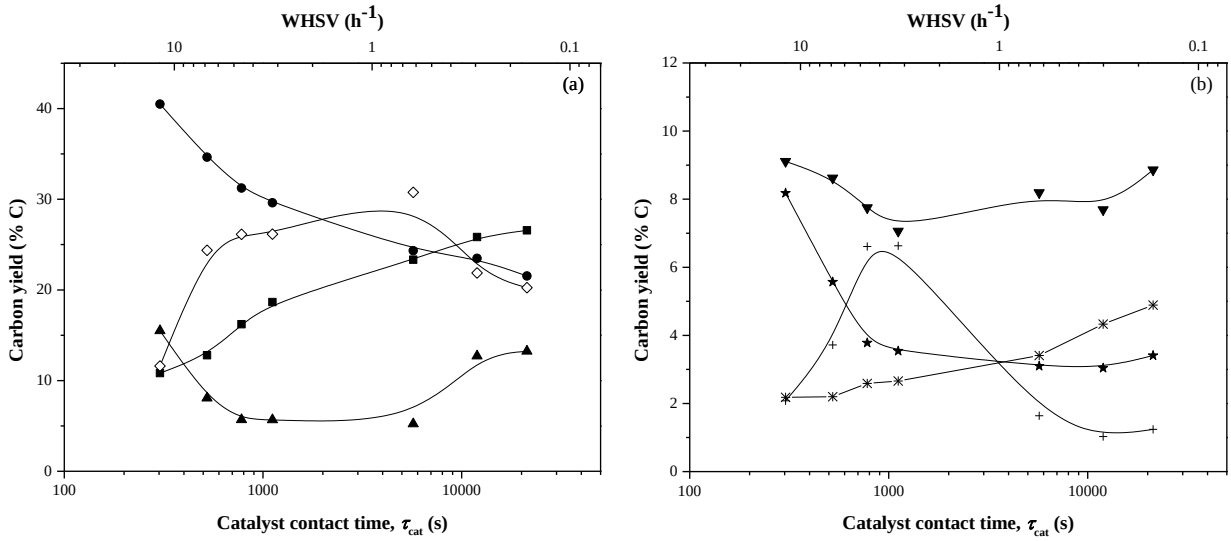

Figure 5.4. Carbon yield as function of catalyst contact time τ_{cat} ($WHSV^{-1}$) for catalytic fast pyrolysis of cellulose with fresh ZSM-5 catalyst. (Reaction conditions: Cellulose feed, Temperature: 500°C) Key: (a) ■:Aromatics ●:CO ▲:Char+Coke, ◇:Unidentified Carbon (b) ▼:Olefins+Aliphatics *:CO_2 ★:Methane +:Identified Oxygenates

While a few of the identifiable oxygenated species were produced at catalyst contact times between 500 s and 800 s, above catalyst contact times of 1000 s, the intermediate species escaped detection via GC and HPLC. This suggests that these intermediates are too large and/or functionalized to be detected via these methods. While exploration using techniques such as FT-ICR-MS is expected to be a topic of future research, until such results become available, we offer our predictions of what such investigations will find.

While large amounts of CO were shown to form at low catalyst contact times, it's not possible for CO to form carbon-carbon bonds on the surface of ZSM-5. This suggests that at low catalyst contact times, CO is merely a decomposition product of a species that is not stable upon desorption from the catalyst surface. We speculate the source of this CO is ether linkages formed between cellulose rings and cellulose chains. This contrasts with previous predictions from our group which suggested the ether linkages form *within* cellulose rings to form anhydrosugars[13].

The first step of carbon-carbon bonds in MTG is not known, but immediately following this step is the elimination of water to form olefins. Similarly, in CFP we suspect water eliminates from ether linkages to form carbon-carbon double bonds. Pure ethanol forms diethyl ether on the surface of ZSM-5 before forming ethylene[111-113] without moving onto aromatics. Conjugated bonds may play a role in aromatization.

There is no guarantee that the intermediate species formed between 500 s and 20,000 s are stable. Moreover, we suspect the species to be a mixture of compounds at various stages of pyrolysis (cellulose-bond cleavage), etherization, and conjugation. This wide variety of species sizes and functionalization accounts for the undetectability via GC and HPLC.

REFERENCES

1. E. Sjöström, *Wood chemistry : fundamentals and applications*, Academic Press, San Diego, 1993.
2. V. Paasikallio, C. Lindfors, E. Kuoppala, Y. Solantausta, A. Oasmaa, J. Lehto and J. Lehtonen, *Green Chemistry*, 2014, **16**, 3549-3559.
3. C. A. Mullen and A. A. Boateng, *Industrial & Engineering Chemistry Research*, 2013, **52**, 17156-17161.
4. V. Paasikallio, F. Agblevor, A. Oasmaa, J. Lehto and J. Lehtonen, *Energy & Fuels*, 2013, **27**, 7587-7601.
5. A. A. Lappas, M. C. Samolada, D. K. Iatridis, S. S. Voutetakis and I. A. Vasalos, *Fuel*, 2002, **81**, 2087-2095.
6. D. C. Dayton, J. R. Carpenter, A. Kataria, J. E. Peters, D. Barbee, O. D. Mante and R. Gupta, *Green Chemistry*, 2015, **17**, 4680-4689.
7. IEA., *World Energy Outlook 2014*, 2014.
8. R. D. Perlack and B. J. Stokes, *U.S. Billion-Ton Update: Biomass Supply for a Bioenergy and Bioproducts Industry*, Oak Ridge National Laboratory, Oak Ridge, TN., 2011.
9. M. Stöcker, *Microporous and Mesoporous Materials*, 1999, **29**, 3-48.
10. L. R. Lynd, C. E. Wyman and T. U. Gerngross, *Biotechnology Progress*, 1999, **15**, 777-793.
11. N. R. Singh, W. N. Delgass, F. H. Ribeiro and R. Agrawal, *Environ. Sci. Technol.*, 2010, **44**, 5298-5305.
12. T. R. Carlson, Y. T. Cheng, J. Jae and G. W. Huber, *Energy & Environmental Science*, 2011, **4**, 145-161.
13. T. R. Carlson, G. A. Tompsett, W. C. Conner and G. W. Huber, *Top. Catal.*, 2009, **52**, 241-252.
14. T. R. Carlson, T. P. Vispute and G. W. Huber, *ChemSusChem*, 2008 **1**, 397-400.
15. H. Y. Zhang, T. R. Carlson, R. Xiao and G. W. Huber, *Green Chem.*, 2012, **14**, 98-110.
16. W. L. Fanchiang and Y. C. Lin, *Appl. Catal., A*, 2012, **419**, 102-110.
17. G. T. Neumann and J. C. Hicks, *ACS Catal.*, 2012, **2**, 642-646.
18. Z. Q. Ma, E. Troussard and J. A. van Bokhoven, *Appl. Catal., A*, 2012, **423**, 130-136.
19. C. A. Mullen, A. A. Boateng, D. J. Mihalcik and N. M. Goldberg, *Energy Fuels*, 2011, **25**, 5444-5451.
20. H. Y. Zhang, R. Xiao, D. H. Wang, Z. P. Zhong, M. Song, Q. W. Pan and G. Y. He, *Energy & Fuels*, 2009, **23**, 6199-6206.
21. X. Y. Li, L. Su, Y. J. Wang, Y. Q. Yu, C. W. Wang, X. L. Li and Z. H. Wang, *Front. Env. Sci. Eng.*, 2012, **6**, 295-303.
22. A. Pattiya, J. O. Titiloye and A. V. Bridgwater, *Fuel*, 2010, **89**, 244-253.
23. R. French and S. Czernik, *Fuel Process. Technol.*, 2010, **91**, 25-32.
24. K. G. Wang and R. C. Brown, *Green Chemistry*, 2013, **15**, 675-681.
25. D. L. Compton, M. A. Jackson, D. J. Mihalcik, C. A. Mullen and A. A. Boateng, *J. Anal. Appl. Pyrolysis*, 2011, **90**, 174-181.
26. K. H. Park, H. J. Park, J. Kim, R. Ryoo, J. K. Jeon, J. Park and Y. K. Park, *J. Nanosci. Nanotechnol.*, 2010, **10**, 355-359.

27. M. J. Jeon, J. K. Jeon, D. J. Suh, S. H. Park, Y. J. Sa, S. H. Joo and Y. K. Park, *Catal. Today*, 2013, **204**, 170-178.
28. Y.-C. Lin, J. Cho, G. A. Tompsett, P. R. Westmoreland and G. W. Huber, *The Journal of Physical Chemistry C*, 2009, **113**, 20097-20107.
29. P. J. Dauenhauer, J. L. Colby, C. M. Balonek, W. J. Suszynski and L. D. Schmidt, *Green Chemistry*, 2009, **11**, 1555-1561.
30. M. S. Mettler, D. G. Vlachos and P. J. Dauenhauer, *Energy & Environmental Science*, 2012, **5**, 7797-7809.
31. J. Cho, J. M. Davis and G. W. Huber, *ChemSusChem*, 2010, **3**, 1162-1165.
32. A. J. Foster, J. Jae, Y. T. Cheng, G. W. Huber and R. F. Lobo, *Applied Catalysis a-General*, 2012, **423**, 154-161.
33. J. Jae, G. A. Tompsett, A. J. Foster, K. D. Hammond, S. M. Auerbach, R. F. Lobo and G. W. Huber, *J. Catal.*, 2011, **279**, 257-268.
34. J. D. Adjaye and N. N. Bakhshi, *Fuel Processing Technology*, 1995, **45**, 185-202.
35. J. D. Adjaye and N. N. Bakhshi, *Fuel Processing Technology*, 1995, **45**, 161-183.
36. A. V. Bridgwater and M. L. Cottam, *Energy Fuels*, 1992, **6**, 113-120.
37. A. Aho, N. Kumar, K. Eraenen, T. Salmi, M. Hupa and D. Y. Murzin, *Fuel*, 2008, **87**, 2493-2501.
38. A. Aho, N. Kumar, K. Eranen, T. Salmi, M. Hupa and D. Y. Murzin, *Process Safety and Environmental Protection*, 2007, **85**, 473-480.
39. J. Jae, R. Coolman, T. J. Mountziaris and G. W. Huber, *Chem. Eng. Sci.*, 2014, **108**, 33-46.
40. A. Aho, N. Kumar, K. Eranen, T. Salmi, M. Hupa and D. Y. Murzin, *Fuel*, 2008, **87**, 2493-2501.
41. H. Y. Zhang, R. Xiao, H. Huang and G. Xiao, *Bioresour. Technol.*, 2009, **100**, 1428-1434.
42. A. Aho, A. Tokarev, P. Backman, N. Kumar, K. Eranen, M. Hupa, B. Holmbom, T. Salmi and D. Y. Murzin, *Top. Catal.*, 2011, **54**, 941-948.
43. F. A. Agblevor, S. Beis, O. Mante and N. Abdoulmoumine, *Industrial & Engineering Chemistry Research*, 2010, **49**, 3533-3538.
44. M. Olazar, R. Aguado, J. Bilbao and A. Barona, *AIChE J.*, 2000, **46**, 1025-1033.
45. A. Atutxa, R. Aguado, A. G. Gayubo, M. Olazar and J. Bilbao, *Energy Fuels*, 2005, **19**, 765-774.
46. D. o. Kunii and O. Levenspiel, *Fluidization engineering*, Butterworth-Heinemann, Boston, 1991.
47. J. Werther, in *Ullmann's Encyclopedia of Industrial Chemistry*, Wiley-VCH Verlag GmbH & Co. KGaA, Berlin, 2000.
48. O. Levenspiel, John Wiley & Sons, New York, 1999.
49. T. R. Carlson, Y.-T. Cheng, J. Jae and G. W. Huber, *Energy & Environmental Science*, 2011, **4**, 145-161.
50. H. Zhang, T. R. Carlson, R. Xiao and G. W. Huber, *Green Chemistry*, 2012, **14**, 98-110.
51. Y.-T. Cheng and G. W. Huber, *Green Chemistry*, 2012, **14**, 3114-3125.
52. S. Du, J. A. Valla and G. M. Bollas, *Green Chemistry*, 2013, **15**, 3214-3229.
53. J. Jae, G. A. Tompsett, Y.-C. Lin, T. R. Carlson, J. Shen, T. Zhang, B. Yang, C. E. Wyman, W. C. Conner and G. W. Huber, *Energy & Environmental Science*, 2010, **3**, 358-365.
54. K. Wang, K. H. Kim and R. C. Brown, *Green Chemistry*, 2013.

55. O. Levenspiel, *The chemical reactor omnibook*, Distributed by OSU Book Stores, Corvallis, OR, 1979.
56. J. F. Davidson, D. Harrison and J. Carvalho, *Annu. Rev. Fluid Mech.*, 1977, **9**, 55-86.
57. C. Y. Wen and Y. H. Yu, *AlChE J.*, 1966, **12**, 610-&.
58. O. Levenspiel, *Engineering flow and heat exchange*, Plenum Press, New York, 1984.
59. K. Miwa, I. Muchi, S. Mori and T. Kato, *International Chemical Engineering*, 1972, **12**, 187-194.
60. S. Mori and C. Y. Wen, *AlChE J.*, 1975, **21**, 109-115.
61. J. F. Davidson and D. Harrison, *Fluidised Particles*, University Press, 1963.
62. G. B. Wallis, *One-dimensional two-phase flow*, McGraw-Hill, 1969.
63. J. Werther, E. Foundation and K. K. Kyōkai, *Fluidization IV: Fourth International Conference on Fluidization, May 29 to June 3, 1983, Shima-Kanko Hotel, Kashikojima, Japan*, Society of Chemical Engineers, Japan, 1983.
64. P. U. Karanjkar, R. J. Coolman, G. W. Huber, M. T. Blatnik, S. Almalkie, S. M. de Bruyn Kops, T. J. Mountziaris and W. C. Conner, *AlChE J.*, 2014, **60**, 1320-1335.
65. S. Whitaker, *AIChE Journal*, 1972, **18**, 361-371.
66. H. T. Bi and J. R. Grace, *Can. J. Chem. Eng.*, 1996, **74**, 1025-1027.
67. R. R. Pattipati and C. Y. Wen, *Industrial & Engineering Chemistry Process Design and Development*, 1981, **20**, 705-707.
68. A. R. Abrahamsen and D. Geldart, *Powder Technology*, 1980, **26**, 35-46.
69. A. A. Lappas, S. Bezergianni and I. A. Vasalos, *Catal. Today*, 2009, **145**, 55-62.
70. H. Y. Zhang, J. Zheng, R. Xiao, D. K. Shen, B. S. Jin, G. M. Xiao and R. Chen, *RSC Adv.*, 2013, **3**, 5769-5774.
71. H. Zhang, R. Xiao, B. Jin, D. Shen, R. Chen and G. Xiao, *Bioresour. Technol.*, 2013, **137**, 82-87.
72. O. Levenspiel, *Chemical Reaction Engineering*, Wiley, 1998.
73. T. R. Carlson, J. Jae and G. W. Huber, *Chemcatchem*, 2009, **1**, 107-110.
74. R. Xiao, B. S. Jin, H. C. Zhou, Z. P. Zhong and M. Y. Zhang, *Energy Convers. Manage.*, 2007, **48**, 778-786.
75. Y. T. Cheng, J. Jae, J. Shi, W. Fan and G. W. Huber, *Angewandte Chemie-International Edition*, 2012, **51**, 1387-1390.
76. S. Du, J. A. Valla and G. M. Bollas, *Green Chem.*, 2013, **15**, 3214.
77. H. Yang, R. J. Coolman, P. Karanjkar, H. Wang, Z. Xu, H. Chen, T. J. Mountziaris and G. W. Huber, *Green Chemistry*, 2015, **17**, 2912-2923.
78. H. P. Yang, R. Yan, H. P. Chen, D. H. Lee and C. G. Zheng, *Fuel*, 2007, **86**, 1781-1788.
79. S. L. Du, H. P. Yang, K. Z. Qian, X. H. Wang and H. P. Chen, *Fuel*, 2014, **117**, 1281-1287.
80. Q. Zhang, J. Chang, T. J. Wang and Y. Xu, *Energ Convers Manage*, 2007, **48**, 87-92.
81. E. Kantarelis, W. H. Yang and W. Blasiak, *Energy & Fuels*, 2013, **27**, 4748-4759.
82. P. T. Williams, N. Nugranad and P. A. Horne, *Biomass Gasification and Pyrolysis: State of the Art and Future Prospects*, 1997, 422-430.
83. C. Gilbert, J. Espindola, W. Conner, J. O. Trierweiler and G. W. Huber, *ChemCatChem*, 20114, **6**, 2497-2500.
84. E. F. Iliopoulou, E. V. Antonakou, S. A. Karakoulia, I. A. Vasalos, A. A. Lappas and K. S. Triantafyllidis, *Chem. Eng. J.*, 2007, **134**, 51-57.
85. L. H. Ong, M. Domok, R. Olindo, A. C. van Veen and J. A. Lercher, *Microporous Mesoporous Mater.*, 2012, **164**, 9-20.

86. A. Corma, J. Mengual and P. J. Miguel, *Appl Catal a-Gen*, 2012, **417**, 220-235.
87. A. Corma, O. Marie and F. J. Ortega, *J Catal*, 2004, **222**, 338-347.
88. A. Corma, J. Mengual and P. J. Miguel, *Applied Catalysis a-General*, 2012, **421**, 121-134.
89. Y. J. Lee, J. M. Kim, J. W. Bae, C. H. Shin and K. W. Jun, *Fuel*, 2009, **88**, 1915-1921.
90. D. S. Shihabi, W. E. Garwood, P. Chu, J. N. Miale, R. M. Lago, C. T. W. Chu and C. D. Chang, *J Catal*, 1985, **93**, 471-474.
91. J. M. Fougerit, N. S. Gnep, M. Guisnet, P. Amigues, J. L. Duplan and F. Hugues, *Zeolites and Related Microporous Materials: State of the Art 1994*, 1994, **84**, 1723-1730.
92. E. Kantarelis, W. Yang and W. Blasiak, *Fuel*, 2014, **122**, 119-125.
93. T. Blasco, A. Corma and J. Martinez-Triguero, *J Catal*, 2006, **237**, 267-277.
94. C. Baerlocher, W. M. Meier and D. Olson, *Atlas of zeolite framework types*, Elsevier, Amsterdam ; New York, 2007.
95. S. H. Jhung, J. S. Chang, J. S. Hwang and S. E. Park, *Micropor Mesopor Mat*, 2003, **64**, 33-39.
96. K. Barbera, F. Bonino, S. Bordiga, T. V. W. Janssens and P. Beato, *J Catal*, 2011, **280**, 196-205.
97. P. Ratnasamy, G. P. Babu, A. J. Chandwadkar and S. B. Kulkarni, *Zeolites*, 1986, **6**, 98-100.
98. S. K. Sahoo, N. Viswanadham, N. Ray, J. K. Gupta and I. D. Singh, *Appl Catal a-Gen*, 2001, **205**, 1-10.
99. K. S. W. Sing, D. H. Everett, R. A. W. Haul, L. Moscou, R. A. Pierotti, J. Rouquerol and T. Siemieniewska, *Pure Appl. Chem.*, 1985, **57**, 603-619.
100. N. Viswanadham, G. M. Dhar and T. S. R. P. Rao, *J Mol Catal a-Chem*, 1997, **125**, L87-L90.
101. N. Viswanadham, R. Kamble, M. Singh, M. Kumar and G. M. Dhar, *Catal Today*, 2009, **141**, 182-186.
102. Y.-T. Cheng and G. W. Huber, *ACS catalysis*, 2011, **1**, 611-628.
103. J. H. Jae, G. A. Tompsett, Y. C. Lin, T. R. Carlson, J. C. Shen, T. Y. Zhang, B. Yang, C. E. Wyman, W. C. Conner and G. W. Huber, *Energy & Environmental Science*, 2010, **3**, 358-365.
104. D. P. Gamliel, S. Du, G. M. Bollas and J. A. Valla, *Bioresour. Technol.*, 2015, **191**, 187-196.
105. K. D. Hammond and W. C. Conner, in *Advances in Catalysis, Vol 56*, eds. B. C. Gates and F. C. Jentoft, 2013, vol. 56, pp. 1-101.
106. P. S. Rezaei, H. Shafaghat and W. M. A. W. Daud, *Applied Catalysis A: General*, 2014, **469**, 490-511.
107. M. J. Antal and G. Varhegyi, *Ind. Eng. Chem. Res.*, 1995, **34**, 703-717.
108. M. J. Antal, G. Várhegyi and E. Jakab, *Ind. Eng. Chem. Res.*, 1998, **37**, 1267-1275.
109. N. S. Tessarolo, R. C. Silva, G. Vanini, A. Pinho, W. Romão, E. V. R. de Castro and D. A. Azevedo, *Microchemical Journal*, 2014, **117**, 68-76.
110. N. Koike, S. Hosokai, A. Takagaki, S. Nishimura, R. Kikuchi, K. Ebitani, Y. Suzuki and S. T. Oyama, *J. Catal.*, 2016, **333**, 115-126.
111. T. K. Phung and G. Busca, *Chem. Eng. J.*, 2015, **272**, 92-101.
112. D. Varisli, T. Dogu and G. Dogu, *Chem. Eng. Sci.*, 2007, **62**, 5349-5352.
113. H. C. Xin, X. P. Li, Y. Fang, X. F. Yi, W. H. Hu, Y. Y. Chu, F. Zhang, A. M. Zheng, H. P. Zhang and X. B. Li, *J. Catal.*, 2014, **312**, 204-215.